Chapter 6

Prestellar Cores and Deeply Embedded Protostars with Spitzer and Bolocam: Properties of the Youngest Objects in Perseus, Serpens, and Ophiuchus

Abstract

We present an unbiased census of prestellar cores and deeply embedded protostars in Perseus, Serpens, and Ophiuchus, assembled by combining large-scale 1.1 mm surveys and *Spitzer* c2d maps of these clouds. First, we identify protostellar candidates based on *Spitzer* data, and use them to separate starless from protostellar cores in each cloud. A comparison of the properties of the starless and protostellar populations reveals both initial conditions of the starless cores and how formation of a central protostar alters core properties. Starless cores in Perseus have similar masses but larger sizes and lower densities on average than protostellar cores, by factors of 1.5 and 3, respectively, and the sizes suggest density profiles similar to Bonnor-Ebert spheres, or substantially flatter than $\rho \propto r^{-2}$. By contrast, starless cores in Serpens are compact and have lower masses than protostellar cores, while in Ophiuchus there is very little difference between the starless and protostellar populations. The combined

Enoch et al., in preparation; to be submitted to ApJ.

starless core mass distribution includes 108 cores and has a slope of $\alpha = -2.5 \pm 0.2$ for $M > 0.8$ $M_\odot$, consistent with recent measurements of the stellar initial mass function. This result provides support for the idea that stellar masses are directly linked to the core formation process.

We construct well-sampled SEDs for cold protostar candidate using the extensive wavelength coverage ($\lambda = 1.25 - 1100$ μm). Examining different protostellar classification methods, we conclude that bolometric temperature is a better measure of evolutionary state than the spectral index α_{IR} for deeply embedded sources. Source classification yields a total of 43 Class 0 and 94 Class I sources in the three cloud sample. Compared to protostellar evolutionary models using the bolometric temperature-luminosity diagram, we find a population of low luminosity Class I sources that are inconsistent with constant or monotonically decreasing mass accretion rates. This result argues strongly for episodic accretion during the Class I phase, with 25% of sources in a quiescent state. Finally, the relative number of starless, Class 0, and Class I sources are used to estimate lifetimes for the starless and Class 0 phases; we find a Class 0 timescale in Perseus and Serpens of $1 - 2 \times 10^5$ yr. In Ophiuchus, by contrast, we find very few Class 0 sources ($N_{Class0}/N_{ClassI} \sim 0.1$), consistent with previous observations in that cloud. The dense prestellar core phase lasts for approximately as long as the entire embedded protostellar phase, $2-5 \times 10^5$ yr, or only a few free-fall timescales, and is much shorter than the timescale predicted from ambipolar diffusion.

6.1 Introduction

The problem of how low mass stars like the sun form has been studied extensively over the last few decades. Much of this work has naturally focused on isolated objects, where interactions with the local environment or with other objects is limited, and observations are somewhat are easier to interpret. It is well established, however, that most of the star formation in our Galaxy occurs in clusters and groups within large molecular clouds (e.g., Lada & Lada, 2003, and references therein). Molecular clouds

are known to be turbulent, with supersonic linewidths (e.g., McKee & Zweibel, 1992), and to have complex magnetic fields that are likely important to the cloud physics (e.g., Crutcher, 1999). To understand the formation of typical stars we must focus our studies on this complicated environment.

As discussed in chapter 1, a number of open questions remain regarding the formation of stars in molecular clouds, including: (1) What are the physical processes controlling core formation, support, and collapse? (2) What are the initial conditions of star formation, as traced by prestellar cores? (3) How do protostars evolve through the earliest phases, from protostellar formation through Class I? Compared to more evolved protostars and pre-main sequence objects, the earliest stages of the star formation process, from the formation of dense cores through the main mass accretion phase, are relatively poorly understood. This lack of information is due in large part to the difficulty of observing young, deeply embedded sources, which are shrouded within dense protostellar envelopes and only observable via reprocessed emission at mid-infrared to millimeter wavelengths. Large surveys at these wavelengths are essential for addressing the above questions, as is a complete sample of young objects. Large samples are also important for characterizing variations in the star formation process with environment, and to account for biases of such differences in the interpretation of results.

With a few notable, recent exceptions (Jørgensen et al., 2007; Hatchell et al., 2007), previous samples of very young sources have typically been compiled from many different surveys, and suffered from systematics, unquantified environmental effects, and small number uncertainties. The Bolocam surveys of Perseus, Serpens, and Ophiuchus described in chapters 2–4 complement large *Spitzer* Space Telescope IRAC and MIPS maps of the same clouds from the "From Molecular Cores to Planet-forming Disks" *Spitzer* Legacy program ("Cores to Disks" or c2d; Evans et al. 2003). Combining these data sets enables us to assemble a mass limited, unbiased census of the youngest star-forming objects, including prestellar cores, Class 0, and Class I protostars, in three different environments.

The 1.1 mm surveys of Perseus, Serpens, and Ophiuchus were completed with

Bolocam at the Caltech Submillimeter Observatory (CSO). We mapped 7.5 deg^2 (140 pc^2 at our adopted cloud distance of $d = 250$ pc) in Perseus, 1.5 deg^2 (30 pc^2 at $d = 260$ pc) in Serpens, and 10.8 deg^2 (50 pc^2 at $d = 125$ pc) in Ophiuchus (Enoch et al., 2006; Young et al., 2006; Enoch et al., 2007), with a resolution of 31″. Both Bolocam and *Spitzer* maps were designed to cover down to a visual extinction of $A_V \gtrsim 2$ mag in Perseus, $A_V \gtrsim 3$ mag in Ophiuchus, and $A_V \gtrsim 6$ mag in Serpens (Evans et al., 2003). Millimeter emission traces the properties of starless cores and protostellar envelopes, including sizes, masses, and spatial distribution. The *Spitzer* data are complementary in that they provide information about the properties of young protostars embedded within dense cores. The *Spitzer* c2d IRAC and MIPS surveys of each cloud are described in detail in Jørgensen et al. (2006); Harvey et al. (2006); Rebull et al. (2007); Harvey et al. (2007b). The young stellar object (YSO) population in Serpens is discussed in detail by Harvey et al. (2007a). The c2d *Spitzer* surveys are complete at the 50% level to young objects with luminosities as low as $0.01 L_\odot$ (based on the Serpens survey; Harvey et al. 2007a).

In chapter 5, we looked at how the global cloud environment influences the properties of star-forming cores, by comparing the 1.1 mm core populations in Perseus, Serpens, and Ophiuchus. In this chapter we use the combination of the Bolocam 1.1 mm surveys with *Spitzer* c2d MIPS and IRAC maps to study initial conditions and early protostellar evolution. We separate starless cores from protostellar cores in each cloud to probe the initial conditions of star formation on large scales as traced by the starless core samples. Given that we are sensitive to both starless cores and the envelopes around protostars of variable evolutionary state, we can also infer how the formation of a protostar alters the core properties. Extensive wavelength coverage from $\lambda = 1.25 - 1100$ μm allows us to construct well-sampled spectral energy distributions (SEDs) for protostellar sources in their main mass accretion phase, in order to trace their evolution.

We follow Di Francesco et al. (2007) in defining starless cores as low mass dense cores without a compact internal luminosity source, and prestellar cores, at least conceptually, as starless cores that are gravitationally bound. A practical method

of distinguishing prestellar cores is required as well; our operational definition of a prestellar core is a starless core that is detected at submillimeter or millimeter wavelengths. Such sources have mean densities $\gtrsim 2 - 3 \times 10^4$ cm^{-3} (see Ward-Thompson et al. 1994 and §5.3), and are more likely to show evidence for infall motions than lower density starless cores (Gregersen & Evans, 2000). For millimeter cores containing a compact luminous internal source (i.e., an embedded protostar) we follow Di Francesco et al. (2007) in terming these "protostellar cores", regardless of whether the final object will be stellar or sub-stellar in nature. Unlike protostellar cores, which are internally heated by the embedded source, starless cores are externally heated by the interstellar radiation field, with decreasing temperatures toward the core center. In general, we will use the terms Class 0 and Class I to refer to an evolutionary sequence of embedded protostars with $M_* < M_{env}$ and $M_* > M_{env}$, respectively, following André (1994), although the validity of these physical associations is not firmly established (see chapter 1). Our observational definition of Class 0 and Class I, and classification of sources will be discussed in §6.7.

The organization of this chapter is as follows: In §6.2 we describe the combination of the 1.1 mm and *Spitzer* infrared (IR) data. Cold protostar candidates are identified based on their mid- and far-infrared properties in §6.3. Criteria for source selection are discussed, as well as basis on which we determine association with a 1.1 mm core, and the method for distinguishing starless from protostellar cores. The resulting starless and protostellar 1.1 mm core populations for each cloud are compared in §6.4, including core sizes and shapes (§6.4.1), peak and mean particle densities (§6.4.2), distribution in mass versus size (§6.4.3), differential mass distributions (§6.4.4), relationship to cloud column density (§6.4.5), and spatial clustering(§6.4.6). We combine the starless core populations to produce the prestellar core mass distribution (CMD), which is discussed in relation to the stellar initial mass function and combined protostellar CMD in §6.5.

In the second half of this chapter we use our extensive wavelength coverage to study the properties of the embedded protostar populations in each cloud (§6.6), beginning with the calculation of bolometric luminosities and temperatures in §6.6.1

and a discussion of selected individual sources in §6.6.4. We compare protostellar classification methods in §6.7, and discuss alternative classification schemes made possible by our large, unbiased sample in §6.7.1. Sources are placed on a bolometric temperature-luminosity diagram (§6.8) in order to compare to protostellar evolutionary models. Finally, in §6.9 we calculate timescales for the Class 0 and prestellar evolutionary phases.

6.2 Combining Bolocam and Spitzer c2d Data

Our Bolocam 1.1 mm maps of Perseus, Serpens, and Ophiuchus cover nearly the same area as *Spitzer* c2d maps of the sample clouds. The actual overlap in area between Bolocam and IRAC maps is shown in figure 2.1 of chapter 2 for Perseus, figure 3.1 of chapter 3 for Ophiuchus, and figure 4.1 of chapter 4 for Serpens. Catalogs listing c2d measured *Spitzer* fluxes of all sources in each of the three clouds, as well as near-infrared fluxes for sources in the 2MASS catalogs, are available through the *Spitzer* database (Evans et al., 2007). Thus, we have wavelength coverage from $\lambda = 1.25$ to 1100 μm, using 2MASS (1.25,1.65,2.17 μm), IRAC (3.6,4.5,5.8,8.0 μm), MIPS (24,70,160 μm), and Bolocam (1.1 mm) data. Note that 160 μm flux measurements are internal c2d products only, and not included in the public catalogs.

Basic data papers describe the processing and analysis of the *Spitzer* IRAC and MIPS maps of Perseus, Serpens, and Ophiuchus, as well as presenting general properties of the sources in each cloud, such as color-color and color-magnitude diagrams (Jørgensen et al., 2006; Harvey et al., 2006; Rebull et al., 2007; Harvey et al., 2007b). Here we are most interested in cold protostellar sources that are most likely to be embedded in the millimeter cores detected with Bolocam. For the following we will use the term "cold protostar" in general to encompass candidate Class I and younger objects. Although it will become apparent in §6.3 that our criteria also pick up a number of Class II sources, in general we focus on sources with evidence for a protostellar envelope (Class 0 and Class I).

In figures 6.1–6.4 we show the result of combining *Spitzer* and Bolocam data for a

few examples from each cloud. Representative starless cores from Perseus (top row), Serpens (middle row), and Ophiuchus (bottom row) are displayed in figure 6.1 as three-color (8, 24, 160 μm) *Spitzer* images with 1.1 mm Bolocam contours overlaid. Note that the determination of whether or not a core is starless is done in §6.3.1. Symbols ("x") mark the position of all identified 1.1 mm cores, and the Bolocam identification (ID) of the central sources, from table 1 of chapters 2–4, is given at the top of each image. Red 160 μm images are often affected by saturation, pixel artifacts (bright pixels), and incomplete coverage. Saturation by bright sources affects many pixels in a given scan; this and incomplete sampling accounts for the striped appearance of the red images, especially in Ophiuchus. In some cases (e.g., Oph-Bolo 14), large regions are saturated at 160 μm.

Figure 6.1 demonstrates the range of starless cores that we see in each of the clouds. Starless cores may be isolated single sources (Pers-Bolo 62), associated with filaments or groups of other starless cores (Pers-Bolo 73, Oph-Bolo 26), or found near bright protostars (Pers-Bolo 57, Oph-Bolo 14). Although most of the starless cores are extended (e.g., Oph-Bolo 43), some are quite compact (e.g., Pers-Bolo 57), barely resolved by the 31″ Bolocam beam. Some starless cores are distinguished in the Spitzer bands by their bright 160 μm emission. For example, Pers-Bolo 62 is not detectable at 24 or 70 μm, but emerges as a relatively bright, diffuse source at 160 μm, indicating a cold, extended core. The 1.1 mm source is also extended and closely mirrors the 160 μm emission. Other starless cores are less identifiable at 160 μm, but rather stand out as dark "shadows" in the shorter wavelength bands. Serp-Bolo 18 and Oph-Bolo 26 are two examples of such cores; the dark shadows against bright 8 and 24 μm emission are suggestive of dense cores obscuring background nebular emission. These objects generally exhibit 160 μm emission as well, but it is not necessarily well distinguished from local extended 160 μm emission. Again, contours at 1.1 mm closely trace the *Spitzer* short-wavelength shadows.

Figures 6.2–6.4 show examples of embedded protostellar sources in each cloud. Images are now three-color *Spitzer* maps at (8, 24, 70 μm), and do not include 160 μm data. As before, 1.1 mm contours are overlaid. Sources were chosen both to

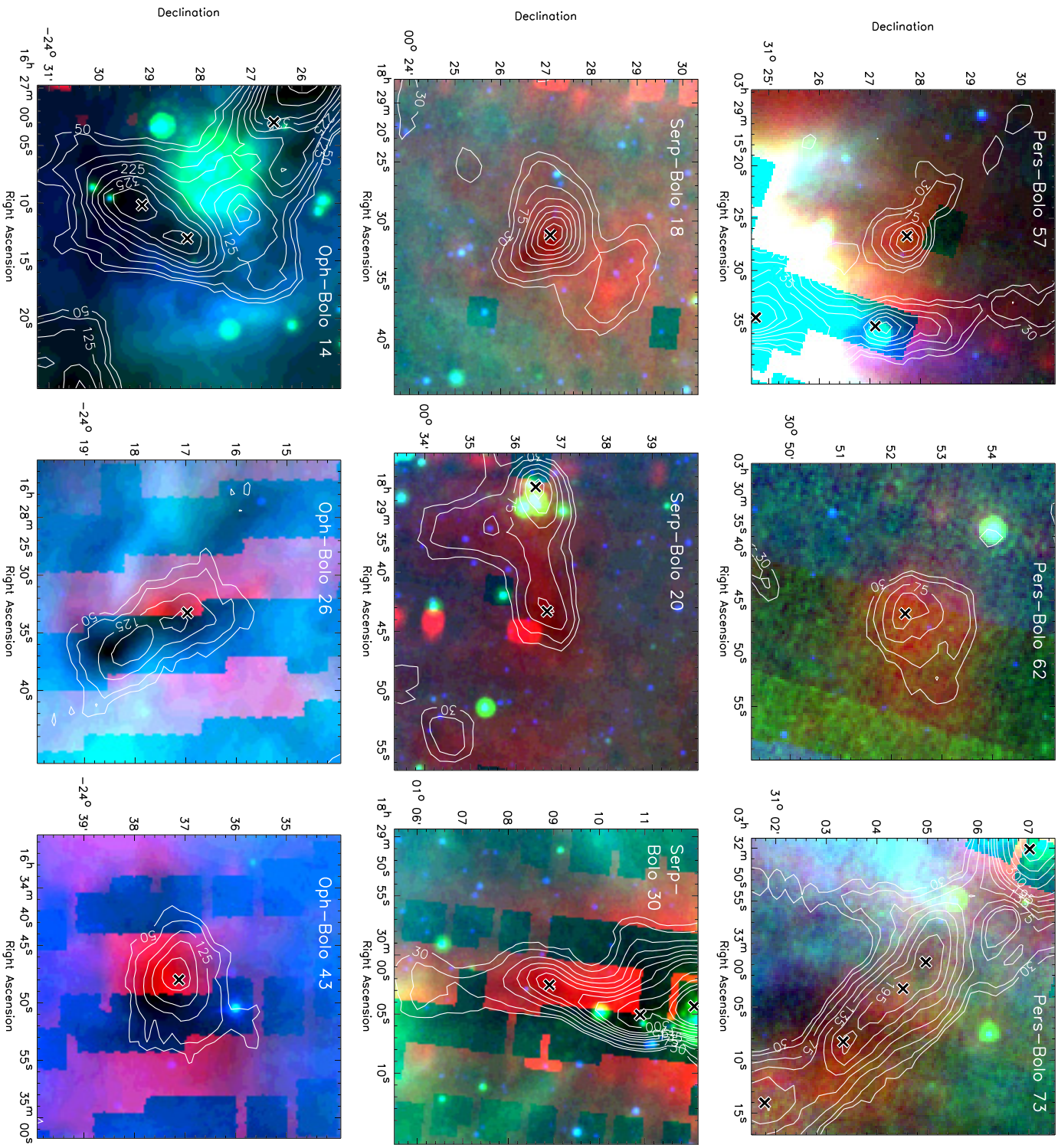

Figure 6.1 Three color Spitzer images (8.0, 24, 160 μm) of selected starless cores in Perseus, Serpens, and Ophiuchus, with 1.1 mm contours. Contour intervals are $2, 3, 5, 7, 9, 11, 13, 15, 20, 25, 30, 35\sigma$, where 1σ is the mean rms noise in each cloud (15 mJy in Perseus, 10 mJy in Serpens, and 25 mJy in Ophiuchus). Positions of identified Bolocam 1.1 mm cores are indicated by an "x", and the Bolocam ID of the centered core is given. Saturation, image artifacts, and incomplete sampling causes the striped appearance of some of the red 160 μm images.

highlight newly identified highly embedded objects, as well as to illustrate the wide variety of sources that we are able to characterize by combining these data. As for figure 6.1, the Bolocam ID of the centered 1.1 mm core is given. We use the 2MASS, IRAC, MIPS, and Bolocam data to construct complete spectral energy distributions (SEDs) from 2 to 1100 μm for each protostellar source associated with the central Bolocam core in figures 6.2–6.4. The SEDs are also shown in these figures in the lower panels, and will be discussed further in §6.6. Additional SHARC II 350 μm fluxes (Wu et al., in preparation) and SCUBA 850 μm fluxes (Kirk et al., 2006, open circles) are included when available.

Protostellar sources in our sample may be isolated (e.g., Pers-Bolo 57) or lie in crowded regions (e.g., Pers-Bolo 49), similar to starless cores. Approximately 5%–20% of the time, depending on cloud, more than one protostellar source lies within a single 1.1 mm core. This is almost certainly due to the fact that the Bolocam beam (31″) is larger than the *Spitzer* beam at 24 μm (7″), and multiple *Spitzer* sources will be blended in the 1.1 mm map. Sometimes the SEDs of such multiple sources look similar to each other (Pers-Cold 19 and 24 in the lower-left panel of figure 6.2), and sometimes quite different (Pers-Cold 50 of the same panel).

Although the coverage of the IRAC, MIPS and Bolocam maps overlaps nearly perfectly for our purposes, there are a few cases in which cold protostar candidates are outside the boundaries of the MIPS 70 μm map (three sources in Serpens) or 1.1 mm map (one source in Perseus). In addition, the 160 μm maps are often saturated near bright sources and in regions of bright extended emission, such as near bright clusters of sources. Reliable 160 μm fluxes are especially difficult to determine in crowded regions, due both to the large beam size (40″) and saturation issues. The lack of 160 μm data is most problematic in Ophiuchus, where the 160 μm maps are saturated in all of the dense source regions. Even for isolated sources, the measured 160 μm flux density, determined from a point spread function (PSF) fit, may be underestimated if the source is extended. The effects of these issues on our analysis are discussed in more detail in the appendix Section 6.11

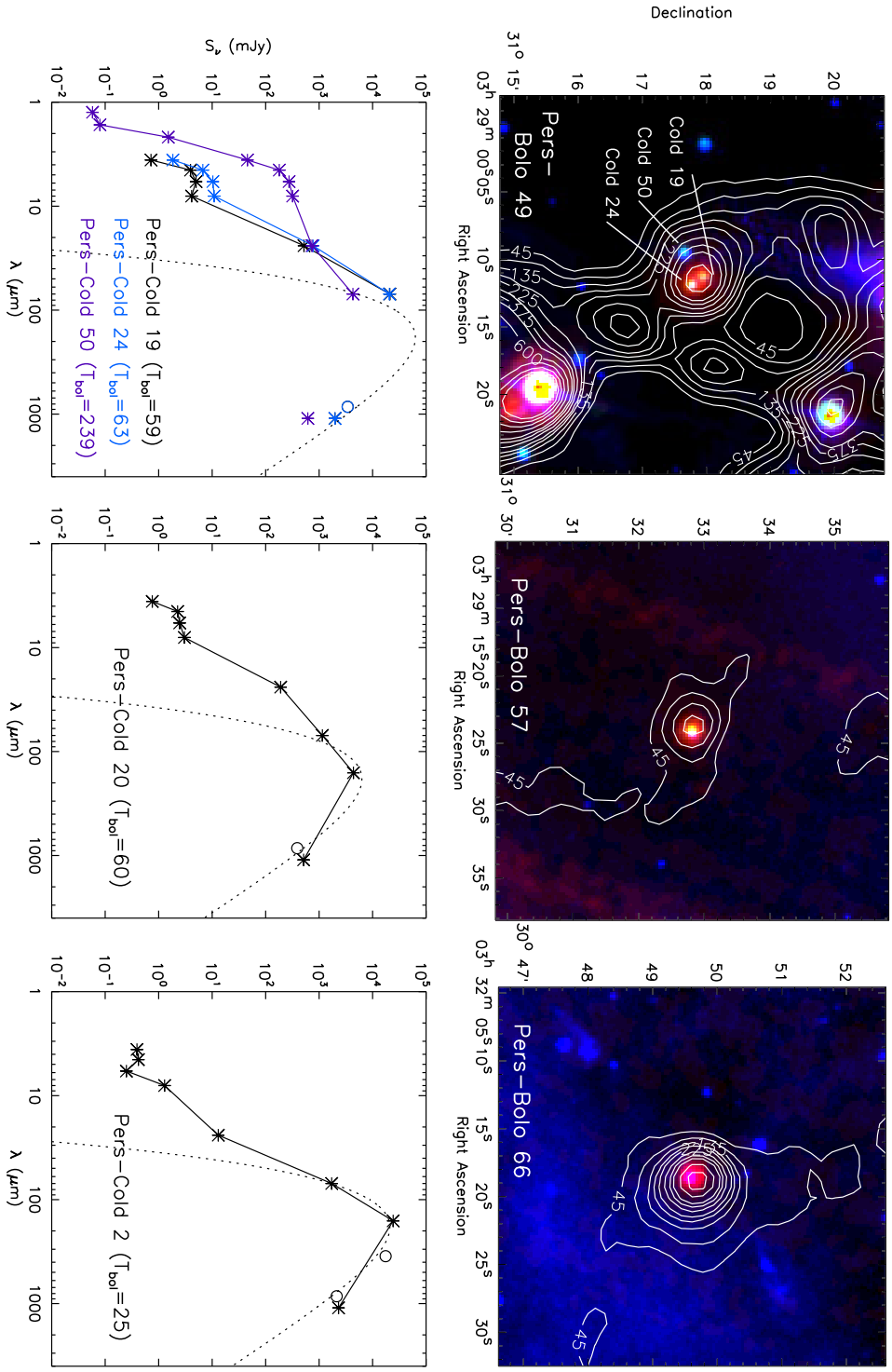

Figure 6.2 three-color Spitzer images (8.0, 24, 70 μm) of selected protostellar cores in Perseus, with 1.1 mm contours. Spectral energy distributions (SEDs) of protostellar sources associated with each core are plotted in the lower panels. SEDs include 2MASS, IRAC, and MIPS photometry from the c2d database and 1.1 mm fluxes (asterisks), as well as published 350 μm and 850 μm points if available (open circles). The Bolocam ID of the centered core is also given. Contour intervals for the 1.1 mm emission are $3, 6, 9, 12, 15, 20, 25, ..., \sigma$.

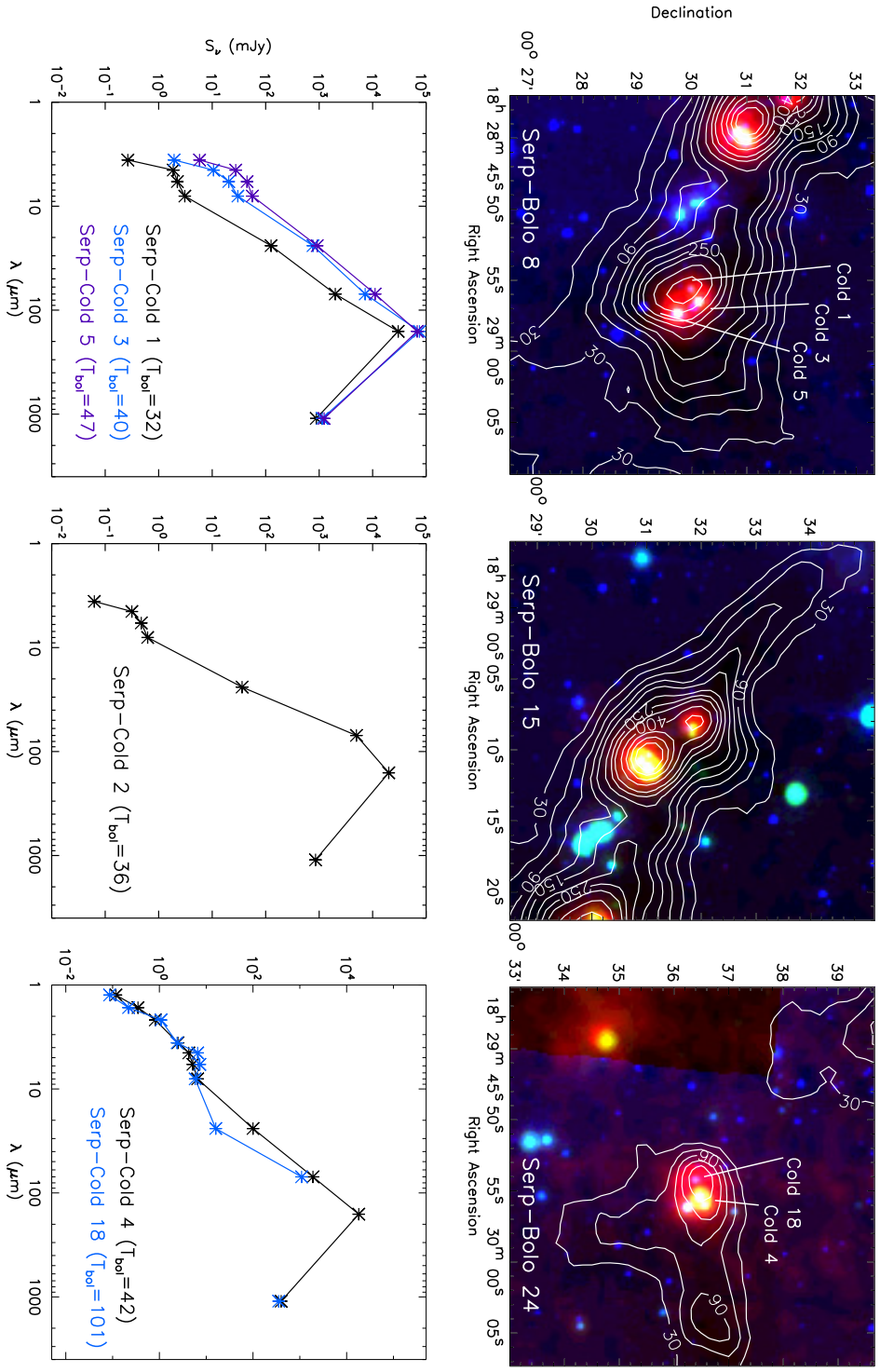

Figure 6.3 three-color Spitzer images (8.0, 24, 70 μm) of selected protostellar cores in Serpens, with 1.1 mm contours. Spectral energy distributions of protostellar sources associated with each core are plotted in the lower panels. Contours, photometry, and identifications are as in figure 6.2.

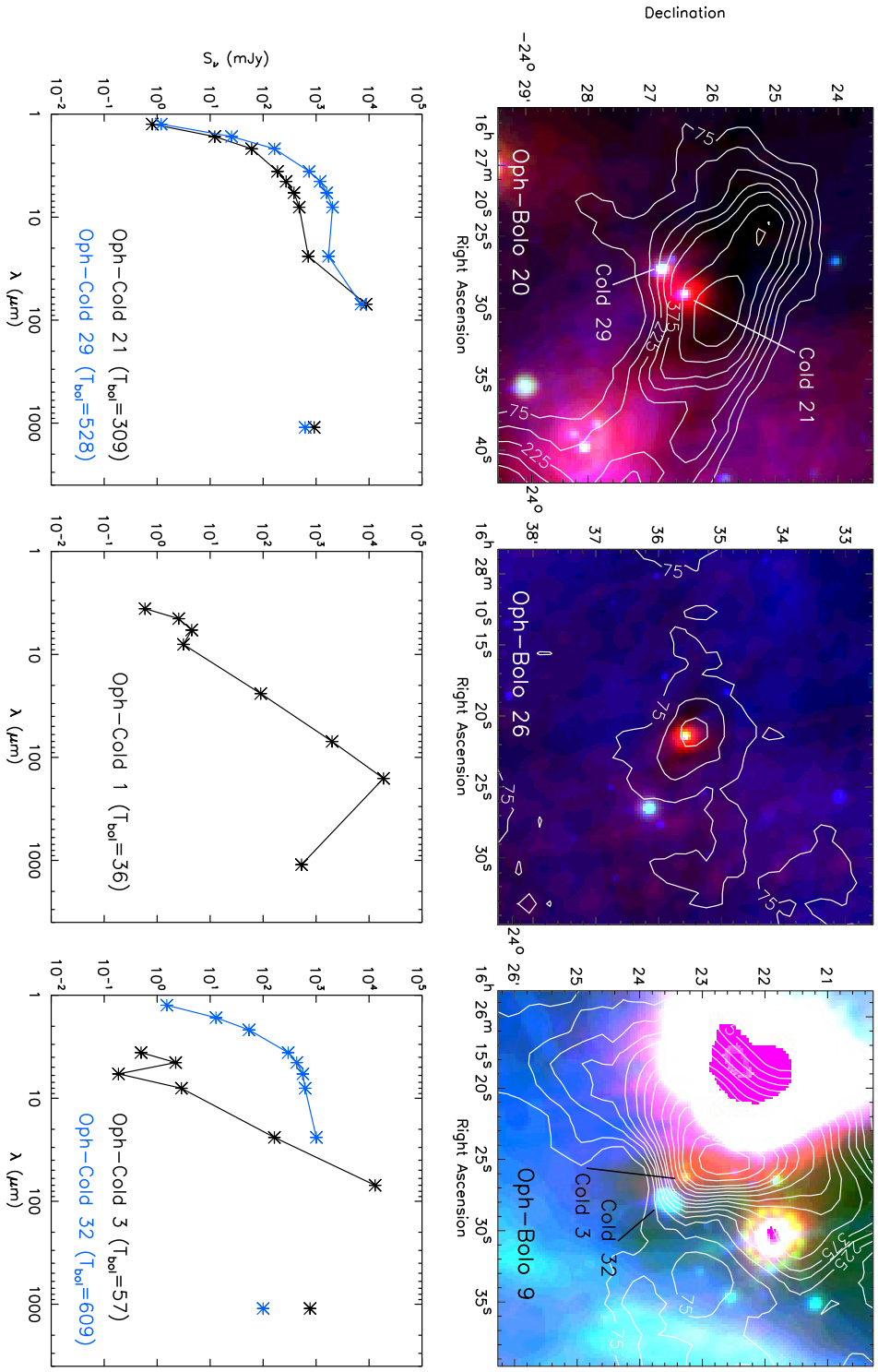

Figure 6.4 three-color Spitzer images (8.0, 24, 70 μm) of selected protostellar cores in Ophiuchus, with 1.1 mm contours. Spectral energy distributions of protostellar sources associated with each core are plotted in the lower panels. Contours, photometry, and identifications are as in figure 6.2.

6.3 Identifying Cold Protostars

We form a sample of candidate cold protostars from the c2d catalogs; the first cut is based on the source "class." All sources in the c2d catalogs are assigned a class parameter based on colors, magnitudes, and stellar SED fits, as discussed in the c2d Delivery Document (Evans et al., 2007) and Harvey et al. (2007a). Class parameters include "star", "star+disk", "YSOc" (young stellar object candidate), "red", "rising", "Galc" (galaxy candidate), etc. Serpens is used as an example and to test our method, because the list of YSO candidates in Serpens, which includes embedded protostars as well as more evolved star-plus-disk sources, has also been carefully checked by Harvey et al. (2007a). Cold protostars will generally be a subset of YSOc sources, but some of the most embedded may also be assigned to the "red" class if they are not detected in all four IRAC bands. Thus, we begin by selecting all sources from the c2d database that are classified as "YSOc" or "red." From this list, we keep only sources that meet *all* of the following criteria:

(a) flux density at 24 μm ($S_{24\mu\mathrm{m}}$) $\geq$ 3 mJy

(b) $S_{24\mu\mathrm{m}} \geq 5\alpha_{IR} + 8$ mJy, where α_{IR} is the near- to mid-infrared spectral index, determined by a least-squares fit to all fluxes shortward of 24 μm.

(c) $S_{24\mu\mathrm{m}}$ and $S_{8\mu\mathrm{m}}$ must be of high quality, i.e., both measured flux densities have signal to noise (S/N) higher than 7.

(d) if $S_{24\mu\mathrm{m}} < 50$ mJy, then it is not a "band-filled" flux. For sources not originally detected in all *Spitzer* bands, a flux or upper limit is measured at the source position (band-filling, Harvey et al. 2007a). Because the resolution is lower at 24 μm than at the shorter wavelengths, some IRAC-only sources have unreliable band-filled fluxes at 24 μm (e.g., sources are confused with the PSF wings of a nearby source).

In addition, we include in our sample any 70 μm point sources that are not classified as galaxy candidates ("Galc"). In each cloud, a few deeply embedded sources that have strong 70 μm emission but very weak 24 μm emission (e.g., HH211 in Perseus) are recovered by this last criteria, as are a few very bright sources that are saturated at 8 μm or 24 μm (these are often classified as "rising").

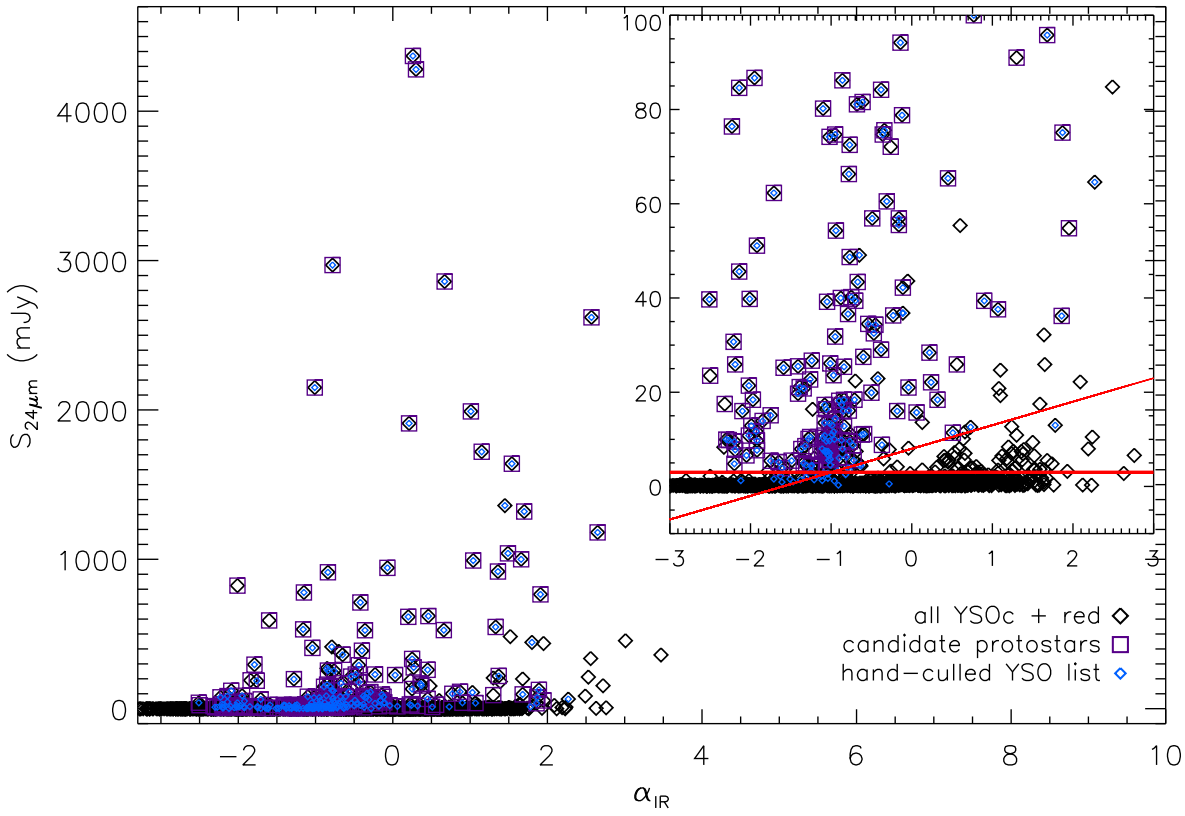

Figure 6.5 Plot of $S_{24\mu\mathrm{m}}$ versus spectral index α_{IR} for sources in Serpens, to demonstrate selection criteria for the cold protostar samples. Black diamonds represent all catalog sources labeled as "YSOc" or "red." Smaller blue diamonds show the carefully vetted YSO sample from Harvey et al. (2006). Red lines (inset) show 24 μm flux cuts imposed by criteria (a) and (b), which remove most sources not in the hand-culled sample. Boxes indicate the final cold protostar sample, after applying criteria (a)-(d). The hand-culled and final candidate protostar samples match well, with the exception of a few sources that require examination by eye (see text).

The sample formed using the above criteria (a–d) is quite similar to the carefully vetted list of YSO candidates from Harvey et al. (2007a), as shown in figure 6.5. In this figure, which plots $S_{24\mu\mathrm{m}}$ versus α_{IR}, black diamonds are the original "YSOc"+"red" sample for Perseus, blue diamonds are the "hand-culled" YSOs from Harvey et al. (2007a), and our cold protostar candidates after applying criteria (a)-(d) are indicated by purple boxes. The majority of the black-only points, which were rejected as true YSOs by Harvey et al. (2007a), are removed by criteria (a) and (b) (shown as red lines). The 14 sources in the hand-culled list but not in our sample (blue diamonds,

no box) are classified as "star+dust" and were examined by hand and found to have Class II-like SEDs, with no nearby 1.1 mm emission. There are also a few sources in our sample that are not in the hand-culled sample (black diamond plus box). Most of these were fairly easily identified as non-protostellar when examining by eye. We do identify three additional cold protostar candidates based on their 70 μm fluxes, which are not in the hand-culled sample but seem to be associated with 1.1 mm emission (see §6.3.1): one "red", one "rising", and one "cup-up."

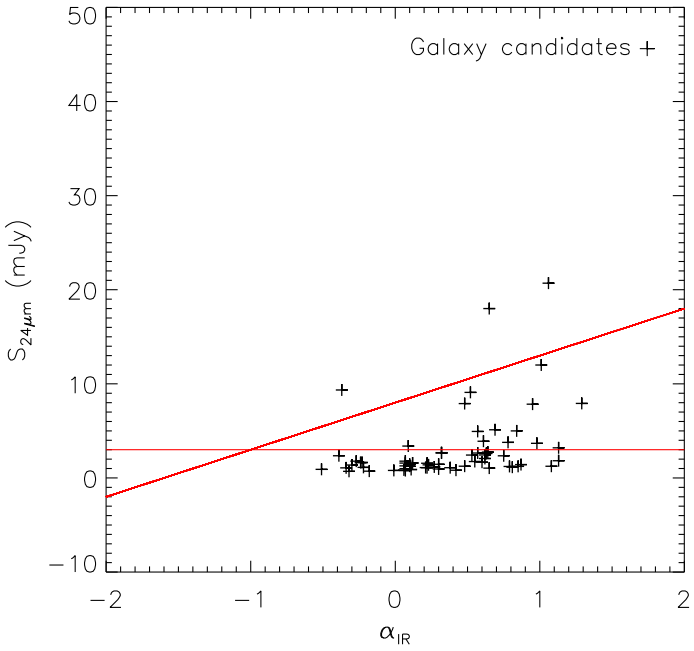

Figure 6.6 Plot of $S_{24\mu\mathrm{m}}$ versus spectral index α_{IR} for galaxy candidates ("Galc") in Serpens. Selection criteria (a) and (b) are plotted, as in figure 6.5. The selection criteria eliminate most of the parameter space inhabited by extragalactic sources.

In addition to weeding out false "YSOc" sources, our cold protostar criteria are efficient at removing objects with the properties of extragalactic sources, as shown in figure 6.6. In this figure, $S_{24\mu\mathrm{m}}$ is plotted versus α_{IR} for all "Galc" galaxy candidates in Serpens. As in figure 6.5, red lines show criteria (a) and (b), which effectively eliminate most galaxy candidates. Therefore, if any extragalactic sources are mistakenly classified as "YSOc", the majority would be removed from our sample by these criteria. After having checked our criteria using the Serpens sample, we apply them to the other clouds to produce candidate cold protostar samples for Perseus

and Ophiuchus. Finally, the images and SEDs of each source are examined by eye to remove any galaxies that are extended in the near-infrared, and other obviously non-embedded sources.

In some cases, there is no available point-source flux at 70 or 160 μm even if there is emission at the position of the source, generally because the source is extended at these wavelengths. In these cases a flux density is measured by hand, if possible, using aperture photometry. A few bright sources were saturated at 8 or 24 μm; the flux for these was estimated using aperture photometry and interpolating over bad pixels. Large uncertainties for these saturated or band-filled flux measurements (50% or more) are reflected in the errors on these flux points.

6.3.1 Association with a 1.1 mm Core

Once we have a sample of candidate cold protostars, we next determine which of these objects are associated with 1.1 mm emission. Rather than use a single distance criteria, we examine the distance from the protostar to the nearest 1.1 mm peak, and assign a protostellar source to a given millimeter core if it is within $1.0 \times \theta_{1mm}$ of the 1.1 mm core centroid position, where θ_{1mm} is the angular full-width at half-maximum (FWHM) size of the core. To justify this choice, we plot in figure 6.7 (left) the distribution of cold protostar candidates in Perseus, including all "YSOc", "red" and 70 μm sources, around each core position. This is inspired by a similar analysis done by Jørgensen et al. (2007) (their figure 2). The distance from each protostar candidate to the nearest 1.1 mm core is shown in units of the core FWHM size; large circles enclose sources within $0.5 \times \theta_{1mm}$ and $1.0 \times \theta_{1mm}$ of a core position. Sources with $T_{bol} < 70$ K and $70 < T_{bol} < 650$ K (as determined in Section 6.7) are color coded red and blue, respectively. In general we find that the coldest protostars are all within $1.0 \times \theta_{1mm}$ of a millimeter core position, as expected if they are deeply embedded.

Figure 6.7 (right) is similar, but for a spatially random distribution of *Spitzer* sources over the Bolocam map area. This is equivalent to taking the candidate pro-

tostars that appear in the left panel and spreading them randomly across the cloud. There are approximately the same number of sources in the random distribution as in the candidate protostar sample, but only a small number of the randomly distributed sources fall within a few core FWHM of a 1.1 mm core position. There are two sources from the random distribution within $1.0 \times \theta_{1mm}$ of a core position; thus we can expect up to two false associations with 1.1 mm cores in each cloud using this criteria. Using $0.5 \times \theta_{1mm}$ would be a more restrictive choice, but might miss some cold protostars or mis-identify protostellar cores as starless.

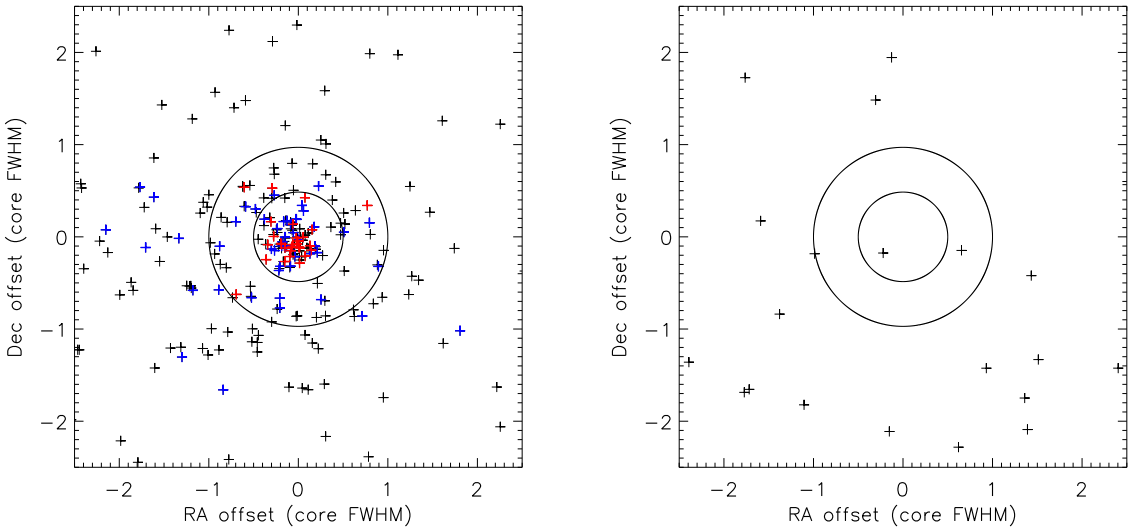

Figure 6.7 *Left:* Distribution of the distance from cold protostar candidates in Perseus to the nearest core position, including all "YSOc", "red" and 70 μm sources. Distances are in units of the core FWHM size θ_{1mm}. Sources with $T_{bol} < 70$ K and $70 < T_{bol} < 650$ K are color coded red and blue, respectively. *Right:* Similar, but for a spatially random distribution of *Spitzer* sources over the Bolocam map area. There are approximately the same number of *Spitzer* sources in the random distribution as in the candidate protostar sample at left, but only a small number fall within a few FWHM of a 1.1 mm core position. Circles enclose sources within 0.5 and 1.0 θ_{1mm} of a core position. Our definition that candidate protostars within 1.0 θ_{1mm} are associated with a given core may result in approximately two false identifications in each cloud.

If a cold protostar candidate is found to be associated with a millimeter core by the above criteria, the 1.1 mm flux is included in the protostellar SED, and is used to calculate an envelope mass (M_{env}) for that protostellar source (see §6.6.2). If a given

cold protostar candidate is not within $1.0 \times \theta_{1mm}$ of a millimeter core, we calculate an upper limit from the original 1.1 mm map. In a number of cases (12 in Perseus, 4 in Serpens, and 15 in Ophiuchus) there is clearly 1.1 mm flux at the protostar position, that was not identified as a core in the original 1.1 mm source extraction because it is below 5σ or is in a confused region of the map. If this emission exceeds a threshold of approximately 3 times the local rms noise, we measure a 1.1 mm flux using a small aperture (30″–40″). In regions of blended 1.1 mm emission, we also re-compute the 1.1 mm flux density in small apertures, rather than simply adopting the total core flux. When more than one protostar candidate is associated with a single compact millimeter core, we divide the 1.1 mm flux equally between the protostellar sources.

Approximately 20% of the cold protostar candidates in each cloud (40% in Oph) are lacking 1.1 mm emission, even after re-examining the 1.1 mm maps at each source position. Most of these sources appear to be late Class I or early Class II sources, with little or no remaining envelope. Any 1.1 mm emission from these objects, therefore, is likely below our detection limit of $\sim 0.1 M_{\odot}$. A few of these may actually be low luminosity sources that are truly embedded in a low mass envelope below our detection limit. For this reason, we only claim completeness to protostars with $M_{env} > 0.1$ $M_{\odot}$, as discussed further in §6.9.

6.3.2 Separating Starless and Protostellar Cores

To study the initial conditions of star formation, as traced by prestellar cores, as well as how the formation of a central protostar alters core properties, we first must differentiate cores with internal luminosity sources (protostellar cores) from those without an embedded self-luminous source (starless cores). Protostellar cores will have lost some mass due to accretion onto the embedded protostar, and may be otherwise altered so that they are no longer representative of core initial conditions. Any core that has a cold protostar candidate within $1.0 \times \theta_{1mm}$ of the core center is considered protostellar, based on the discussion in §6.3.1. In addition, we examine the remaining 1.1 mm cores, searching for any "YSOc" source that has $S_{24\mu m} > 3$ mJy

and is within $1.0 \times \theta_{1mm}$ of the core center, even those that do not meet the criteria of §6.3.1. A flux limit at $S_{24\mu\mathrm{m}}$ of 3 mJy is chosen because that is the flux of the most embedded known protostar at 24 μm (HH211), and it is high enough to eliminate sources with SEDs that are clearly inconsistent with an embedded nature (e.g., sources with $S_{24\mu\mathrm{m}} < S_{8\mu\mathrm{m}}$).

An additional 2 cores in Perseus, 2 in Serpens, and 5 in Ophiuchus are determined to be protostellar cores by this latter method. Note, however, that the "YSOc" sources assumed to be associated with these cores are not added to the cold protostar sample; in general they do not meet our criteria because they are very faint at 24 μm and are not detected at 70 μm. It is not at all clear that these YSOc sources are truly associated with the 1.1 mm cores with which they are spatially coincident, especially as the 1.1 mm core flux density is generally much higher than what would be expected from the *Spitzer* 24 μm flux, and none are detected at 70 or 160 μm. In fact, some associations are probably just an effect of projection on the sky. Figure 6.7 demonstrates that at least a few non-embedded sources will be projected within $1.0 \times \theta_{1mm}$ of a core position. As we do not want to mistakenly contaminate our starless core sample with more evolved sources, however, we adopt this very conservative criteria for starless cores. Therefore the number of starless cores in each cloud is likely a lower limit to the true value.

Table 6.1 gives the number of starless (N_{SL}) and protostellar (N_{PS}) cores in each cloud, as well as the ratio N_{SL}/N_{PS}. Note that the number of starless and protostellar cores are approximately equal in each cloud ($N_{SL}/N_{PS} = 1.2$ in Perseus, 0.8 in Serpens, and 1.4 in Ophiuchus), a fact that will be important for our discussion of the starless core lifetime in §6.9. Differences between the clouds are not significant, as the mis-identification of only a few starless cores as protostellar in Serpens would make the ratio closer to 1.1, similar to the other clouds. The number of cold protostar candidates from §6.3.1 that are associated with 1.1 mm emission is given in column six of table 6.1. Notice that this number is larger than the number of protostellar cores in each cloud. Part of the difference is explained by sources that have been "band-filled" at 1.1 mm, while the remaining excess is accounted for by individual

Table 6.1. Statistics of 1.1 mm cores in the three clouds

Cloud	N_{total}[1]	N_{SL}[2]	N_{PS}[3]	N_{SL}/N_{PS}	N_{Cold}[4](w/1mm)	N_{PS} (mult)[5]
Perseus	122	67	55	1.2	68	13
Serpens	35	15	20	0.8	37	11
Ophiuchus	44	26	18	1.4	32	3

[1]Total number of identified 1.1 mm cores.

[2]Number of starless 1.1 mm cores, i.e., cores that do not have a YSO candidate (with $S_{24\mu m} > 3$ mJy) within $1.0 \times \theta_{1mm}$ of the core center.

[3]Number of protostellar cores.

[4]Number of cold protostar candidates that are associated with 1.1 mm emission, as determined in §6.3.1.

[5]Number of protostellar cores that are associated with more than one candidate cold protostar (within $1.0 \times \theta_{1mm}$ of the core center).

cores that are associated with more than one cold protostar candidate. There are 13 such multiple protostellar sources in Perseus (24% of the protostellar core sample), 11 in Serpens (55%), and 3 in Ophiuchus (17%), as noted in the last column of table 6.1.

6.4 Comparing the Starless and Protostellar 1.1 mm Core Populations

Having separated the starless and protostellar core populations in each cloud, we now compare their physical properties, with two primary goals. First, isolating a starless core sample allows us to probe the initial conditions of star formation in each cloud, as reflected in the properties of the starless cores. Second, differences between the starless and protostellar core samples are indicative of how the formation of a central protostar alters core properties. In the next several sections we follow the methodology of chapter 5, examining the sizes and shapes of cores, their peak and mean densities, the distribution of core mass versus size, their spatial clustering properties, and their relationship to the surrounding cloud column density.

6.4.1 Sizes and Shapes

Figure 6.8 shows the distribution of the angular deconvolved sizes of protostellar and starless cores in Perseus, Serpens, and Ophiuchus. The angular deconvolved size is calculated as $\theta_{dec} = \sqrt{\theta^2_{meas} - \theta^2_{mb}}$, where θ_{meas} is the geometric mean of the measured minor and major axis FWHM sizes and θ_{mb} is the beam FWHM ($31''$). Recall from chapter 5 that the measured size does not necessarily represent a physical boundary, but rather is a characteristic scale that depends on the linear resolution and intrinsic source density profile. Starless cores are larger on average in Perseus than protostellar cores (figure 6.8, left panel), with average θ_{dec} values of $67'' \pm 23''$ and $50'' \pm 17''$, respectively. Note that the standard deviation quoted here and in the rest of §6.4 is the dispersion in the sample, *not* the error in the mean.

As discussed in chapter 5, for sources with power law density profiles, which do not have a well defined size, θ_{dec}/θ_{mb} is independent of distance and simply related to the index of the power law (Young et al., 2003). According to the correlation between θ_{dec}/θ_{mb} and density power law exponent p found by Young et al. (2003), a mean θ_{dec}/θ_{mb} value of ($50''/31'' = 1.6$) for protostellar cores in Perseus implies an average power law index of $p \sim 1.4$ to 1.5. Many well-known protostellar sources have been found to have envelopes consistent with power law density profiles, as determined by high-resolution imaging combined with radiative transfer modeling. Our inferred average index for Perseus protostellar cores ($p = 1.4 - 1.5$) is consistent with, but slightly smaller than, the mean $p \sim 1.6$ from radiative transfer modeling of Class 0 and Class I envelopes (Shirley et al., 2002; Young et al., 2003). For reference, a singular isothermal sphere has $p = 2$, and the profile expected for a free-falling envelope is $p = 1.5$ (Shu, 1977).

In contrast, the distribution of θ_{dec} for starless cores in Perseus is relatively flat, with a few barely resolved cores, and several larger than 3 θ_{mb}. It is difficult to reconcile such large values of θ_{dec} with power law density profiles. The mean θ_{dec}/θ_{mb} value of 2.2 for starless cores in Perseus would imply an extremely shallow mean power law index of $p \sim 1.1$, and the maximum value ($\theta_{dec}/\theta_{mb} \sim 3.5$) would correspond to

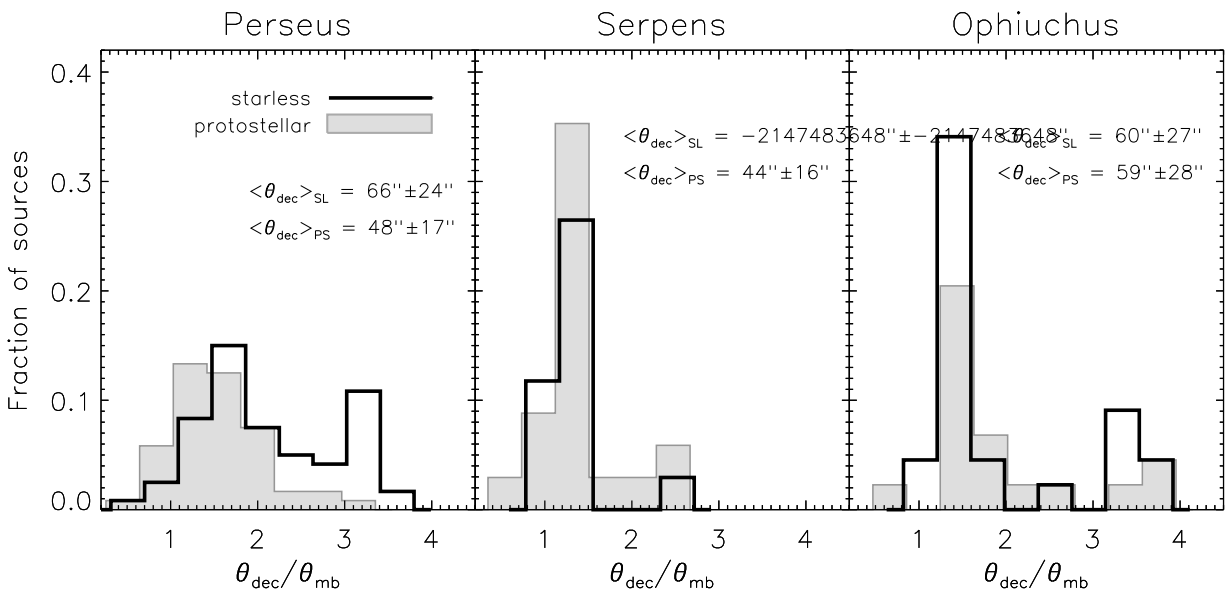

Figure 6.8 Distributions of the angular deconvolved sizes of starless and protostellar cores in the three clouds. The size is given in units of the beam FWHM (θ_{mb}), and the mean of each distribution $\pm$ the dispersion in the sample is listed. Starless cores are larger on average than protostellar cores in Perseus, with a flattened distribution out to 3.5 θ_{mb}. In Serpens and Ophiuchus, however, there is very little difference between the starless and protostellar distributions, with a few very large cores.

$p < 0.8$. On the other hand, a Bonnor-Ebert sphere (Ebert, 1955; Bonnor, 1956) with a central density of 10^5 cm^{-3} and an outer radius of 6×10^4 AU would correspond to $\theta_{dec}/\theta_{mb} = 2.0$ at the distance of Perseus. Thus, very large starless cores are more consistent with BE spheres or other flattened profiles than with a power law density profile. Although the classical pre-collapse singular isothermal sphere (SIS) follows a power law with $p = 2$, there is significant evidence that many starless cores do indeed look like BE spheres (e.g., Johnstone et al. 2000; Shirley et al. 2000; Alves et al. 2001). Note, however, that a sufficiently centrally condensed BE sphere will be indistinguishable from a power law on the scales to which we are sensitive.

Despite the size difference between starless and protostellar cores in Perseus, there is no difference between the two axis ratio distributions (figure 6.9, left panel). Here the axis ratio is defined at the half-max contour: major axis FWHM/minor axis

FWHM. Both starless and protostellar cores have a mean axis ratio of 1.4, with a dispersion of 0.3. Monte Carlo tests indicate that cores with axis ratios less than 1.2 should be considered round. Thus both starless and protostellar cores are slightly elongated on average in Perseus.

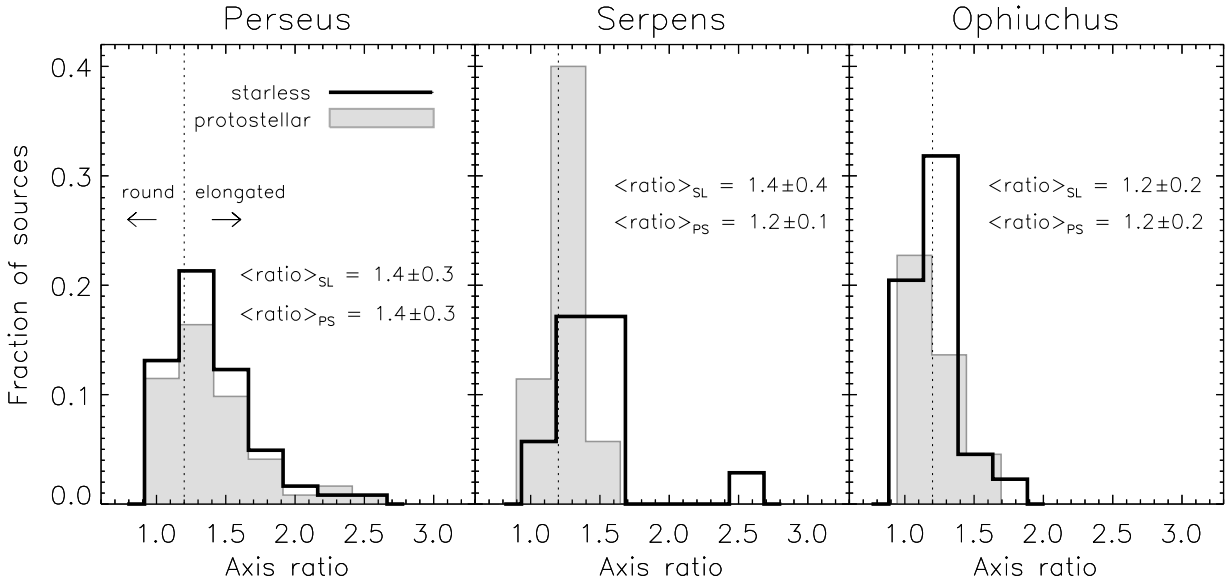

Figure 6.9 Distributions of the axis ratios of starless and protostellar cores in the three clouds. Cores with axis ratios < 1.2 are considered round, and those with axis ratios > 1.2 elongated. Only in Serpens, where starless cores tend to be slightly more elongated (mean axis ratio $= 1.4 \pm 0.4$) than protostellar cores (mean axis ratio $= 1.2 \pm 0.1$), is there a measurable difference between the starless and protostellar populations.

The relative properties of starless and protostellar cores are quite different in Serpens than in Perseus (figures 6.8 and 6.9, middle panels). Starless cores in Serpens have sizes ($\langle\theta_{dec}\rangle = 42'' \pm 12''$) similar to protostellar cores ($\langle\theta_{dec}\rangle = 45'' \pm 15''$). The mean value for protostellar cores ($\theta_{dec}/\theta_{mb} = 1.5$) corresponds to an average power law index of $p = 1.5$, similar to that found for Perseus. In contrast to Perseus, starless cores do not appear to have flatter density profiles than protostellar cores. Starless cores in Serpens do tend to be slightly more elongated (mean axis ratio $= 1.4 \pm 0.4$) than protostellar cores (mean axis ratio $= 1.2 \pm 0.1$).

In Ophiuchus, there is no measurable difference between the starless and protostellar populations (figures 6.8 and 6.9, right panels). The starless and protostellar samples have similar mean sizes ($\langle\theta_{dec}\rangle = 60'' \pm 27''$ and $59'' \pm 28''$, respectively), and both populations display a bimodal behavior. The lower peak is similar to the single peak seen in Serpens at $\theta_{dec} = 1 - 2\ \theta_{mb}$, while the smaller upper peak is at sizes of $\theta_{dec} = 3 - 4\ \theta_{mb}$, comparable to the largest starless cores in Perseus. The mean θ_{dec}/θ_{mb} for protostellar cores in Ophiuchus (1.9) corresponds to an average power law index of $p = 1.3$, and the median value (1.6) to $p = 1.4$. Both starless and protostellar cores in Ophiuchus appear quite round; the mean axis ratio is 1.2 ± 0.2 for both populations. As discussed in chapter 5, the fact that cores in Ophiuchus are observed to be more round than in the other two clouds is likely a result of the higher linear resolution in that cloud, rather than a physical distinction.

To summarize, starless cores are larger on average than protostellar cores in Perseus. The protostellar distribution in Perseus is consistent with power law density sources with an average index $p = 1.4 - 1.5$, while the starless distribution is suggestive of Bonnor-Ebert spheres or very flattened profiles. Both starless and protostellar cores are compact in Serpens, with starless cores being somewhat more elongated on average. There is no difference in the sizes or axis ratio distributions of starless and protostellar cores in Ophiuchus; both populations have a bimodal distribution of sizes, with a few cores at very large sizes. The smaller sizes of both starless and protostellar cores in Serpens and Ophiuchus compared to Perseus may be related to the general lack of isolated sources in those clouds. The measured size of a core is limited by the distance to the nearest neighboring source, meaning that in crowded regions the measured size will tend to be smaller than for isolated sources.

6.4.2 Core Densities

Figures 6.10 and 6.11 compare the peak and mean densities of starless and protostellar cores in each cloud. We use the peak column density N_{H_2}, calculated from the peak 1.1 mm flux density (§2.4.2 and equation (2.2)), as a measure of the peak density.

Note that the peak density is an average over the 31″ beam. As discussed in §5.3, the 1.1 mm emission traces significantly higher column densities than other tracers such as the reddening of background stars. Mean particle densities are calculated at the half-max contour: $\langle n \rangle = 3M/(4\pi R^3 \mu m_H)$, where M is the core total mass, R is the linear deconvolved half-width at half-max size, and $\mu = 2.33$ is the mean molecular weight per particle.

Core masses are calculated from the total 1.1 mm flux assuming the dust emission at $\lambda = 1.1$ mm is optically thin, and that both the dust temperature and opacity are independent of position within a core:

$$M = \frac{d^2 S_\nu}{B_\nu(T_D)\kappa_\nu}, \tag{6.1}$$

where κ_ν is the dust opacity, d is the cloud distance, and T_D is the dust temperature. We assume a dust opacity at 1.1 mm of $\kappa_{1.1mm} = 0.0114$ cm^2 g^{-1}, interpolated from table 1 column 5 of Ossenkopf & Henning (1994) for dust grains with thin ice mantles (see chapter 1). A gas to dust mass ratio of 100 is included in $\kappa_{1.1mm}$.

The dust temperature T_D should depend on whether a core is starless or has an internal source of luminosity, and we assume a slightly higher temperature for protostellar cores ($T_D = 15$ K) than for starless cores ($T_D = 10$ K). For dense regions without internal heating, the mean temperature is about 10 K, warmer on the outside and colder on the inside (Evans et al., 2001). Our assumed value of 15 K for protostellar cores is the average isothermal dust temperature found from radiative transfer models of a sample of Class 0 and Class I protostars (Shirley et al., 2002; Young et al., 2003). The isothermal dust temperature is the temperature that, when used in an isothermal mass equation (e.g., equation (6.1), above) yields the same mass as does a detailed model including temperature gradients. The difference in mass between assuming $T_D = 10$ K and 15 K is a factor of 1.9, as can be easily seen from the difference between the starless and protostellar completeness curves in figure 6.12 (§6.4.3).

Both peak N_{H_2} values and mean densities are significantly lower on average for

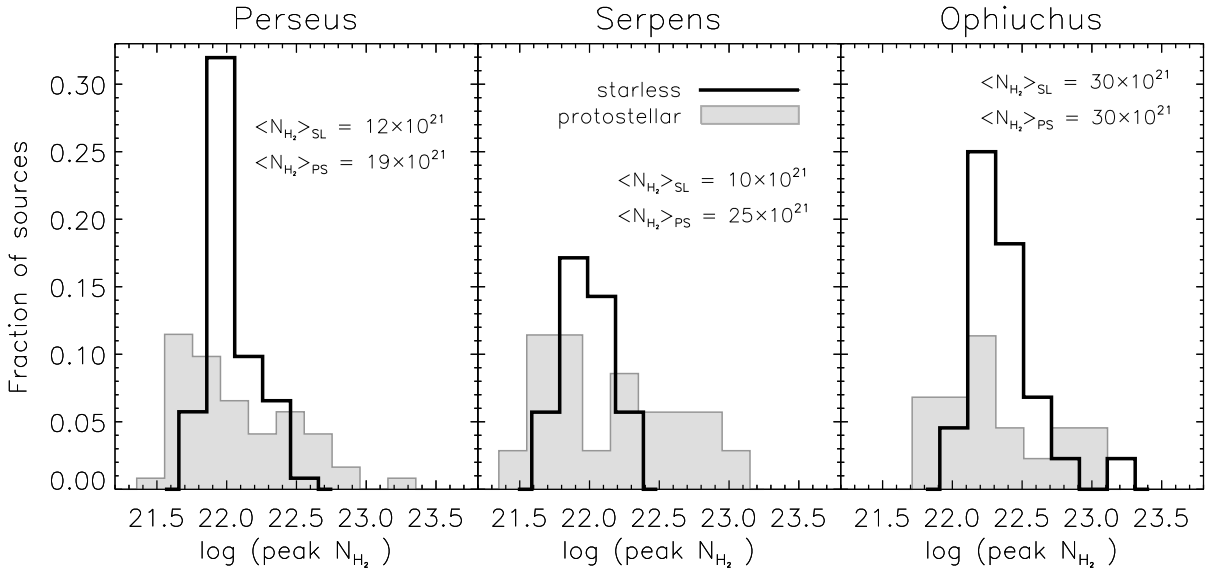

Figure 6.10 Distributions of the peak column density N_{H_2} of starless and protostellar cores in the three clouds. The peak N_{H_2} values of starless cores are considerably lower than those of protostellar cores in both Perseus ($\langle N_{H_2} \rangle = 12 \times 10^{21}$ cm^{-2} and $19{\times}10^{21}$ cm^{-2}, respectively) and Serpens ($\langle N_{H_2} \rangle = 10{\times}10^{21}$ cm^{-2} and $25{\times}10^{21}$ cm^{-2}). In Ophiuchus there is no difference in the mean values ($\langle N_{H_2} \rangle = 30 \times 10^{21}$ cm^{-2}), but in all three clouds the starless distribution is more peaked and the protostellar distribution is relatively flat.

starless cores than for protostellar cores in Perseus (figures 6.10 and 6.11, left panels), and the starless core distributions are much narrower. The average peak N_{H_2} for starless cores in Perseus is 12×10^{21} cm^{-2}, while the average peak N_{H_2} for protostellar cores is 50% higher, 19×10^{21} cm^{-2}, with a much wider dispersion. Similarly, the typical mean density of starless cores (1.3×10^5 cm^{-3}) is more than a factor of three smaller than that of protostellar cores (4.8×10^5 cm^{-3}). The large difference in mean densities in Perseus is due primarily to the significantly smaller sizes of protostellar cores. Recently, Jørgensen et al. (2007) found a similar result for Perseus, comparing SCUBA 850 μm cores with and without internal luminosity sources, as determined using *Spitzer* c2d data. Those authors concluded that cores with embedded YSOs (within 15″ of the core position) have higher "concentrations" on average.

Unlike the large differences seen between Perseus and Serpens when looking at core sizes, the distributions of peak and mean densities for starless and protostellar cores

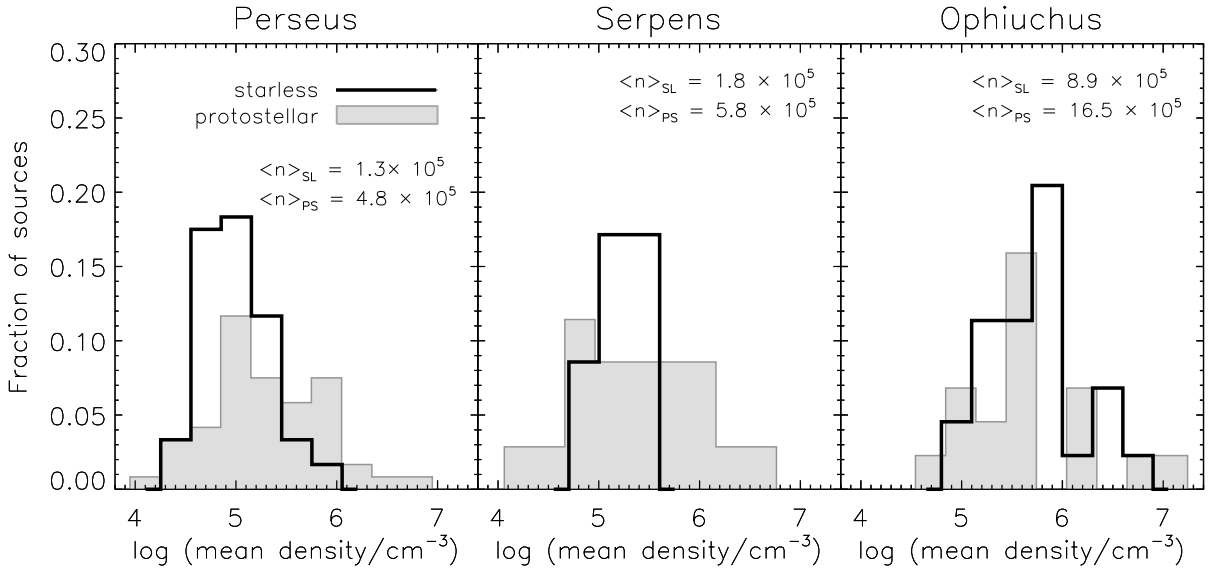

Figure 6.11 Distributions of the mean densities $\langle n \rangle$ of starless and protostellar cores. As for the peak N_{H_2} distribution (figure 6.10), starless cores tend to have lower mean densities than protostellar cores in Perseus and Serpens, by approximately a factor of three. In Ophiuchus, by contrast, there is almost no difference between the two distributions. Higher mean densities on average in Ophiuchus are a result of the higher linear resolution in that cloud (see text and §5.4).

in Serpens (figures 6.10 and 6.11, middle panels) are quite similar to those in Perseus. Average peak densities are substantially smaller for starless ($\langle N_{H_2} \rangle = 10 \times 10^{21}$ cm^{-2}) than for protostellar ($\langle N_{H_2} \rangle = 25 \times 10^{21}$ cm^{-2}) cores, and form a much narrower distribution. Likewise, the typical mean density of starless cores (1.8×10^5 cm^{-3}) is more than three times smaller than that of protostellar cores (5.8×10^5 cm^{-3}). In contrast to Perseus, mean density differences in Serpens are entirely due to the significantly larger masses of protostellar cores in that cloud, as starless cores are slightly smaller on average than protostellar cores in Serpens.

As was also the case for core sizes and shapes, there is essentially no difference between the peak and mean densities of starless and protostellar cores in Ophiuchus (figures 6.10 and 6.11, right panels). Average peak densities are the same ($\langle N_{H_2} \rangle = 30 \times 10^{21}$ cm^{-2}), and the two distributions have similar dispersions The average mean density is slightly higher for protostellar than for starless cores (17×10^5 cm^{-3}

versus 9×10^5 cm^{-3}), but the difference is primarily due to a few very high density protostellar cores. Larger mean densities in general in Ophiuchus compared to the other two clouds are likely not significant, but a consequence of the higher linear resolution in Ophiuchus, and resulting smaller linear deconvolved sizes (§5.4). This conjecture is confirmed using the "convolved" Ophiuchus sample, or the sample of sources extracted from the Ophiuchus map after having convolved it with a larger beam ($62''$) to simulate putting it at the same distance as Perseus and Serpens. The median peak N_{H_2} values for starless and protostellar cores in the convolved sample are both 10×10^{21} cm^{-2}, while the median mean densities are 1.2×10^5 cm^{-3} and 1.0×10^5 cm^{-3}, respectively, closer to those in Perseus and Serpens.

To summarize, the peak N_{H_2} and mean densities of starless cores in Perseus and Serpens are lower on average than for protostellar cores, whereas in Ophiuchus there is no difference between the starless and protostellar populations. Note that an error in the assumed dust temperature of approximately 30% for either protostellar or starless cores would bring the average peak N_{H_2} values of these two populations into agreement for Perseus and Serpens. The N_{H_2} distribution of starless cores does appear more peaked than that of protostellar cores in Ophiuchus, however, as in the other two clouds. Higher mean densities in Ophiuchus compared to the other clouds are found to be a result of the higher linear resolution, rather than a physical difference.

6.4.3 The Mass versus Size Distribution

Figure 6.12 shows the total core mass versus angular FWHM size for starless and protostellar cores in Perseus. There is a striking difference between the starless and protostellar distributions; in particular, starless cores seem to follow a constant surface density ($M \propto R^2$) curve, consistent with the narrow distribution of peak densities. Protostellar cores, in contrast, have a narrower range of sizes for a similar range of masses. This is another way of visualizing the result found earlier, that protostellar cores are smaller and have higher densities than starless cores. Looking at this plot, it is easy to imagine how protostellar cores in Perseus might have evolved from the

current population of starless cores, by decreasing in size and increasing in density for a constant mass, until collapse and protostellar formation is triggered. Equivalently, the formation of a central protostar within a previously starless core is associated with a decrease in core size and an increase in core density.

Note that because the completeness limits as a function of size (dashed for starless cores and dash-dot for protostellar cores) are similar to $M \propto R^2$, the distribution of starless cores in mass and size only implies that the upper envelope of cores follows a constant surface density curve. For example, there could be a population of large, low mass cores that we are unable to detect. Nevertheless, the two populations clearly fill different regions of the mass versus size parameter space. Empirical 50% completeness

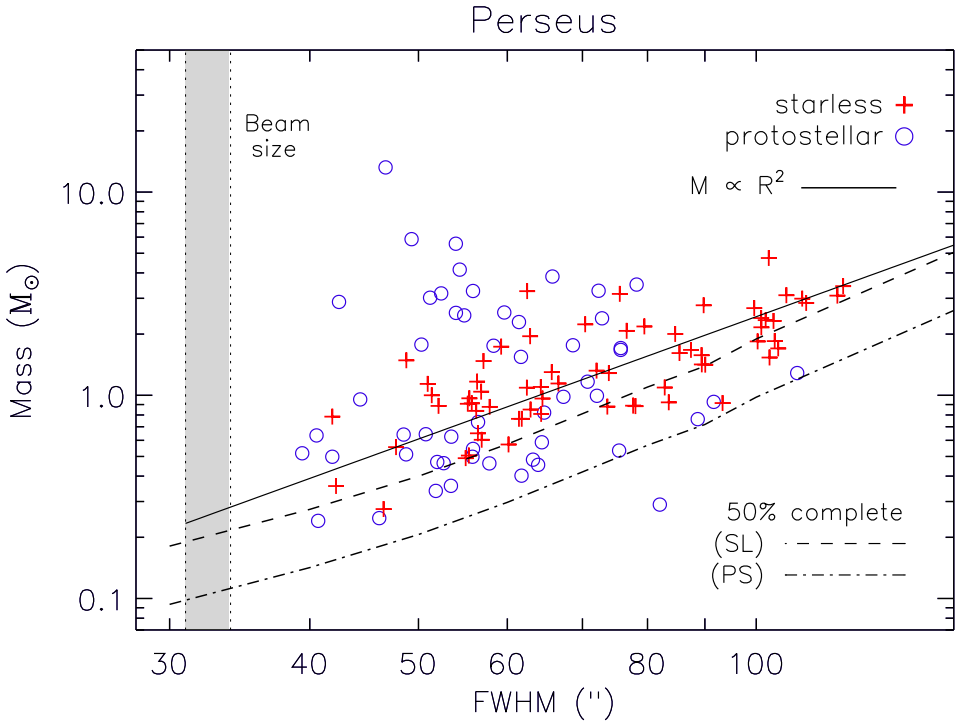

Figure 6.12 Total mass versus average angular FWHM size for starless and protostellar cores in Perseus. Starless cores tend to follow an $M \propto R^2$ relationship (solid line), while protostellar cores have a wide range in masses for a relatively small range in sizes. Thus there is a relatively simple explanation for how protostellar cores might have evolved from starless cores, getting smaller and denser for the same mass until protostellar formation is triggered. Dashed and dash-dot lines indicate empirically derived 50% completeness limits for starless and protostellar cores, respectively.

limits are derived using Monte Carlo simulations, by inserting simulated sources of increasing sizes into the real maps.

Such a simple explanation of the relationship between the protostellar and starless populations is not consistent with the other clouds, however, as shown in figure 6.13. Although protostellar cores in Serpens have a similarly small range in sizes for a large range of masses, as seen in Perseus, there is no population of large starless cores in Serpens. In fact, it is unclear how the relatively high mass protostellar cores in Serpens could have evolved from the compact, low mass population of starless cores. This discrepancy raises the possibility that the Serpens cloud has used up its reserve of relatively massive prestellar cores, and any future star formation in the cloud

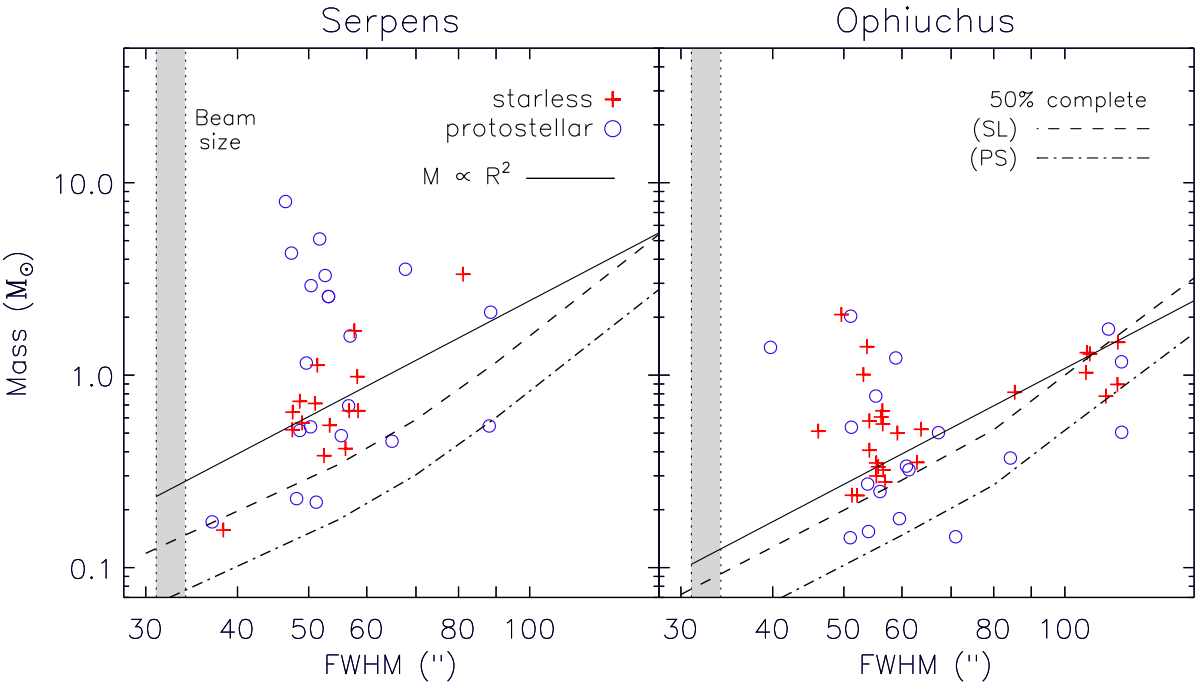

Figure 6.13 Total mass versus angular FWHM size for protostellar and starless cores in Serpens and Ophiuchus. Unlike in Perseus (figure 6.12), starless cores do not necessarily follow a constant surface density ($M \propto R^2$) line. Strikingly, there is no population of large starless cores in Serpens that might be expected to eventually evolve to resemble the current protostellar population in that cloud. In contrast, the properties of starless and protostellar cores are indistinguishable in Ophiuchus. Dashed and dash-dot lines indicate empirically derived 50% completeness limits for starless and protostellar cores, respectively.

will result in stars of lower mass than those of the current protostellar population. In contrast to both Perseus and Serpens, there is essentially no difference between the starless and protostellar populations in Ophiuchus, suggesting that protostellar formation results in very little core evolution for sources in that cloud.

6.4.4 Core Mass Distributions

Differential core mass distributions (CMDs) for the starless and protostellar core samples are shown for each cloud in figure 6.14. Note that the empirically derived 50% completeness limits for averaged size sources (dashed lines) occur at lower masses for protostellar cores, because a higher dust temperature is assumed (T_D = 15 K) than for starless cores (T_D = 10 K). For each distribution, we fit a single power law ($dN/dM \propto M^{\alpha}$) above the 50% completeness limit.

In Perseus (upper left panel), the protostellar core mass distribution is considerably wider than the starless distribution and extends to higher masses, despite the fact that there are fewer sources in the protostellar sample. Furthermore, the best-fit power law slope is shallower for protostellar cores ($\alpha = -1.7 \pm 0.1$) than for starless cores ($\alpha = -2.8 \pm 0.3$). A widening of the mass distribution is expected if the protostellar CMD originally looked like the starless CMD, and individual cores gradually moved to smaller masses as core material was accreted or ejected by the protostar. Larger masses in the protostellar distribution at the the high mass end of the CMDs are not expected in this scenario, however, unless the mass distribution from which the protostellar cores originated was shifted to higher masses than the current starless CMD. Another possibility, of course, is that we are underestimating the dust temperature T_D for protostellar cores, or overestimating T_D for starless cores.

In Serpens (upper right panel), the protostellar CMD is slightly wider than the starless distribution and has a shallow slope ($\alpha = -1.3 \pm 03$), even shallower than in Perseus. Due to the small number of starless cores in Serpens (15), the starless mass distribution is very noisy, and we are unable to fit a power law slope with reasonable confidence. It is clear, however, that there are significantly more protostellar cores

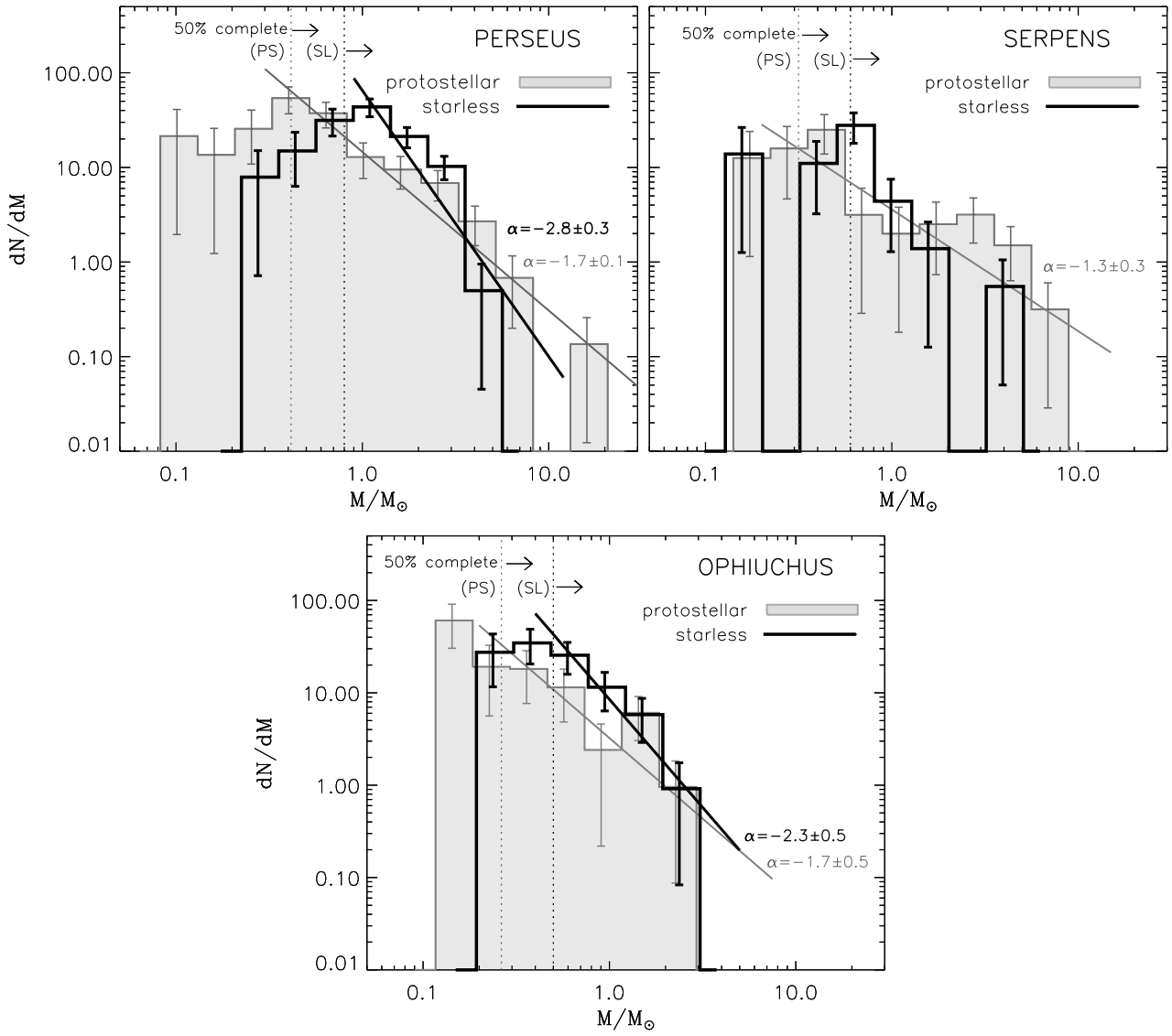

Figure 6.14 Differential core mass distributions (CMDs) of protostellar and starless cores in the three clouds. Empirical 50% completeness limits for average sized sources in each population are shown (dotted lines), and we fit power law slopes above those limits. The protostellar distributions appear to be wider and flatter in all three clouds, as expected if the protostellar CMDs have their origin in the starless CMDs and the distributions have shifted to lower masses as core material is accreted by the protostars within the protostellar cores. The starless CMD for Serpens is too noisy to fit a slope with any reasonable confidence.

than starless cores with high masses.

The slope of the protostellar distribution in Ophiuchus (lower panel) is again shallower ($\alpha = -1.7 \pm 0.5$) than that of the starless CMD ($\alpha = -2.3 \pm 0.5$). In

fact, the slope of the protostellar distribution is the same as was found for Perseus. In contrast to Perseus, however, the two distributions have quite similar widths, and the protostellar CMD extends to only slightly smaller masses. Unlike for the other two clouds, the Ophiuchus CMDs are completely consistent with the idea that the protostellar CMD was originally identical to the current starless CMD, and core evolution after protostellar formation moved some protostellar cores to lower masses. If this is indeed the case, the highest mass protostellar cores must contain quite young protostars, having evolved very little in mass since protostellar formation.

6.4.5 Relationship to Cloud Column Density

We use the cumulative fraction of starless and protostellar cores as a function of cloud A_V, shown in figure 6.15, to quantify the relationship between dense cores and the surrounding cloud material. The visual extinction (A_V) is a measure of the cloud column density, and is derived based on the reddening of background 2MASS and IRAC sources, as described in §4.3.1. In chapter 5, we found that 75% of 1.1 mm cores in Perseus, Serpens, and Ophiuchus are found at visual extinctions of $A_V \gtrsim 8$ mag, $A_V \gtrsim 15$ mag, and $A_V \gtrsim 20 - 23$ mag, respectively. Although these values do not define a strict threshold, below these A_V levels the likelihood of finding any 1.1 mm core is very low. Here we investigate if the relationship between dense cores and cloud column density is different for starless and protostellar cores.

Dotted lines in figure 6.15 identify the A_V level above which more than 75% of the 1.1 mm cores occur. In all three clouds the majority of cores are found at high cloud column density ($A_V > 7$ mag): 75% of starless and protostellar cores in Perseus are located at $A_V \gtrsim 7$ and 8.5 mag, respectively. The equivalent values are $A_V \gtrsim 9.5$ and 16 mag in Serpens, and $A_V \gtrsim 19.5$ and 23 mag in Ophiuchus. These values are quite similar to those found using the full core samples in chapter 5. Starless cores in Serpens tend to be found at somewhat lower A_V than protostellar cores, but this may be a consequence of small number statistics as there are only 15 starless and 20 protostellar cores in Serpens. In the other clouds, there is very little difference between

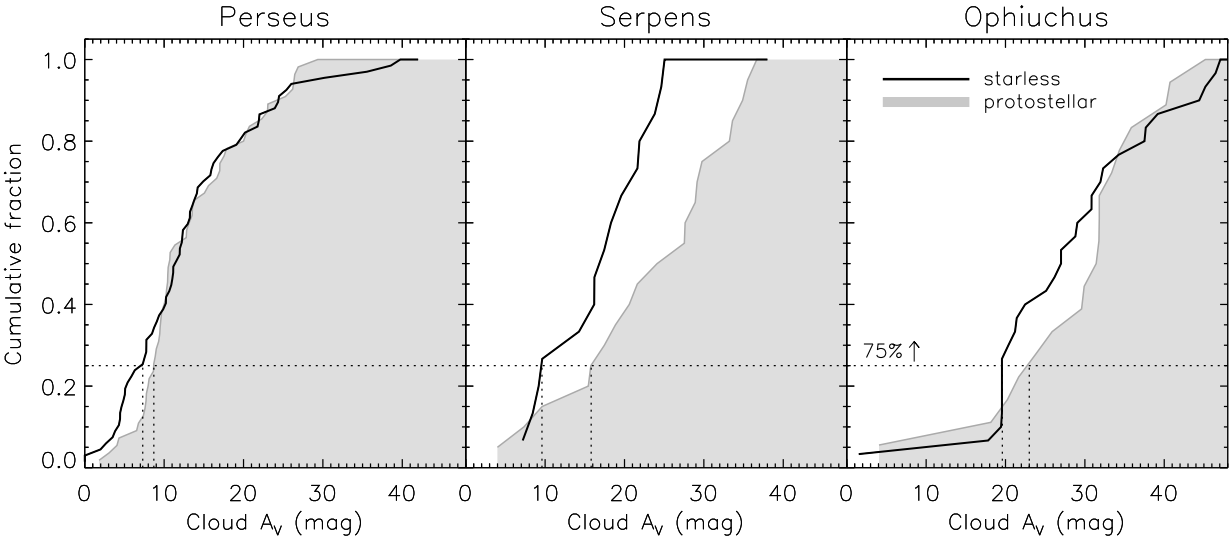

Figure 6.15 Cumulative fraction of starless and protostellar cores as a function of the cloud A_V in Perseus, Serpens, and Ophiuchus. In all three clouds, most cores are found at high cloud column density ($A_V > 7$ mag): 75% of starless and protostellar cores in Perseus are located at $A_V \gtrsim 7$ and 8.5 mag, respectively. The equivalent values are $A_V \gtrsim 9.5$ and 16 mag in Serpens, and $A_V \gtrsim 19.5$ and 23 mag in Ophiuchus. Except in Serpens, where starless cores are found at slightly lower A_V values, there is very little difference between the starless and protostellar core populations. Only Ophiuchus shows evidence for a strict extinction threshold, at $A_V \sim 17$ mag.

the starless and protostellar populations. Only in Ophiuchus does there appear to be a true extinction threshold for finding 1.1 mm cores; only one protostellar and one starless core is found at $A_V < 17$ mag in this cloud.

As discussed in chapter 5, an extinction threshold has been predicted by McKee (1989) for photoionization-regulated star formation in magnetically supported clouds. In this model, core collapse and star formation will occur only in shielded regions of a molecular cloud where $A_V \gtrsim 4 - 8$ mag. The fact that 75% of both protostellar and starless cores are found above $A_V = 7$ mag in each cloud is consistent with this model, and suggests that magnetic fields must be important, at least in the low column density regions of molecular clouds.

6.4.6 Clustering

Finally, we look at the spatial clustering of starless and protostellar cores, as measured by the two-point correlation function (figure 6.16), where $H(r)$ and $w(r)$ are defined as in chapter 2. In essence, $w(r)$ is the excess clustering in the sample as compared to a random distribution of sources. The upper panels of figure 6.16 plot $w(r)$ as a function of source separation r, with the linear beam size and average source size indicated. The lower panels plot $\log(w)$, with a power law fit ($w(r) \propto r^p$) for r larger than the average source size. The amplitude of $w(r)$ is a measure of the degree of clustering above a random distribution, while the slope is a measure of how quickly clustering falls off on increasing scales.

Although visually starless and protostellar cores tend to cluster in a similar way, the amplitude of $w(r)$ is higher for the protostellar samples in all three clouds. This behavior suggests that clustering is stronger on all spatial scales for protostellar cores. In Serpens (middle panel), the slope of the starless and protostellar distributions are quite similar ($p = -1.4 \pm 0.3$ and -1.3 ± 0.6). In Perseus and Ophiuchus, however, the slope of the starless distribution is shallower, by approximately 4σ in Perseus and 2σ in Ophiuchus ($p = -1.14 \pm 0.13$ and -1.5 ± 0.1 for starless and protostellar cores in Perseus, and -1.3 ± 0.3 and -2.2 ± 0.4 in Ophiuchus). Shallower slopes for the starless samples suggest that although the amplitude of clustering is weaker for starless cores, it does not fall off as fast at larger spatial scales.

A lower degree of clustering for starless cores as compared to protostellar cores in Perseus and Serpens is confirmed by calculating the peak number of cores per square parsec (see §5.5.4). In Perseus, the peak number of starless cores is 10 pc^{-2}, compared to 16 pc^{-2} for protostellar cores. Likewise, in Serpens the peak number of starless cores is 4 pc^{-2}, and the peak number of protostellar cores 8 pc^{-2}, suggesting that clustering in the protostellar samples is a factor of 1.5–2 times stronger than in the starless samples for these clouds. In Ophiuchus, however, the values of the starless and protostellar populations are identical (12 pc^{-2}).

There are two plausible reasons that clustering might be stronger for protostellar

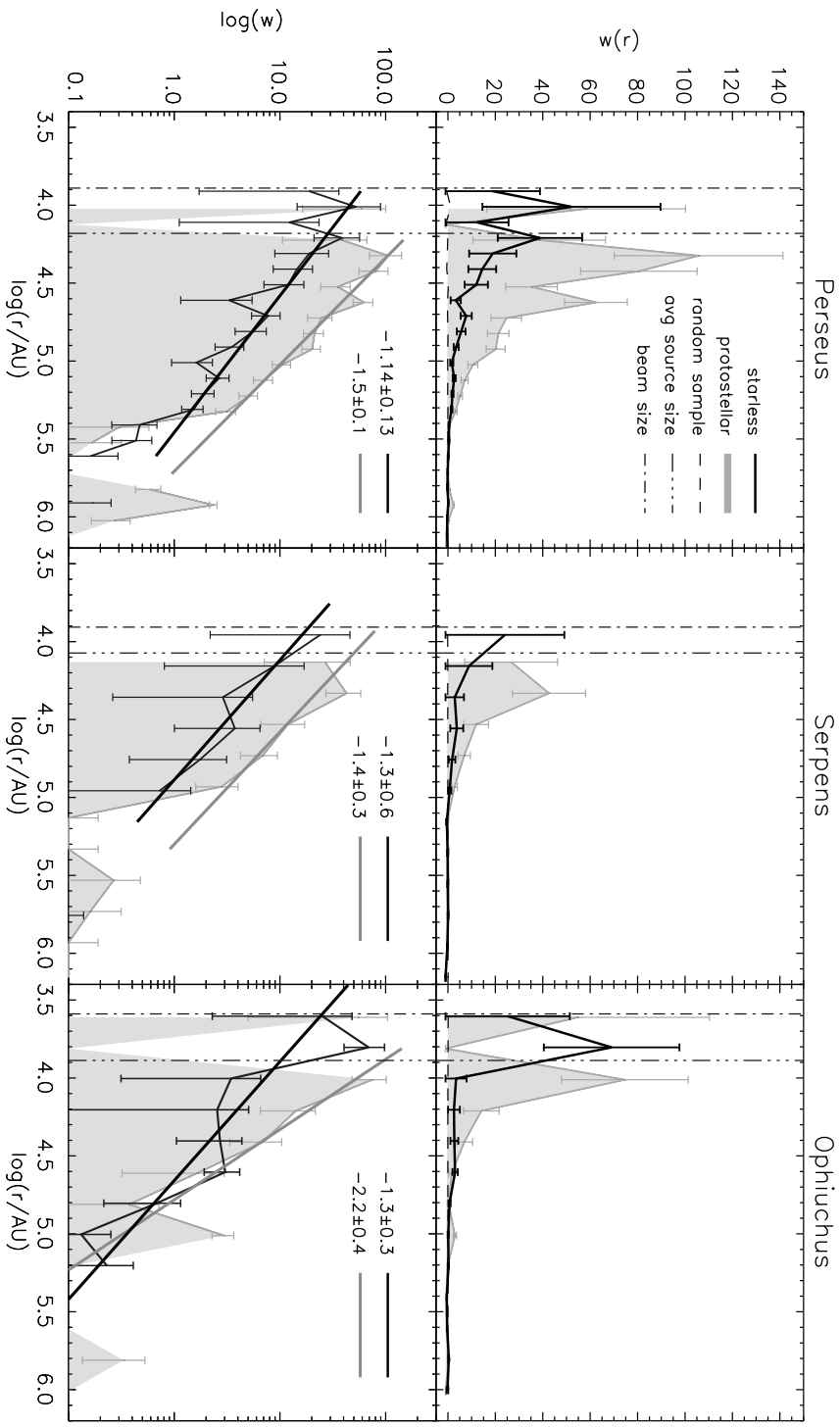

Figure 6.16 Two-point correlation function $w(r)$, as a function of source separation r, for protostellar and starless cores in Perseus, Serpens, and Ophiuchus (upper panels). The lower panel plots $\log(w)$, with the best fitting power law slope to each distribution, where slopes are fit above the average source size in each cloud. The amplitude of the protostellar $w(r)$ is consistently higher than the starless $w(r)$, suggesting that clustering is stronger on all spatial scales for the protostellar samples. In Perseus, the slope of the starless distribution is shallower, indicating that clustering does not fall off as quickly on large scales.

cores, one environmental and one evolutionary. The difference may be an environmental effect if cores that are located in regions of the cloud with higher gas density are more likely to collapse to form protostars. In this case, more clustered sources would tend to be protostellar rather than starless. If evolution plays a more important role, however, the spatial distribution of cores might evolve after protostellar formation, for example as a result of dynamical effects.

6.5 The Prestellar Core Mass Distribution

One very important measure of the initial conditions of star formation is the prestellar core mass distribution (CMD). In particular, comparing the prestellar CMD to the stellar initial mass function (IMF) gives us insight into how the final masses of stars are determined. In the simplest case, there are two possible processes that might dictate what the final mass of forming star will be. If stellar masses are determined by the initial fragmentation into cores, i.e., the final star mass is always a fixed percentage of the original core mass, then the shape of the emergent stellar IMF should closely trace that of the starless CMD (e.g., Myers et al., 1998). This might be expected in crowded regions where the mass reservoir is limited to a protostar's nascent core. If, on the other hand, stellar masses are determined by competitive accretion (Bonnell et al., 2001) or by the protostars themselves through feedback mechanisms (e.g., outflows and winds, Shu et al. 1987), we would not expect the emergent IMF to reflect the original clump mass function (Adams & Fatuzzo, 1996).

We assume that all starless cores in our 1.1 mm samples will eventually form stars, and thus are true prestellar cores. While it is possible that some fraction of the starless cores are transient or stable structures that will never collapse to form a protostar, the cores detected by our Bolocam surveys have high mean densities ($n > 2 - 3 \times 10^4$ cm^{-3}; chapter 5), making them likely to be prestellar (Gregersen & Evans, 2000; Di Francesco et al., 2007). We attempt to estimate if cores are gravitationally bound by comparing the measured core masses to the Jeans mass for

material with the same mean density, where

$$M_J = \frac{a^3}{\rho^{0.5} G^{1.5}} = 1.6 \text{ M}_\odot \left(\frac{n_{H_2}}{10^4 \text{cm}^{-3}}\right)^{-0.5}, \tag{6.2}$$

for a temperature of 10 K and internal support due to thermal motions only (Jeans, 1928). Using the mean particle density of each core to calculate the local Jeans mass, we find that nearly all sources have $M > M_J$, with median M/M_J ratios of 2.4 in Perseus, 1.5 in Serpens, and 2.4 in Ophiuchus. Thus the large majority of starless cores are likely to be bound or unstable, although there may be additional means of core support, such as turbulence or magnetic fields (e.g., Evans, 1999). Future comparison of our data to molecular line observations of the Bolocam cores in Perseus, recently acquired as part of the COMPLETE project, will provide a more robust method of determining if cores are in virial equilibrium, and for distinguishing prestellar from unbound starless cores.

Combining the starless core samples from all three clouds, and using $T_D = 10$ K to calculate the mass, results in the prestellar CMD shown in figure 6.17. The highest empirical completeness limit is in the Perseus sample, where the 50% completeness for averaged size sources (70″) is 0.8 $\text{M}_\odot$. The completeness limit is lower in Serpens (0.6 $\text{M}_\odot$) and Ophiuchus (0.5 $\text{M}_\odot$), but as more than half of the total population of starless cores are in Perseus, we adopt 0.8 $\text{M}_\odot$ for the entire sample.

We fit a power law ($dN/dM \propto M^\alpha$) to the CMD for $M > 0.8$ $\text{M}_\odot$, finding a slope of $\alpha = -2.5 \pm 0.2$, with a reduced chi-squared of $\tilde{\chi}^2 = 3.1$. We also fit a lognormal distribution (equation (1.7)) to $M > 0.3$ $\text{M}_\odot$, finding a best-fit width $\sigma = 0.30 \pm 0.03$ and characteristic mass $M_0 = 1.0 \pm 0.1$ $\text{M}_\odot$. Although the lognormal function is quite a good fit ($\tilde{\chi}^2 = 0.5$), the reliability of the turnover in the prestellar CMD is highly questionable, given that the completeness limit in Perseus coincides closely with the turnover mass. The prestellar CMD can also be fitted by a broken power law with $\alpha = -4.3 \pm 1.1$ for $M > 2.5$ $\text{M}_\odot$ and $\alpha = -1.7 \pm 0.3$ for $M < 2.5$ $\text{M}_\odot$, although the uncertainties are large. Two recent estimates for the IMF shape are also shown in figure 6.17 for reference.

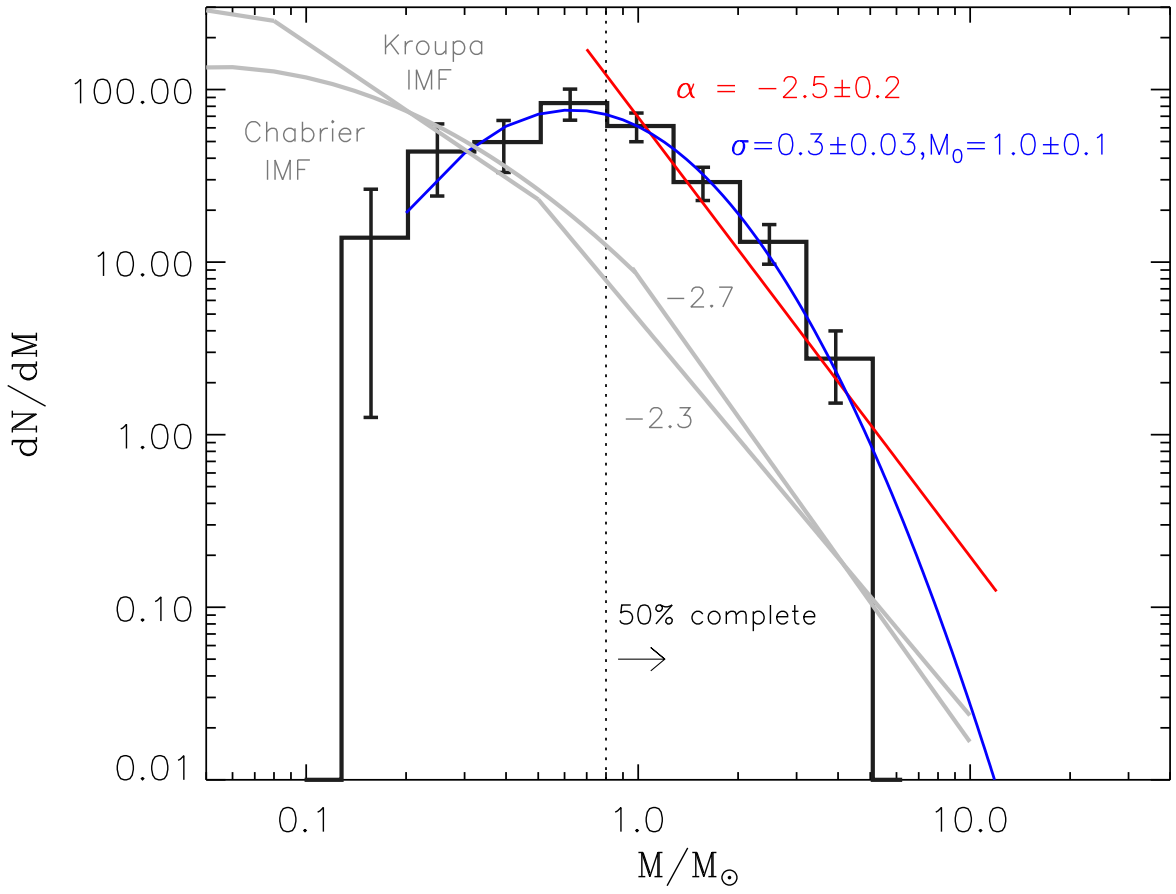

Figure 6.17 Combined prestellar core mass distribution, with power law (red curve) and lognormal (blue curve) fits. The prestellar sample is composed of all starless cores from Perseus, Serpens, and Ophiuchus, and the 50% mass completeness limit is defined by the completeness to average sized cores in Perseus, the least deep cloud. Recent measurements of the stellar IMF ($\alpha = -2.3$ to -2.8) are similar to the best fit power law slope ($\alpha = -2.5$). Slopes of $\alpha = 2.3$ and 2.7 are shown for reference (thick gray lines), as are IMF fits for low masses from Chabrier (2005) and Kroupa (2002).

For comparison, we show in figure 6.18 the CMD of the *protostellar* core sample combined from all three clouds, and assuming $T_D = 15$ K. The protostellar CMD is considerably wider and flatter than the starless CMD. The best-fitting power law slope ($\alpha = -1.9 \pm 0.2$; $\tilde{\chi}^2 = 1.7$) is shallower than for the starless sample, and the best-fitting lognormal distribution ($\sigma = 0.51 \pm 0.07$, $M_0 = 0.8 \pm 0.2$; $\tilde{\chi}^2 = 1.3$) is wider by nearly a factor of two. It is also possible to fit the protostellar distribution

with a broken power law: $\alpha = -2.8 \pm 0.4$ ($M > 2$ M$_\odot$) and $\alpha = -1.3 \pm 0.2$ (0.3 M$_\odot$ $< M < 2$ M$_\odot$). A protostellar CMD that extends to lower masses than the starless CMD is expected, given that some fraction of mass has already been accreted on to the central source for protostellar cores. An extension to higher masses in the protostellar CMD as compared to the starless CMD, however, can only be explained if (a) we are underestimating the dust temperature of protostellar sources, (b) masses of protostellar cores are overestimated due to blending in clustered regions, or (c) the current populations of prestellar cores in these clouds have lower mass than the generation of cores that have already formed protostars.

The shape of the local IMF is still uncertain (Scalo, 2005), but recent work has found evidence for a slope of $\alpha = -2.3$ to -2.8 for stellar masses $M \gtrsim 1$ M$_\odot$, quite similar to the slope we measure for the combined prestellar CMD ($\alpha = -2.5$). For example, Reid, Gizis, & Hawley (2002) find $\alpha = -2.5$ above 0.6 M$_\odot$, and $\alpha = -2.8$ above 1 M$_\odot$. Schröder & Pagel (2003) suggest $\alpha = -2.7$ for $1.1 < M < 1.6$ M$_\odot$ and $\alpha = -3.1$ for $1.6 < M < 4$ M$_\odot$. For reference, the Salpeter IMF has a slope of $\alpha = -2.35$ (Salpeter, 1955), and the Scalo (1986) slope for sources with mass $M \gtrsim 1$ M$_\odot$ is $\alpha \sim -2.7$) At lower masses, the IMF flattens, and may be characterized by a lognormal function. Kroupa (2002) suggests a three-component power law for the average single-star IMF: $\alpha = -2.3$ for $0.5 < M < 1$ M$_\odot$, $\alpha = -1.3$ for $0.08 < M < 0.5$ M$_\odot$, and $\alpha = -0.3$ for $0.01 < M < 0.08$ M$_\odot$. Chabrier (2005) finds that a lognormal distribution with $\sigma = 0.55$ and $M_0 = 0.25$ $M_\odot$ is a good fit for $M < 1$ M$_\odot$. The system IMF, i.e., treating binaries and multiple systems as single rather than multiple objects, peaks at approximately $0.2 - 0.3$ M$_\odot$ (e.g., Chabrier, 2005; Luhman et al, 2003). This system IMF is appropriate for comparison to our CMDs, which would not resolve these multiple systems even if they form from distinct cores.

The Kroupa (2002) three-component power law and the Chabrier (2005) lognormal IMF joined with $\alpha = -2.7$ for $M > 1$ M$_\odot$ are shown as thick gray lines in figure 6.17. The width of the Chabrier (2005) IMF lognormal is somewhat larger than the width of the prestellar CMD best-fit lognormal ($\sigma = 0.3$), expected if we are incomplete

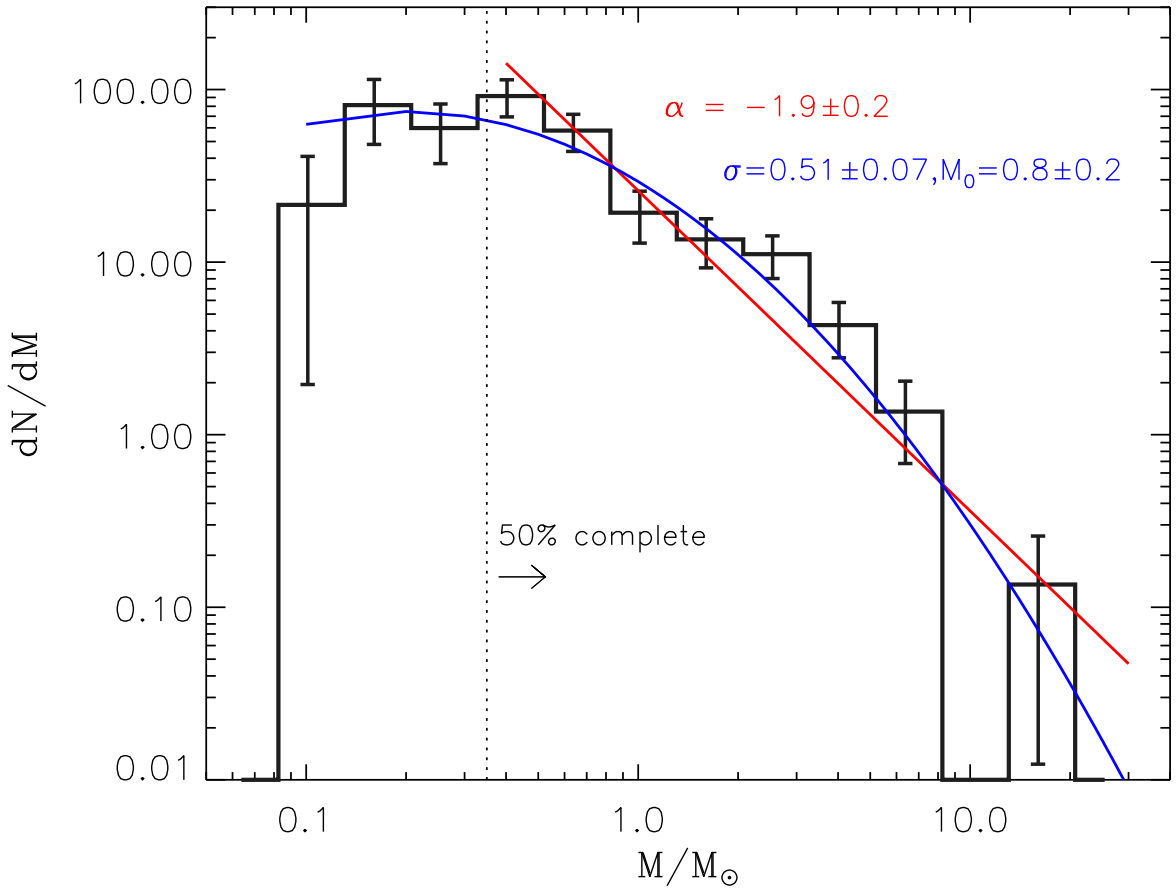

Figure 6.18 Combined protostellar mass distribution, with power law (red) and lognormal (blue) fits. The protostellar CMD includes all protostellar cores from Perseus, Serpens, and Ophiuchus, and the 50% mass completeness limit is defined by the completeness to average sized protostellar cores in Perseus. The best-fit power law ($\alpha = -1.9$) is shallower, and the distribution as a whole wider, than the prestellar CMD (figure 6.17), as expected if the protostellar CMD evolved from the prestellar CMD. Higher masses than the prestellar CMD are more difficult to explain, however.

at lower masses, and the IMF characteristic mass (0.25 $M_\odot$) is a factor of four lower than that of the CMD (1.0 $M_\odot$). A lower characteristic mass for the IMF is expected if some fraction of the core mass is lost in the star-formation process. The power law slopes for $M > 1$ $M_\odot$ appear to be quite similar for the CMD and IMF, however. While we cannot rule out the importance of feedback and other local processes, the fact that the prestellar CMD and the local IMF have similar shapes provides support

for the hypothesis that the final masses of stars are already determined during the core formation process.

If the prestellar CMD does have a one-to-one relationship with the stellar IMF, then the ratio of turnover masses ($M_{\rm TO}^{\rm IMF}/M_{\rm TO}^{\rm CMD}$) is a measure of the core collapse efficiency $f_{\rm eff}$, or the fraction of original core mass that ends up in the final star. Equivalently, $M_{\rm TO}^{\rm CMD}/M_{\rm TO}^{\rm IMF} = 1 - f_{\rm eff}$ is the fraction of core mass lost in the star formation process. Our limited completeness dictates that we can only measure a lower limit to $f_{\rm eff}$. If there is a true turnover in the prestellar CMD, it occurs at $M_{\rm TO}^{\rm CMD} \lesssim 0.8$ M$_\odot$. For an IMF turnover mass of 0.25 M$_\odot$ (Chabrier, 2005), this value implies that least 30% of the initial core mass is accreted onto the final star. Characteristic masses associated with lognormal fits to both the IMF and CMD imply a similar ratio of at least $f_{\rm eff} \gtrsim M_0^{\rm IMF}/M_0^{\rm CMD} = 0.25/1.0 = 0.25$. There is a suggestion of a break in the CMD at $M \sim 2.5$ M$_\odot$. Comparing to the three-component Kroupa (2002) IMF, which has a break at $M = 0.5$ M$_\odot$, again implies that the CMD is similar in shape to the IMF but shifted to higher masses by about a factor of four.

Evidence for a direct link between the CMD and the IMF has been found previously based on dust emission surveys of small regions (Testi & Sargent, 1998; Motte et al., 1998), as well as molecular line observations of dense cores (Onishi et al. 2002; see also chapter 1 for more discussion). Recently, Alves et al. (2007) found evidence for a break in the mass distribution of dense cores in the Pipe Nebula, as traced by dust extinction toward background stars. Those authors interpret the similarity between the Pipe Nebula CMD and the Trapezium cluster IMF(Muench et al., 2002) as evidence that the stellar IMF is a direct product of the CMD, with a uniform core-to-star efficiency of 30% $\pm$ 10%. Although the measured masses of Alves et al. (2007) are somewhat less uncertain than ours because they do not need to assume a dust opacity or temperature, the mean densities of cores traced by dust extinction, $n \sim 5 \times 10^3 - 2 \times 10^4$ cm^{-3}, are considerably lower than the mean densities of cores traced by our Bolocam 1.1 mm surveys ($n \sim 1 - 8 \times 10^5$ cm^{-3}). Furthermore, extinction is sensitive to all material along the line of sight, and may be tracing diffuse structures that will never form stars. Despite these differences, however, the two

methods give similar results.

6.6 Properties of Cold Protostars

6.6.1 Bolometric Luminosity and Temperature

Our extensive wavelength coverage allows us to construct well-sampled SEDs for the cold protostar candidates in all three clouds, from which we calculate a bolometric luminosity (L_{bol}) and bolometric temperature (T_{bol}) for each source. The bolometric luminosity is calculated by integrating the SED S_ν over frequency:

$$L_{bol} = 4\pi d^2 \int S_\nu d\nu. \tag{6.3}$$

The bolometric temperature is defined as the temperature of a blackbody with the same mean frequency as the source SED, and is given by $T_{bol} = 1.35 \times 10^{-11} \langle \nu \rangle$ K (Myers & Ladd, 1993), where the mean frequency is

$$\langle \nu \rangle = \frac{\int \nu S_\nu d\nu}{\int S_\nu d\nu}. \tag{6.4}$$

Two methods for estimating the integrations over frequency for finitely sampled SEDs are discussed in the appendix (§6.11). We use the difference between the values calculated by the two methods to estimate overall uncertainties on measured L_{bol} and T_{bol} values of $20\% - 50\%$, depending on whether or not a 160 μm flux is available. Systematic errors introduced by missing 160 μm flux points are also investigated in §6.11. Without a 160 μm flux point, T_{bol} will almost certainly be an overestimate for very cold sources, which may affect our classification of protostellar candidates. Ophiuchus will be most affected, as only four sources in that cloud have reliable 160 μm fluxes. We will revisit this issue in §6.9, when we look at the relative number of Class 0 and Class I protostars.

Tables 6.2–6.4 list the bolometric temperatures and luminosities derived for all candidate protostars in each cloud that are associated with 1.1 mm emission. Sources

are listed by increasing T_{bol}, and identified as, e.g., "Pers-Cold#", as well as by their c2d name (SSTc2dJ...), which also gives the position. Note that the uncertainties given are formal errors from the midpoint integration only, and do not include our estimated systematic uncertainties of 20%–50%.

6.6.2 Envelope Mass

The envelope mass of candidate protostars, M_{env}, is calculated from the flux density at 1.1 mm using equation (6.1), by the same method used to derive the masses of protostellar cores. Of course, our protostellar "cores" and protostellar "envelopes" are often one and the same. We assume a dust temperature of $T_D = 15$ K for all protostellar envelopes, as discussed in §6.4.4. The temperature will be higher close to the protostar, but the majority of the envelope mass is in the outer, cooler, regions of the envelope. Envelope masses are listed in tables 6.2–6.4; if the source is associated with a particular core the Bolocam identification from chapters 2–4 is given in the last column. If the source is not associated with a distinct core, but rather the flux has been "band-filled" at 1.1 mm, then no Bolocam ID is given. Furthermore, only sources with measured fluxes at 1.1 mm are listed in tables 6.2–6.4. We ignore sources with upper limits at 1.1 mm because we are interested primarily in young, embedded sources, and those without emission at 1.1 mm are unlikely to have substantial envelopes.

6.6.3 Completeness

Because we require a detection at 1.1 mm to be included in the final source lists, we are clearly incomplete to objects more evolved than Class I, which do not have a substantial envelope. A few Class II sources with massive disks do appear in our sample, and are discussed in §6.6.4.3. It is possible that we are missing low luminosity cold objects that are below our 1.1 mm detection threshold, as the 1.1 mm detection requirement is more restrictive than our 24 μm flux criteria (e.g., Dunham et al., in preparation).

Taking the 1.1 mm detection limits for each cloud (75 mJy in Perseus, 50 mJy in Serpens, and 110 mJy in Ophiuchus), and assuming the spectrum of a modified blackbody, $S_\nu = \nu^\beta B_\nu(T)$ with $T = 15$ K, we can estimate the minimum detectable bolometric luminosity in each cloud. For $\beta = 1$, the minimum L_{bol} is 0.02 $L_\odot$ in Perseus, 0.01 $L_\odot$ in Serpens, and 0.006 $L_\odot$ in Ophiuchus. Assuming $T = 20$ K raises these values by approximately a factor of 2, while taking $\beta = 2$ causes an increase of a factor of 4. Although these are very rough estimates, they agree fairly well with the lowest observed bolometric luminosities for sources with 1.1 mm detections (0.04 $L_\odot$ in Perseus, 0.05 $L_\odot$ in Serpens, and 0.01 $L_\odot$ in Ophiuchus). Harvey et al. (2007a) demonstrates that the c2d *Spitzer* surveys of Serpens are complete at the 50% level to young objects with luminosities as low as $0.01 L_\odot$, and at the 90% level to $0.05 L_\odot$.

Table 6.2. Bolometric temperatures, luminosities, and envelope masses of cold protostars in Perseus

ID	c2d name/position (SSTc2dJ...)	T_{bol} (K)	L_{bol} ($L_\odot$)	M_{env}[1] ($M_\odot$)	Bolocam ID[2]
		Class 0			
Pers-cold1	034356.74+320050.1	24 (3)	1.5 (0.14)	3.02 (0.08)	Bolo 103
Pers-cold2	033217.95+304947.4	25 (1)	1.3 (0.04)	2.88 (0.08)	Bolo 66
Pers-cold3	032900.70+311200.0	30 (11)	0.69 (0.2)	0.29 (0.03)	Bolo 41
Pers-cold4	032839.10+310601.7	31 (1)	0.22 (0.01)	0.36 (0.02)	Bolo 30
Pers-cold5	033120.96+304530.0	33 (2)	1.20 (0.04)	0.95 (0.04)	Bolo 65
Pers-cold6	033314.40+310710.8	36 (12)	0.64 (0.18)	1.04 (0.10)	Bolo 79
Pers-cold7	034443.94+320136.1	40 (10)	3.0 (0.66)	0.63 (0.06)	Bolo 116
Pers-cold8	032951.82+313906.0	41 (2)	0.46 (0.02)	0.64 (0.04)	Bolo 59
Pers-cold9	033316.56+310651.8	47 (1)	0.27 (0.01)	1.57 (0.16)	Bolo 79
Pers-cold10	034357.10+320304.2	49 (1)	0.45 (0.01)	1.78 (0.04)	Bolo 104
Pers-cold11	032910.50+311330.9	51 (5)	4.2 (0.28)	7.75 (0.78)	Bolo 48
Pers-cold12	032902.36+311533.9	53 (1)	2.40 (0.01)	1.87 (0.19)	Bolo 43
Pers-cold13	032912.04+311301.7	54 (26)	1.4 (0.49)	3.66 (0.37)	Bolo 48
Pers-cold14	032913.45+311355.5	54 (1)	0.49 (0.01)	0.5 (0.05)	Bolo 48
Pers-cold15	032911.11+312202.8	55 (1)	9.90 (0.03)	0.64 (0.06)	
Pers-cold16	032904.05+311446.5	56 (26)	0.53 (0.17)	1.16 (0.12)	
Pers-cold17	034350.95+320324.7	56 (25)	0.38 (0.12)	1.15 (0.11)	Bolo 102
Pers-cold18	032739.09+301303.1	59 (8)	4.2 (0.49)	0.51 (0.03)	Bolo 22
Pers-cold19	032911.25+311831.4	59 (27)	2.8 (0.94)	2.47 (0.07)	Bolo 49
Pers-cold20	032923.49+313329.5	60 (3)	0.36 (0.01)	0.64 (0.05)	Bolo 57
Pers-cold21	032743.23+301228.8	60 (3)	1.70 (0.06)	0.50 (0.03)	Bolo 23
Pers-cold22	032855.56+311436.8	61 (4)	18.0 (0.48)	2.81 (0.28)	Bolo 38
Pers-cold23	033313.78+312005.2	63 (17)	0.11 (0.03)	0.41 (0.04)	Bolo 78
Pers-cold24	032910.68+311820.6	63 (5)	2.8 (0.17)	2.47 (0.07)	Bolo 49
Pers-cold25	032522.33+304513.9	63 (5)	1.7 (0.11)	1.41 (0.14)	Bolo 5
Pers-cold26	032917.16+312746.4	66 (6)	0.29 (0.02)	0.5 (0.05)	Bolo 52
Pers-cold27	032845.30+310541.9	67 (3)	0.43 (0.02)	0.19 (0.02)	Bolo 33
Pers-cold28	032637.46+301528.0	68 (4)	0.95 (0.04)	0.5 (0.08)	Bolo 18
Pers-cold29	032538.82+304406.1	69 (5)	4.4 (0.26)	1.87 (0.19)	Bolo 10
		Class I			
Pers-cold30	034351.02+320308.1	72 (6)	0.28 (0.02)	0.62 (0.06)	Bolo 102
Pers-cold31	032832.55+311105.1	74 (21)	0.18 (0.05)	0.19 (0.02)	Bolo 25
Pers-cold32	033317.85+310931.9	76 (6)	1.8 (0.11)	3.84 (0.09)	Bolo 80
Pers-cold33	033327.28+310710.2	78 (5)	1.7 (0.06)	0.59 (0.06)	Bolo 84
Pers-cold34	034402.40+320204.9	84 (6)	0.16 (0.01)	0.63 (0.02)	Bolo 106

Table 6.2 (cont'd)

ID	c2d name/position (SSTc2dJ...)	T_{bol} (K)	L_{bol} ($L_\odot$)	M_{env}[1] ($M_\odot$)	Bolocam ID[2]
Pers-cold35	032536.48+304522.1	90 (6)	4.3 (0.22)	4.47 (0.45)	Bolo 8
Pers-cold36	033015.12+302349.3	99 (6)	1.6 (0.06)	0.46 (0.07)	Bolo 60
Pers-cold37	032837.16+311331.6	103 (6)	9.1 (0.3)	0.44 (0.04)	Bolo 29
Pers-cold38	032857.36+311415.8	106 (7)	5.3 (0.27)	0.74 (0.07)	Bolo 38
Pers-cold39	032918.27+312319.8	106 (8)	0.07 (0.01)	0.44 (0.04)	Bolo 54
Pers-cold40	033229.18+310240.8	115 (3)	0.54 (0.01)	0.45 (0.08)	Bolo 68
Pers-cold41	033316.66+310755.1	132 (8)	1.5 (0.07)	1.12 (0.11)	
Pers-cold42	033320.30+310721.4	157 (8)	0.17 (0.01)	1.50 (0.15)	Bolo 81
Pers-cold43	032539.10+304358.1	163 (12)	0.68 (0.04)	1.82 (0.18)	Bolo 10
Pers-cold44	034202.16+314802.0	176 (12)	0.07 (0.01)	0.07 (0.02)	
Pers-cold45	033309.57+310531.1	197 (12)	0.05 (0.01)	0.21 (0.02)	
Pers-cold46	032903.76+311604.9	202 (16)	23.0 (1.4)	3.25 (0.32)	Bolo 43
Pers-cold47	032800.40+300801.2	221 (9)	0.3 (0.01)	0.17 (0.02)	
Pers-cold48	032834.50+310051.0	230 (9)	1.2 (0.04)	0.12 (0.02)	
Pers-cold49	032738.23+301358.6	238 (7)	0.87 (0.02)	0.34 (0.04)	Bolo 21
Pers-cold50	032912.94+311814.3	239 (10)	1.1 (0.04)	0.77 (0.08)	Bolo 49
Pers-cold51	032908.12+312157.8	254 (18)	10.0 (0.58)	1.62 (0.16)	Bolo 47
Pers-cold52	032834.53+310705.5	263 (11)	0.07 (0.01)	0.24 (0.04)	Bolo 28
Pers-cold53	032839.72+311731.9	278 (11)	0.16 (0.01)	0.49 (0.05)	Bolo 31
Pers-cold54	034741.56+325144.0	287 (10)	4.7 (0.13)	1.67 (0.08)	Bolo 122
Pers-cold55	034443.33+320131.5	302 (43)	1.9 (0.27)	0.32 (0.03)	Bolo 116
Pers-cold56	032901.46+312022.8	304 (23)	6.2 (0.39)	1.87 (0.19)	Bolo 42
Pers-cold57	034705.42+324308.5	312 (11)	0.54 (0.02)	0.14 (0.02)	
Pers-cold58	032903.33+312314.6	313 (15)	0.09 (0.01)	0.11 (0.02)	
Pers-cold59	032858.44+312217.5	322 (14)	0.63 (0.02)	0.71 (0.07)	Bolo 40
Pers-cold60	032835.04+302009.8	341 (18)	0.04 (0.01)	0.14 (0.02)	Bolo 27
Pers-cold61	032909.09+312128.7	354 (19)	0.34 (0.02)	0.74 (0.07)	Bolo 47
Pers-cold62	032920.07+312407.5	363 (16)	0.28 (0.01)	0.52 (0.05)	Bolo 54
Pers-cold63	034421.33+315932.5	371 (14)	0.24 (0.01)	0.17 (0.02)	Bolo 113
Pers-cold64	034412.98+320135.4	378 (14)	1.8 (0.06)	0.12 (0.02)	
Pers-cold65	032843.28+311732.9	436 (27)	1.9 (0.11)	0.25 (0.02)	Bolo 31
Pers-cold66	033312.85+312124.2	438 (16)	3.2 (0.1)	0.53 (0.07)	Bolo 76
Pers-cold67	032856.31+312227.8	440 (18)	0.16 (0.01)	0.25 (0.02)	
Pers-cold68	034345.15+320358.6	542 (19)	0.69 (0.02)	0.24 (0.02)	

[1]The envelope mass is calculated assuming a dust temperature $T_D = 15$ K

[2]Bolocam IDs are from chapter 2-4, and indicate that the protostellar source is within 1.0 core FWHM of a given Bolocam core. If no ID is listed, the source was not originally identified as a distinct 1.1 mm core, but there is detectable ($\gtrsim 3\sigma$) 1.1 mm emission at the position of the source (i.e., it has been "band-filled" at 1.1 mm).

Note. — Uncertianties for T_{bol}, L_{bol}, and M_{env} are given in parentheses; uncertainties for T_{bol} and L_{bol} are formal fitting errors from the midpoint SED integration, and do not include systematic uncertainties of 20-30%. Uncertainties in M_{env} are from the photometry only. Absolute uncertainties in the mass may be a factor of 4 or more, from uncertainties in d, κ_{1mm} and T_D, but relative values should be much more accurate.

Table 6.3. Bolometric temperatures, luminosities, and envelope masses of cold protostars in Serpens

ID	c2d name/position (SSTc2dJ...)	T_{bol} (K)	L_{bol} ($L_\odot$)	M_{env} ($M_\odot$)	Bolocam ID
		Class 0			
Serp-cold1	182855.92+002944.7	32 (12)	1.6 (0.47)	1.19 (0.12)	Bolo 8
Serp-cold2	182908.52+003130.5	36 (14)	1.4 (0.38)	1.16 (0.01)	Bolo 15
Serp-cold3	182854.84+002952.5	40 (12)	4.3 (1.1)	1.54 (0.15)	Bolo 8
Serp-cold4	182952.44+003611.7	42 (1)	1.0 (0.01)	0.54 (0.01)	Bolo 24
Serp-cold5	182854.12+002929.9	47 (12)	4.5 (1.)	1.67 (0.17)	Bolo 8
Serp-cold6	183000.72+011301.4	54 (1)	1.2 (0.01)	2.56 (0.01)	Bolo 28
Serp-cold7	182949.20+011654.7	55 (4)	0.58 (0.02)	2.42 (0.24)	Bolo 22
Serp-cold8	182854.84+001832.6	56 (16)	0.16 (0.04)	0.24 (0.02)	Bolo 7
Serp-cold9	182949.56+011521.9	57 (27)	11.0 (3.7)	7.98 (0.01)	Bolo 23
Serp-cold10	182948.12+011644.9	58 (1)	2.1 (0.02)	3.72 (0.37)	Bolo 22
Serp-cold11	182959.28+011401.7	59 (1)	1.7 (0.01)	2.56 (0.01)	Bolo 26
		Class I			
Serp-cold12	182906.72+003034.3	77 (1)	1.9 (0.01)	1.39 (0.14)	Bolo 14
Serp-cold13	182948.84+011617.7	79 (1)	7.6 (0.01)	1.53 (0.15)	Bolo 22
Serp-cold14	182952.08+011547.8	85 (1)	2.6 (0.02)	1.23 (0.12)	Bolo 23
Serp-cold15	182902.04+003120.6	86 (1)	0.05 (0.01)	0.17 (0.02)	
Serp-cold16	182902.76+003009.5	95 (30)	1.0 (0.32)	0.22 (0.02)	Bolo 13
Serp-cold17	183005.40+004104.5	100 (1)	0.08 (0.01)	0.19 (0.02)	
Serp-cold18	182954.24+003601.3	101 (35)	0.17 (0.05)	0.48 (0.05)	Bolo 24
Serp-cold19	182844.76+005125.7	110 (6)	0.04 (0.01)	0.24 (0.02)	Bolo 3
Serp-cold20	182906.36+003043.2	117 (1)	1.5 (0.01)	1.38 (0.14)	Bolo 14
Serp-cold21	182952.80+011456.0	120 (1)	1.2 (0.01)	0.74 (0.07)	Bolo 23
Serp-cold22	183000.00+011311.6	129 (1)	2.0 (0.01)	2.56 (0.01)	Bolo 28
Serp-cold23	182951.00+011640.6	141 (1)	1.7 (0.01)	1.84 (0.18)	Bolo 22
Serp-cold24	182957.48+011300.4	157 (36)	2.6 (0.58)	2.35 (0.24)	Bolo 25
Serp-cold25	182957.84+011251.4	190 (40)	3.1 (0.63)	1.06 (0.11)	Bolo 25
Serp-cold26	182845.12+005203.5	204 (2)	0.24 (0.01)	0.29 (0.03)	Bolo 3
Serp-cold27	183000.00+011159.0	249 (36)	1.8 (0.25)	1.14 (0.11)	Bolo 29
Serp-cold28	182851.24+001927.3	250 (3)	0.06 (0.01)	0.16 (0.02)	Bolo 7
Serp-cold29	182949.56+011706.0	294 (9)	0.58 (0.02)	1.87 (0.19)	Bolo 22
Serp-cold30	182958.92+011426.2	303 (9)	0.62 (0.02)	2.0 (0.2)	Bolo 26
Serp-cold31	182956.76+011446.5	322 (1)	5.8 (0.02)	0.69 (0.07)	
Serp-cold32	182844.04+005337.9	360 (5)	0.19 (0.01)	0.26 (0.03)	Bolo 2
Serp-cold33	183002.88+011228.2	374 (2)	2.2 (0.01)	1.32 (0.13)	Bolo 28
Serp-cold34	182957.48+011404.5	426 (1)	19.0 (0.02)	1.9 (0.19)	Bolo 26

Table 6.3 (cont'd)

ID	c2d name/position (SSTc2dJ...)	T_{bol} (K)	L_{bol} ($L_\odot$)	M_{env} ($M_\odot$)	Bolocam ID
Serp-cold35	182931.92+011842.9	430 (1)	5.3 (0.01)	2.12 (0.01)	Bolo 20
Serp-cold36	183005.76+003930.8	431 (6)	0.05 (0.01)	0.2 (0.02)	Bolo 32
Serp-cold37	182916.08+001822.7	437 (1)	1.7 (0.01)	0.54 (0.01)	Bolo 17

Note. — Columns are as in table 6.3, and uncertainties for T_{bol}, L_{bol}, and M_{env} are given in parentheses.

6.6.4 Individual Sources

Here we briefly discuss a few examples of interesting or newly-identified cold protostellar sources.

6.6.4.1 IRAS 03292+3039

IRAS 03292+3039 (Pers-Cold 2) is a little-studied, Class 0 source associated with the 1.1 mm core Pers-Bolo 66, and was discussed briefly in chapter 2. An image of IRAS 03292+3039, together with the SED, is shown in figure 6.2. Jørgensen et al. (2006) identified this as an outflow source, noting on the large-scale outflow visible in the 4.5 μm IRAC band (also seen in figure 6.2 as bright 8 μm knots on either side of the protostellar source).

Bright 1.1 mm emission centered on this object indicates a fairly massive protostellar envelope (2.8 $M_\odot$), while the powerful outflow and low bolometric temperature ($T_{bol} = 25$ K) are evidence of an extremely young, energetic embedded protostar. The spectral energy distribution (figure 6.2) is similar to well-known Class 0 protostars in Perseus such as NGC 1333-IRAS 4, and the nearby source IRAS 03282+3035. The small fan-shaped nebulosity visible at 3.6 and 4.5 μm (figure 6.19) is most easily explained by a cone-shaped cavity, carved out of the dense envelope by an energetic outflow. The orientation of the nebulosity corresponds well to the larger-scale outflow traced by IRAC emission, and the approximate orientation of the large-scale outflow is indicated by thick gray lines in figure 6.19. The one-sided nebulosity at 3.6 μm is strikingly similar to the Whitney et al. (2003) model IRAC image of an early Class 0

Table 6.4. Bolometric temperatures, luminosities, and envelope masses of cold protostars in Ophiuchus

ID	c2d name/position (SSTc2dJ...)	T_{bol} (K)	L_{bol} ($L_\odot$)	M_{env} ($M_\odot$)	Bolocam ID
		Class 0			
Oph-cold1	162821.72–243623.4	36 (2)	0.25 (0.01)	0.17 (0.02)	Bolo 26
Oph-cold2	163222.56–242831.8	54 (5)	6.9 (0.48)	0.12 (0.02)	Bolo 37
Oph-cold3	162625.80–242428.8	57 (28)	0.41 (0.15)	0.24 (0.02)	Bolo 9
		Class I			
Oph-cold4	163136.84–240419.7	77 (2)	0.18 (0.01)	0.03 (0.01)	
Oph-cold5	162718.36–242836.7	82 (14)	0.01 (0.01)	0.08 (0.01)	
Oph-cold6	162721.96–242727.5	87 (33)	0.08 (0.03)	0.12 (0.01)	Bolo 17
Oph-cold7	162715.84–243845.1	89 (35)	0.4 (0.13)	0.02 (0.01)	
Oph-cold8	162705.40–243629.5	106 (8)	0.15 (0.01)	0.09 (0.01)	Bolo 14
Oph-cold9	163151.96–245726.0	124 (12)	0.01 (0.01)	0.05 (0.01)	Bolo 33
Oph-cold10	162625.44–242301.3	135 (9)	0.1 (0.01)	0.53 (0.05)	Bolo 8
Oph-cold11	163200.96–245642.5	145 (14)	2.7 (0.2)	0.05 (0.01)	Bolo 35
Oph-cold12	162659.28–243458.6	177 (43)	2.0 (0.45)	0.21 (0.02)	Bolo 12
Oph-cold13	162717.64–242856.2	190 (11)	0.52 (0.03)	0.07 (0.01)	
Oph-cold14	162724.48–244103.0	191 (37)	0.33 (0.06)	0.12 (0.01)	Bolo 18
Oph-cold15	163152.32–245536.1	240 (13)	0.13 (0.01)	0.08 (0.01)	
Oph-cold16	162621.48–242305.4	254 (20)	4.4 (0.29)	0.22 (0.02)	Bolo 5
Oph-cold17	162727.00–244050.6	255 (34)	2.2 (0.25)	0.36 (0.04)	Bolo 18
Oph-cold18	162728.08–243932.5	264 (43)	2.7 (0.39)	0.11 (0.01)	
Oph-cold19	163135.76–240129.3	290 (8)	1.5 (0.03)	0.09 (0.01)	Bolo 30
Oph-cold20	162857.72–244054.8	304 (14)	0.03 (0.01)	0.04 (0.01)	
Oph-cold21	162728.44–242720.9	309 (14)	0.47 (0.02)	0.29 (0.03)	Bolo 20
Oph-cold22	162706.84–243814.8	310 (13)	0.6 (0.02)	0.05 (0.01)	Bolo 13
Oph-cold23	162640.56–242714.3	372 (17)	0.06 (0.01)	0.06 (0.01)	
Oph-cold24	162709.36–243718.6	383 (70)	4.8 (0.61)	0.07 (0.01)	Bolo 14
Oph-cold25	162702.16–243729.8	400 (45)	3.7 (0.39)	0.09 (0.01)	
Oph-cold26	162648.48–242838.6	428 (19)	0.12 (0.01)	0.03 (0.01)	
Oph-cold27	162737.08–244237.8	438 (16)	0.13 (0.01)	0.04 (0.01)	
Oph-cold28	163143.68–245524.6	496 (16)	0.28 (0.01)	0.04 (0.01)	
Oph-cold29	162730.24–242743.2	528 (16)	0.93 (0.02)	0.19 (0.02)	Bolo 20
Oph-cold30	162739.96–244314.9	551 (18)	0.74 (0.02)	0.04 (0.01)	
Oph-cold31	162721.60–244142.9	595 (17)	1.2 (0.03)	0.04 (0.01)	
Oph-cold32	162623.64–242439.4	609 (21)	0.3 (0.01)	0.03 (0.01)	

Note. — Columns are as in table 6.3, and uncertainties for T_{bol}, L_{bol}, and M_{env} are given in parentheses.

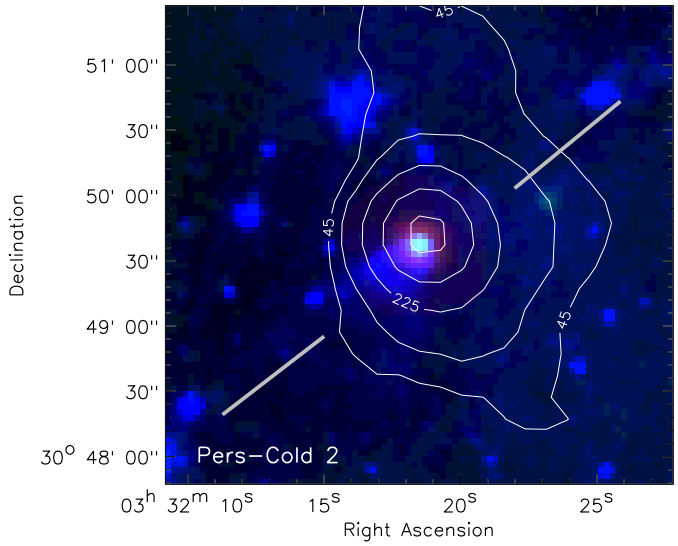

Figure 6.19 three-color *Spitzer* image (3.6, 24, 70 μm) of IRAS 03292+3039 (Pers-Cold 2), with 1.1 mm contours, showing the fan-shaped nebulosity that is visible at 3.6 μm. The nebulosity is most likely scattered light from a narrow outflow cavity in this deeply embedded Class 0 source. Thick gray lines indicate the approximate orientation of the larger-scale outflow (Jørgensen et al., 2006).

sources viewed at an inclination angle of 30 deg (their figure 12a).

6.6.4.2 Pers-Bolo 102

Pers-Bolo 102 is bright 1.1 mm source that was identified in Bolocam survey of Perseus (Enoch et al. 2006; chapter 2); it lies within the region of active star-formation near IC 348, which includes the famous outflow driving source HH 211 (McCaughrean et al., 1994). The *Spitzer* 24 μm image resolves the luminous internal source into a double object (Pers-Cold 17 and Pers-Cold 30). Although they have very similar SEDs for $\lambda \geq 8$ μm (figure 6.20), variations at shorter wavelengths cause Pers-Cold 17 ($T_{bol} = 56$ K) to fall into Class 0, while Pers-Cold 30 ($T_{bol} = 72$ K) falls just outside the Class 0/Class I boundary at $T_{bol} = 70$ K. These sources are good examples of why a more continuous evolutionary scheme is preferable to the standard classifications. Recently obtained CARMA interferometric observations at $\lambda = 2.7$ mm resolve the millimeter core into two sources, coincident with the *Spitzer* source positions (Enoch

et al., in preparation). The 2.7 mm flux ratio of the northern (Pers-Cold 17) to southern (Pers-Cold 30) source is at least 2:1, further evidence that Pers-Cold 30 is slightly more evolved.

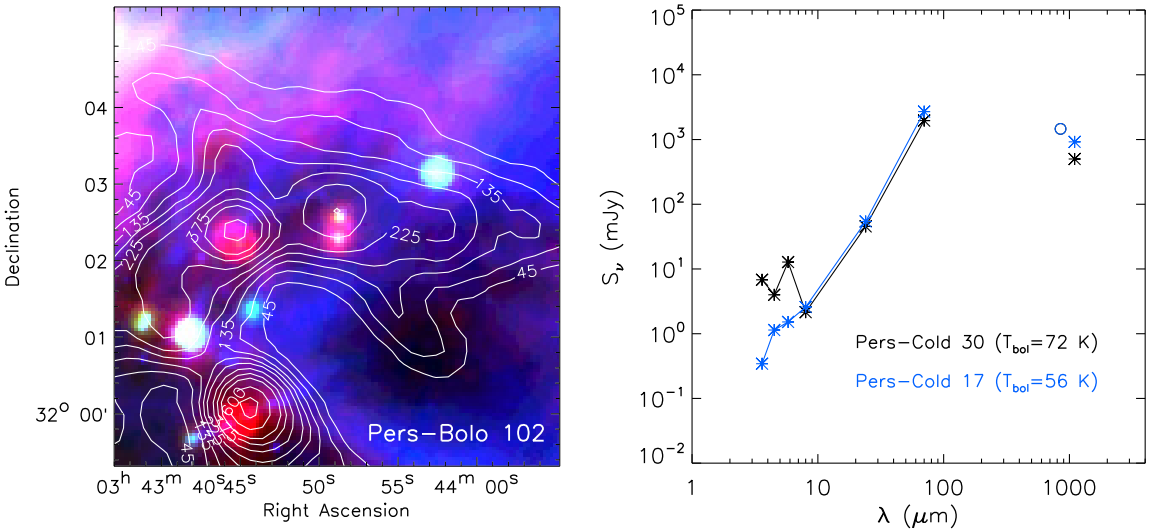

Figure 6.20 three-color *Spitzer* image (8, 24, 70 μm) of Pers-Bolo 102, a new candidate binary Class 0/I source, with 1.1 mm contours. SEDs of the two cold protostellar sources associated with the single 1.1 mm core are shown in the right panel. Although the SEDs look very similar at $\lambda \geq 8$ μm, the southern source is brighter at shorter wavelengths, and has a slightly higher bolometric temperature ($T_{bol} = 72$ K versus $T_{bol} = 56$ K).

Although not as massive or cold as nearby HH 211 (Pers-Cold 1) and IC 348-mm (Pers-Cold 10), Pers-Bolo 102 is an interesting case study. It appears to be a separate-envelope binary system, with two late Class 0 or early Class I sources that are likely coeval. The separation of the sources is 17″, or 4200 AU. Binary separations of this order are consistent with early fragmentation in a relatively dense cloud ("prompt initial fragmentation", e.g., Pringle 1989; Looney et al. 2000), and the individual sources would most likely have distinct protostellar envelopes. If the binary formed via gravitational fragmentation, we would expect the separation to correspond to the local Jeans length:

$$\lambda_J = \left(\frac{\pi c_s^2}{G \mu_p m_H n} \right)^{1/2}, \tag{6.5}$$

where c_s is the local sound speed, and $\mu_p = 2.33$ and n are the mean molecular weight and mean density per particle, respectively (Jeans, 1928). A Jeans length of 4200 AU would require a relatively high density of $n \sim 6 \times 10^5$ cm^{-3} (assuming $c_s = 0.2$ km s^{-1}). The mean density of the Pers-Bolo 102 core, measured at the FWHM contour, is a factor of four lower than this required value, or 1.4×10^5 cm^{-3}. The *peak* density measured within the beam size of 30″, which corresponds to a linear size of approximately 4000 AU at the distance of Perseus, is considerably higher, however, 16×10^5 cm^{-3}.

6.6.4.3 Serp-Bolo 33 and Other Class II Objects

Given our sensitivity limit at 1.1 mm of approximately 0.1 M$_\odot$, almost all sources detected at 1.1 mm will be dense cores or envelopes around relatively young protostars. In general, by the time a protostar has consumed or dispersed its massive envelope and enters the Class II (T Tauri) stage (e.g., Adams et al., 1987), the remnant disk of gas and dust has too little mass to be detected by our surveys. Typical measured masses of Class II disks are $0.01 - 0.1$ M$_\odot$ (e.g., Beckwith & Sargent 1996), although values as large as 1 M$_\odot$ have been measured (Beckwith et al., 1990).

In a few a cases, however, we do detect 1.1 mm emission around sources with Class II-type SEDs. These objects have bolometric temperatures $T_{bol} > 650$ K, which defines the Class I/Class II boundary, and a flux density at 1.1 mm that is lower than the flux densities from 3.6 to 24 μm. With the exception of two "flat spectrum" objects ($-0.3 < \alpha_{IR} < 0.3$; Greene et al. 1994), the near- to mid-infrared spectral index α_{IR} is in the range -0.34 to -1.04, confirming their Class II status. In some cases, the 1.1 mm emission is unresolved, consistent with a compact disk. Often, however, these Class II sources are in a region of confused millimeter emission; therefore the physical association of such objects with the 1.1 mm emission is not secure. Table 6.5 lists all of the sources with $T_{bol} > 650$ K (Class II) in each cloud that are detected in our 1.1 mm surveys. Most of the sources lie in confused regions of 1.1 mm emission, indicated by a "*" in the "Bolocam ID" column. The remaining objects have point-like 1.1 mm emission centered on the *Spitzer* position.

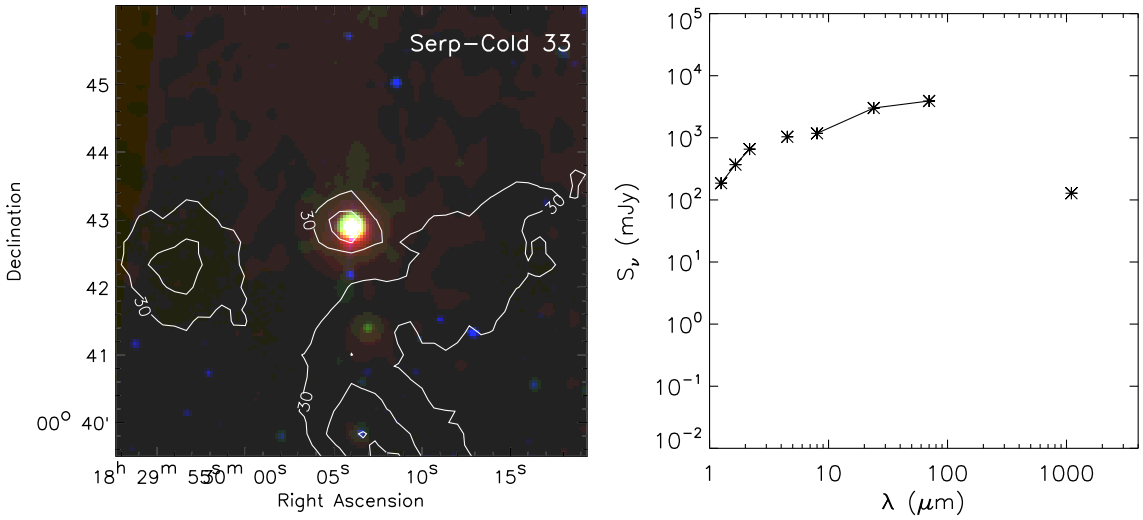

Figure 6.21 three-color *Spitzer* image $(8, 24, 70\ \mu\mathrm{m})$ of Serp-Cold 33, a bright Class II-type object with compact 1.1 mm emission. Contours of 1.1 mm emission at $(3, 6, 9..)\sigma$ are overlaid. The SED of Serp-Cold 33 is shown in the right panel; although this is clearly an evolved source, we are able to detect 1.1 mm emission, likely from a compact disk, due to the brightness of the source.

One noteworthy example is Serp-Bolo 33 in Serpens, a very bright *Spitzer* source with $L_{bol} = 3.6\ \mathrm{L}_\odot$, $T_{bol} = 871$ K, and compact 1.1 mm emission centered on the *Spitzer* position. It is also classified as Class II based on the spectral index $\alpha_{IR} = -0.42$. Vieira et al. (2003) included this source in a sample of Herbig Ae/Be candidates, believed to be the intermediate mass Class II counterparts of low-mass T Tauri objects, although the spectral type is F3. The 1.1 mm mass calculated assuming an optically thin disk is 0.17 $\mathrm{M}_\odot$, approximately 10% of the estimated stellar mass of $M_* \sim 1.3\ \mathrm{M}_\odot$, based on the measured effective temperature $T_{eff} \sim 6300$ K (Vieira et al., 2003) and an empirical $T_{eff} - M$ relation (Habets & Heintze, 1981).

Table 6.5. Class II sources detected at 1.1 mm in Perseus, Serpens, and Ophiuchus

c2d name/position (SSTc2dJ...)	T_{bol} (K)	L_{bol} ($L_\odot$)	M_{1mm}[1] ($M_\odot$)	Bolocam ID[2]	other names
		Perseus			
032747.66+301204.5	662 (15)	2.80 (0.05)	0.82 (0.06)	Pers-Bolo 24	RNO 15[3](1)
034400.00+320154.1	700 (17)	1.60 (0.03)	0.40 (0.04)	Pers-Bolo 106*	
032900.00+312146.6	856 (26)	0.33 (0.01)	0.90 (0.09)	Pers-Bolo 40*	LkHα 353 (2)
034109.13+314437.8	873 (30)	1.70 (0.06)	0.16 (0.02)	Pers-Bolo 90	IRAS 03380+3135
032856.64+311835.5	993 (22)	0.42 (0.01)	0.10 (0.02)	Pers-Bolo 39*	ASR 120 (3)
034548.27+322412.0	1096 (23)	5.00 (0.09)	0.10 (0.02)	Pers-Bolo 120	LkHα 330 (2)
032917.66+312245.0	1297 (22)	1.50 (0.02)	0.19 (0.02)	Pers-Bolo 54*	LkHα 270 (2)
		Serpens			
182900.00+003003.1	806 (5)	0.19 (0.01)	0.35 (0.03)	Serp-Bolo 13*	
183006.12+004233.8	871 (2)	3.60 (0.01)	0.17 (0.01)	Serp-Bolo 33	
182900.96+002931.6	892 (2)	1.20 (0.01)	0.23 (0.02)	Serp-Bolo 13*	
182901.32+002933.0	892 (6)	0.36 (0.01)	0.23 (0.02)	Serp-Bolo 13*	
182901.68+002954.6	1158 (3)	1.80 (0.01)	0.23 (0.02)	Serp-Bolo 13*	CoKu Ser G3 (4)
182901.68+002946.5	1212 (5)	0.70 (0.01)	0.25 (0.02)	Serp-Bolo 13*	CoKu Ser G4 (4)
		Ophiuchus			
163151.96-245615.7	690 (18)	1.20 (0.03)	0.05 (0.01)	*	
162610.32-242054.6	773 (20)	0.36 (0.01)	0.39 (0.03)	Oph-Bolo 4*	
162623.28-242100.8	1082 (28)	2.00 (0.04)	0.15 (0.01)	Oph-Bolo 7*	

[1]The 1.1 mm mass (M_{1mm}) is calculated for an optically thin disk and a dust temperature of T_D = 15 K. Our assumption for the dust opacity may be incorrect for typical Class II disks, however, where grain growth is a possibility (e.g., Natta et al., 2007).

[2]Bolocam IDs with "*"s indicate that the source is in a confused region at 1.1 mm, and the association of the Spitzer object with the given 1.1 mm emission is not secure.

[3]Typically classified as a Class I source, RNO 15 has a bolometric temperature just above the Class I cutoff in our sample. The spectral index of RNO 15 is $\alpha_{IR} = -0.09$, placing it in the "flat spectrum" category, or close to the Class I boundary.

Note. — References: (2) Herbig & Kameswara 1972; (3) Aspin et al. 1994; (4) Cohen & Kuhi 1979.

6.7 Comparison of Classification Methods

Identifying the evolutionary states of sources in our sample is a necessary first step for studying the early evolution of protostars. The evolutionary status is typically estimated by classifying sources into groups based on SED characteristics. A number of different classification methods are employed in the literature; most often used are the near- to mid-infrared spectral index α_{IR} ($\alpha_{IR} = d\log(\lambda F_\lambda)/d\log(\lambda)$; Lada 1987), the bolometric temperature T_{bol} (Myers & Ladd 1993, see §6.6.1), and the ratio of submillimeter to bolometric luminosity L_{submm}/L_{bol} (André et al., 1993). Generally, L_{submm} is taken to be the integrated luminosity at wavelengths $\lambda > 350$ μm. We typically have only one flux measurement for $\lambda > 160$ μm, and a number of sources lack information even at 160 μm, so an accurate determination of L_{submm} is not possible with these data. We will focus, therefore, on T_{bol} and the spectral index α_{IR}.

In figure 6.22 we compare classifications based on α_{IR} and T_{bol} for the cold protostar samples in Perseus, Serpens, and Ophiuchus. Thick colored symbols indicate sources associated with 1.1 mm emission, and thin black points represent sources with upper limits at 1.1 mm. The spectral index α_{IR} is determined from a least squares fit to the SED from the shortest available wavelength (usually 2MASS 1.25 μm or IRAC 3.6 μm) to $\lambda = 24$ μm (Evans et al., 2007). The calculation of T_{bol} is described in §6.11. We adopt class divisions for T_{bol} from Chen et al. (1995): $T_{bol} < 70$ K (Class 0), $70 < T_{bol} < 650$ K (Class I), and $T_{bol} > 650$ K (Class II), and divisions for α_{IR} from (André & Montmerle, 1994): $\alpha_{IR} < 0$ (Class I) and $\alpha_{IR} > 0$ (Class II). No well-defined α_{IR} criteria exists for Class 0 sources; such deeply embedded objects were general not visible in the mid-IR prior to *Spitzer*, making the calculation of α_{IR} impossible until recently.

The two classification methods agree fairly well for Class II and "warmer" Class I sources. Very cold ($T_{bol} \lesssim 100$ K) sources, however, have a wide range of α_{IR} values, a few even falling into Class II based on the spectral index. At least part of the reason for this large scatter in α_{IR} values becomes apparent when examining the SEDs of some deeply embedded sources, which can have widely varying shapes at short wavelengths.

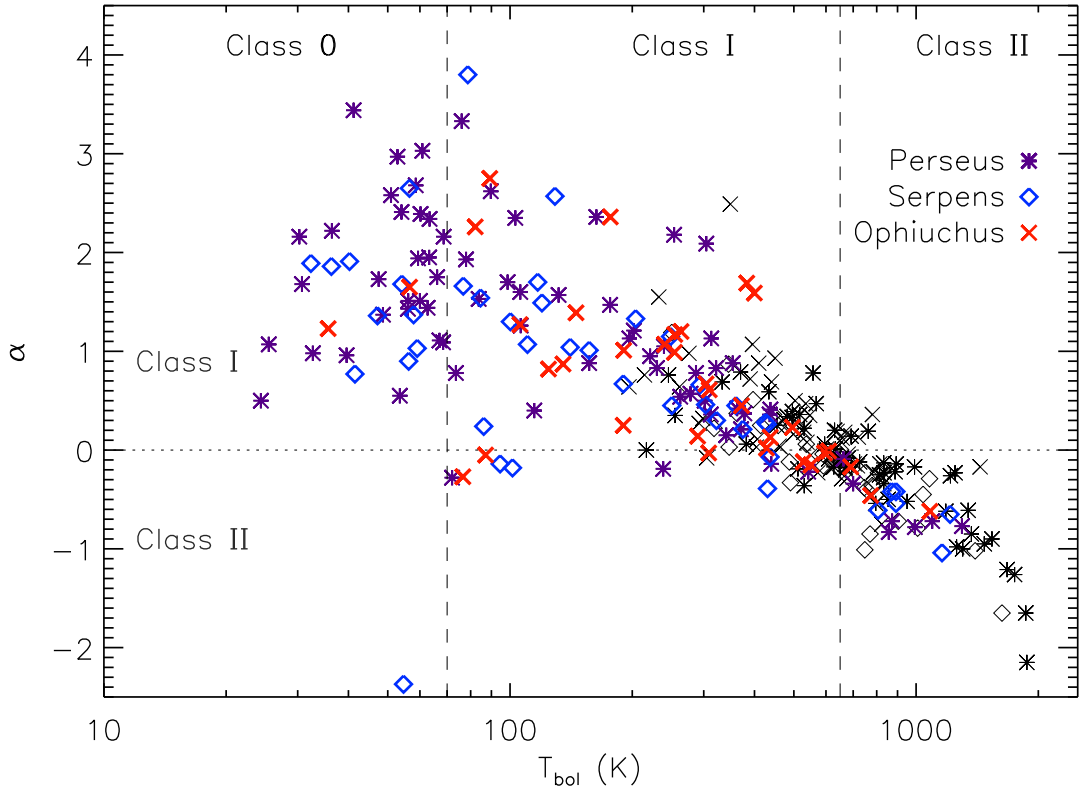

Figure 6.22 Bolometric temperature versus near- to mid-IR spectral index (α_{IR}), for the cold protostar samples in Perseus, Serpens, and Ophiuchus. Thick colored symbols indicate sources associated with 1.1 mm emission, and thin black points represent those with upper limits at 1.1 mm. Standard class divisions for both T_{bol} and α_{IR} are shown. The two methods agree fairly well for Class II and "warmer" Class I sources, but very cold ($T_{bol} \lesssim 100$ K) sources have a large range of α_{IR} values.

Many protostellar SEDS are not monotonically increasing from 3.6 to 24 μm, many falling from 5.8 to 8 μm, and rising again at longer wavelengths, e.g., Pers-Cold 2, Pers-Cold 19, Pers-Cold 24 (figure 6.2), Oph-Cold 1 (figure 6.4). The most likely cause of these features are geometric effects such as scattered light from an outflow cavity, or dust and ice absorption features originating in the protostellar envelope. In any case, non-monotonic behavior at short wavelengths will clearly confuse the calculated slope α_{IR}. Even using α_{IR} calculated from a straight line fit to the two end-point wavelengths, however, still results in a large range of α_{IR} values at low T_{bol}.

For further information about whether α_{IR} or T_{bol} is a more accurate characteriza-

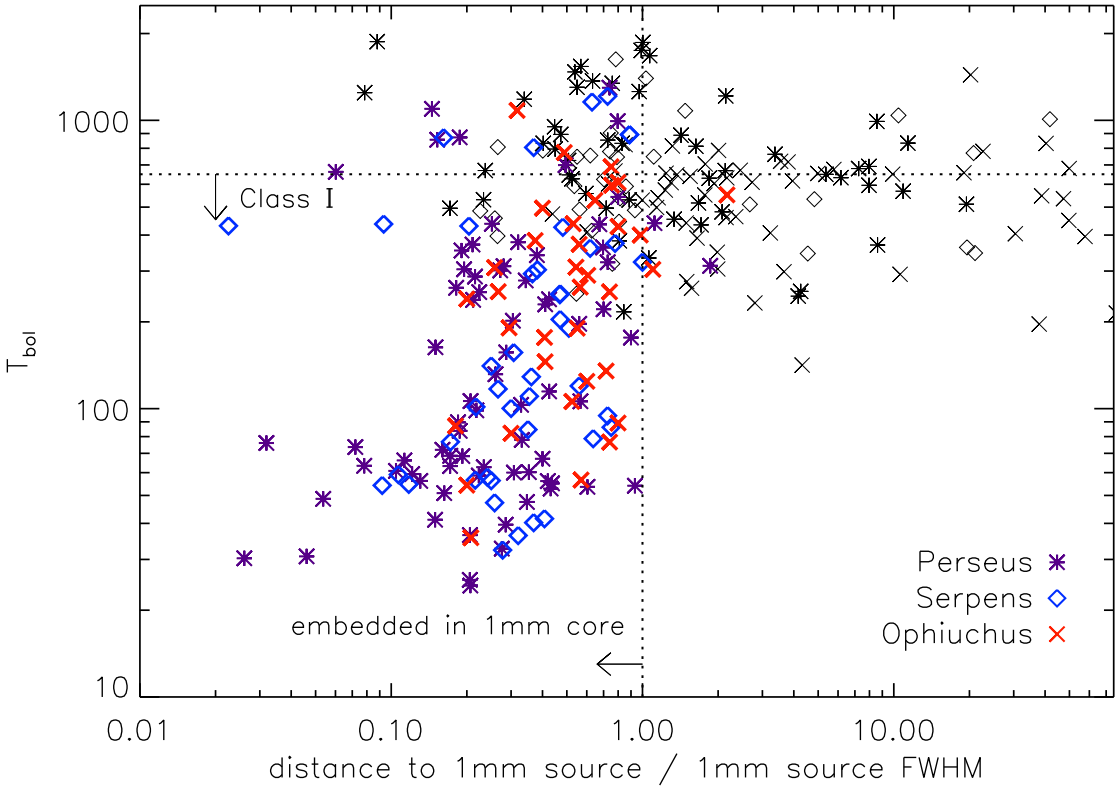

Figure 6.23 Distribution of bolometric temperature as a function of distance to the nearest 1.1 mm core for cold protostar candidates in all three clouds. Distances are in units of the 1.1 mm core FWHM size, and symbols are as in figure 6.22. Sources within 1.0 FWHM of a 1.1 mm core position are considered embedded within that core. There is a clear correlation between smaller distances, or more embedded sources, and lower T_{bol} values.

tion of the true evolutionary state, we look at the correlation between both measures and millimeter cores. Figure 6.23 shows the distribution of T_{bol} with respect to the distance to the nearest 1.1 mm core, in units of the core FWHM size. In all three clouds, essentially all sources with $T_{bol} \lesssim 200$ K lie within one core FWHM of a 1.1 mm peak, and are likely associated with a millimeter core. Thus the majority of "cold" objects, as defined by low T_{bol}, appear to be embedded in dense envelopes, and likely at an early evolutionary stage. Furthermore, there is a clear correlation between smaller distance and lower T_{bol}, suggesting that sources with lower T_{bol} are more embedded than those with higher T_{bol}. If we affiliate the degree of embeddedness

with youth, then T_{bol} seems to correlate well with evolutionary state.

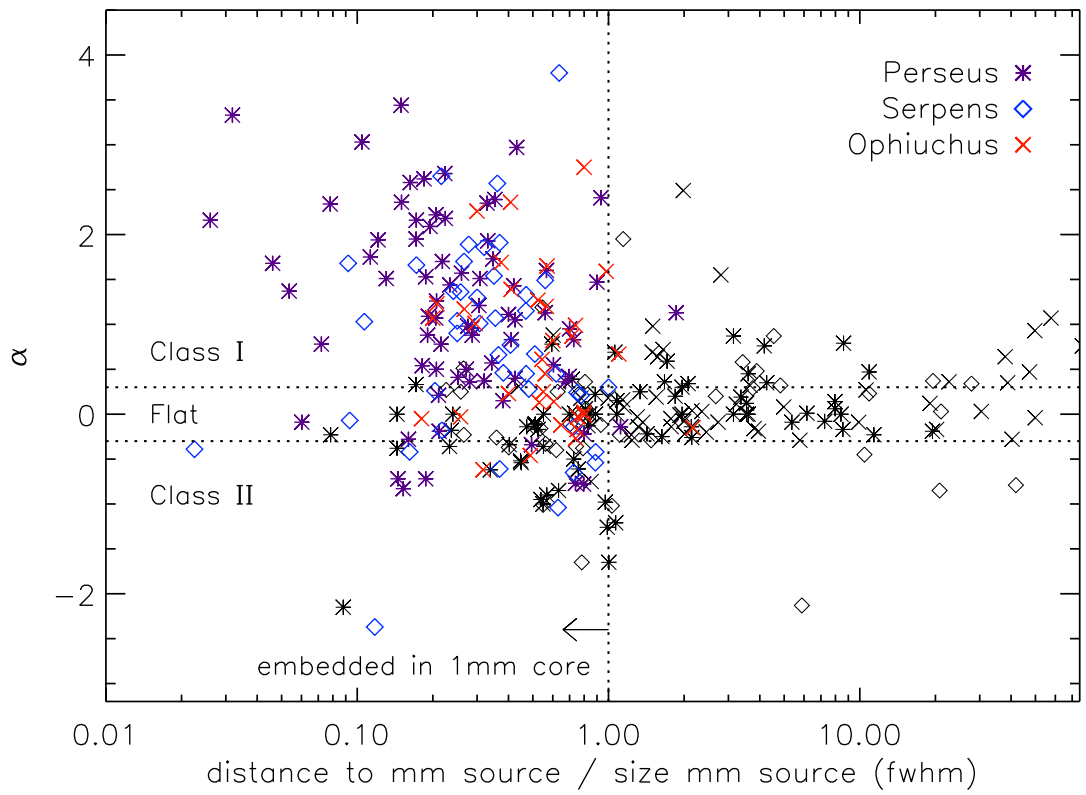

Figure 6.24 Distribution of the near- to mid-infrared spectral index α_{IR} as a function of distance to the nearest 1.1 mm core, for cold protostar candidates in all three clouds. Distances are in units of the nearest 1.1 mm core FWHM size, and symbols are as in figure 6.22. While there is some correlation between higher α_{IR} values and smaller distances, it is not as compelling as that observed for T_{bol} in figure 6.23.

A similar plot for α_{IR} with respect to the distance to the nearest 1.1 mm core is shown in figure 6.24. While there is some correlation between higher α_{IR} values and smaller distances, the relationship is not nearly as clear as it is for T_{bol} (figure 6.23). In particular, there are a number of sources with large α_{IR} values for which the distance to the nearest core is much larger than one FWHM. Likewise, there are several deeply embedded sources with low α_{IR} values.

Based on figures 6.22–6.24, and on an examination of sources with $T_{bol} < 70$ K objects, a number of which are known Class 0 sources, we conclude that T_{bol} is more reliable than α_{IR} for classifying the most embedded protostars. Hereafter, T_{bol} will

be used to characterize protostellar sources, and we use the divisions from Chen et al. (1995) noted above to place sources into Class 0, Class I, or Class II. Recall that we also require Class I sources to be detected at 1.1 mm in addition to the T_{bol} criteria This is clearly a reasonable requirement, as our physical definition of Class I sources ($M_{env} > M_*$) dictates that they should be detected at millimeter wavelengths. The point-source sensitivity of the Bolocam 1.1 mm surveys limit our completeness to Class I sources with $M_{env} \gtrsim 0.09$ $M_\odot$ in Perseus, $M_{env} \gtrsim 0.07$ $M_\odot$ in Serpens, and $M_{env} \gtrsim 0.04$ $M_\odot$ in Ophiuchus.

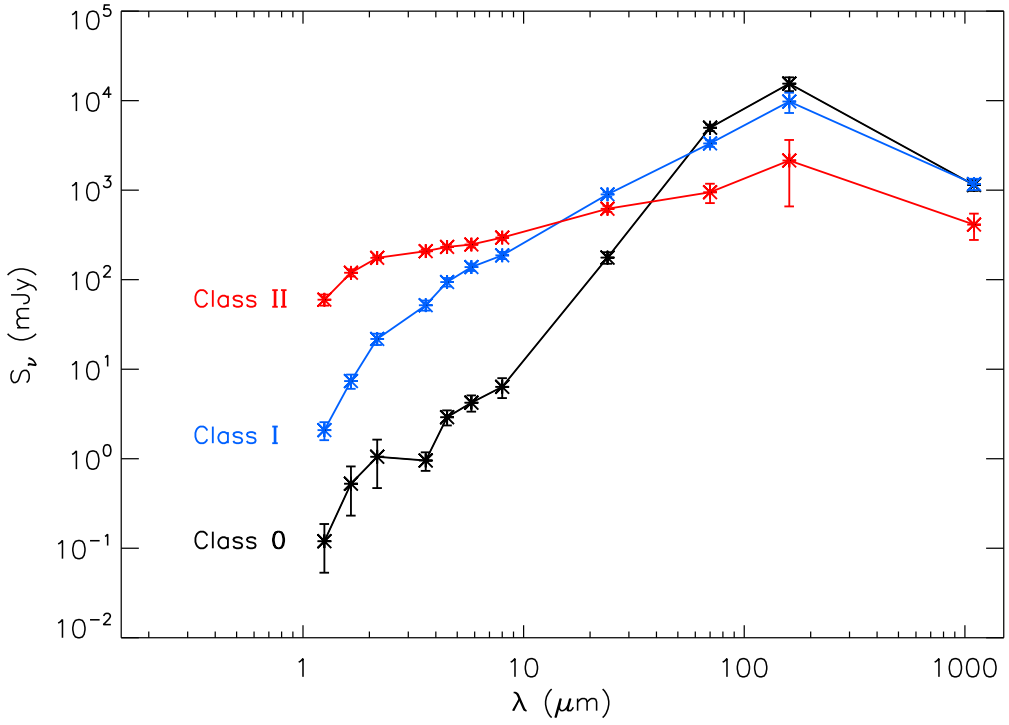

Figure 6.25 Average spectra for Class 0, Class I, and Class II sources, calculated using the SEDs of sources from Perseus and Serpens. Individual SEDs are weighted by the bolometric luminosity. Classifications are based on the source T_{bol}: $T_{bol} < 70$ K (Class 0), $70 < T_{bol} < 650$ K (Class I), and $T_{bol} > 650$ K (Class II), with the additional requirement that Class I sources be detected at 1.1 mm. Error bars are the 1σ error in mean, and not the sample dispersion, which is much larger. The Class II spectrum may not be representative of all Class II objects, as we are very incomplete to sources without protostellar envelopes.

The average spectra of all Class 0, Class I, and Class II sources, as defined by T_{bol}

and the above criteria, are shown in figure 6.25. Average spectra for each class are calculated using sources from Perseus and Serpens, and individual SEDs are weighted by the bolometric luminosity. Flux density upper limits are ignored. Error bars in figure 6.25 represent the 1σ error in the mean ($\sigma_\lambda/\sqrt{N_\lambda}$), but the dispersion in the sample (σ_λ) is much larger. Source SED shapes do not fall into discrete bins, but form a continuous distribution between the averages shown. Points with large error bars indicate either that a small number of flux points went into the average due to a number of sources with upper limits, or that there are significant differences between sources at that wavelength. We do not include Ophiuchus sources in the average because the lack of 160 μm fluxes for most of the Ophiuchus sample tends to bias T_{bol} to slightly higher values.

Note that the progression from Class 0 to Class I to Class II is as expected if this represents a sequence of physical evolution. In particular, the average Class 0 spectrum has the lowest flux densities from 1.25 to 24 μm, as expected for deeply embedded sources with massive, extincting envelopes, and the highest fluxes at $70 - 1100$ μm, where reprocessed protostellar flux is emitted by the cold envelope. By contrast, the average Class II spectrum is relatively flat, with a much larger percentage of the protostar flux emerging at shorter wavelengths, as expected for older sources that do not have much circumstellar material. Between these two extremes is the average Class I spectrum, although the separation between the Class 0 and Class I spectra, as well as the variety of SED shapes, suggests that a more continuous means of estimating evolutionary status may be more appropriate. Large error bars for $\lambda = 1 - 3$ μm for the average Class 0 spectrum are indicative of the wide range of behavior of Class 0 objects in the near-infrared, and the presence of non-monotonic behavior is apparent at $\lambda = 3.6$ μm. It should be mentioned here that the average Class II spectrum is not necessarily representative of all Class II objects, as we are very incomplete to sources without protostellar envelopes. We only find 20 Class II objects in Serpens, while Harvey et al. (2007a) find 132 Class II sources.

When we include Ophiuchus in the average, the average spectra are shifted, have larger dispersion, and the similarity of SEDs within a bin is reduced. This behavior

seems to indicate that T_{bol} may be overestimated for many sources in Ophiuchus, likely due to the lack of information at 160 μm. To mitigate the biases caused by missing 160 μm points, we use the average spectra from figure 6.25 as templates, and assign each Ophiuchus source to Class 0, Class I, or Class II based on a least squares fit. The results of this analysis are shown for Class 0 and Class I in figure 6.26. The best-fitting average spectrum is determined by minimizing the reduced χ^2, with the free parameter of each fit being the scaling factor between the template and source spectra.

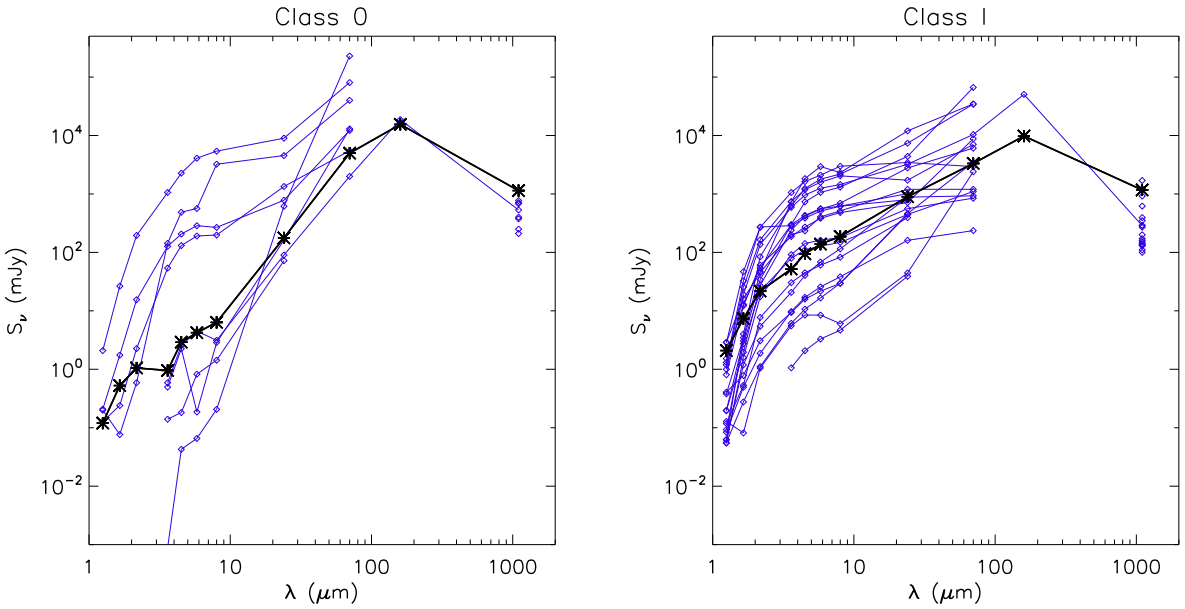

Figure 6.26 Results of using the average spectra from figure 6.25 as templates (thick black lines), to assign Ophiuchus sources (thin blue lines) to Class 0 and Class I. For each source in Ophiuchus, the best-fitting average spectrum (Class 0, Class I or Class III) is determined by a least squares fit, with the scaling factor between the template and source spectra left as a free parameter. An additional 5 sources fall into Class 0 by this method, but the spectra of 4 of those have shapes that may be indicative of high extinction.

In contrast to a simple T_{bol} cut, which results in only three sources designated as Class 0 and 29 as Class I, fitting to the average spectra results in 8 Class 0 and 20 Class I designations in Ophiuchus. Examining the spectra, however, half of those in the Class 0 group look quite different from the template spectrum. Neither do they look like the average Class I spectrum; there is a population of sources in Ophiuchus

with spectra that are steeply rising from 1.25 to 4.5 μm, then relatively flat from 4.5 to 24 μm. A few similar sources are seen in Serpens and Perseus, but not in the same numbers as observed for Ophiuchus. It is possible that the steep rise in the near-infrared for these sources is simply the result of a high degree of extinction. Although the average cloud extinction in Ophiuchus, as measured by the reddening of background stars, is similar to the other clouds, $\langle A_V \rangle \sim 4 - 7$ mag, protostellar 1.1 mm cores do tend to be found at much higher extinctions in Ophiuchus (§6.4.5).

6.7.1 Alternative Classifications

One advantage of the large, complete sample provided by the combined Bolocam and *Spitzer* data is that we can explore alternative classification schemes; ideally, we could define a more continuous evolutionary sequence than the standard classes that were appropriate for the smaller samples previously available. Having well-sampled SEDs, we can use the overall SED shapes, rather than a single parameter, to characterize sources.

With this goal in mind, we first divide the protostellar sources in each cloud into smaller T_{bol} bins than those of the standard Class 0/I/II divisions. Average spectra for Perseus and Serpens, calculated in bins of $T_{bol} < 50$ K ("early Class 0"), $50 < T_{bol} < 100$ K ("late Class 0"), $100 < T_{bol} < 300$ K ("early Class I"), $300 < T_{bol} < 650$ K ("late Class I"), and $T_{bol} > 650$ K (Class II), are shown in figure 6.27. Error bars represent the 1σ error in the mean, and average spectra are calculated as described in the previous section. The largest errors are seen for the shortest wavelengths in the lowest T_{bol} bins, where NIR fluxes vary significantly from source to source, likely dependent on outflow opening angle and viewing geometry. Binning of T_{bol} is based on general agreement of SEDs in a given bin, as determined by eye, and should not be interpreted as suggestive of strict boundaries.

While there are significant similarities between the SEDs within each bin, individual source SEDS fill the continuum between the average spectra, as for figure 6.25. If we were to plot error bars representative of the dispersion in each bin rather than the

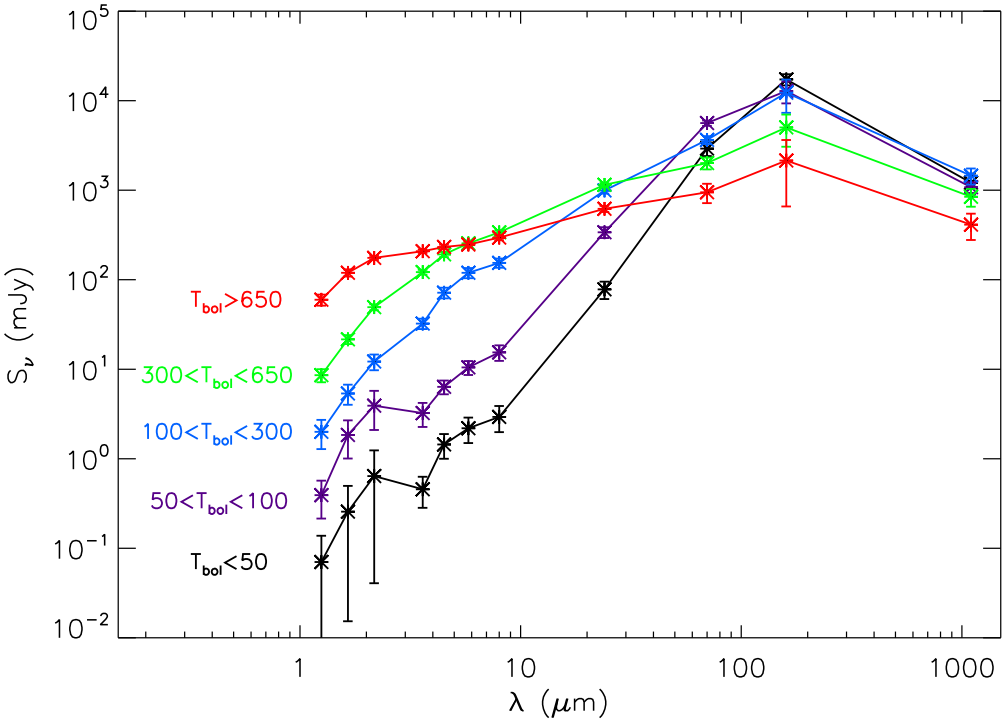

Figure 6.27 Average spectra in designated T_{bol} bins, using sources from Perseus and Serpens, where the average is calculated as described in figure 6.25 and the text. Error bars show the error in the mean. The progression in SED shape for increasing T_{bol} is as expected if this represents physical evolutionary sequence. The large difference at IRAC wavelengths between the "late Class 0" ($50 < T_{bol} < 100$ K) and "early Class I" spectra ($100 < T_{bol} < 300$ K) suggests that this transition occurs fairly rapidly.

error in the mean, each average spectra would be within 1σ of the neighboring T_{bol} bins. The average spectra appear to evolve with T_{bol} as one would expect if T_{bol} is indeed an evolutionary indicator: increasing flux at short wavelengths, and decreasing flux at long wavelengths, with increasing T_{bol}. As discussed above, this kind of spectral evolution might be anticipated if the extincting envelope is continuously accreted or dispersed as the protostar becomes more visible. At all wavelengths except 24 and 70 μm, the flux rises or falls monotonically with increasing T_{bol}. For these intermediate wavelengths, however, the observed flux rises initially as hotter dust close to the protostar is revealed, then falls as the mass of circumstellar material drops. Despite the relatively narrow bins, there is still a rather large change between "late Class 0" ($50 < T_{bol} < 100$ K) and "early Class I" ($100 < T_{bol} < 300$ K), particularly

at $\lambda = 3.6 - 24$ μm, suggesting that this transition occurs fairly rapidly.

We use the average spectra from figure 6.27 as templates to assign cold protostar candidates to one of the five categories defined above ("early Class 0", "late Class 0", etc.). The results are shown in figure 6.28. Source SEDs are color coded by cloud, and template spectra indicated by thick black lines. The number of sources in each category for each cloud is given in the lower right corner. Determination of the best-fitting template spectrum is accomplished as described in §6.7, above. As some SEDs have anomalous points at one wavelength, we redo the fit after removing the largest outlier if $\tilde{\chi}^2_{best}/\tilde{\chi}^2_{worst} < 2$, where $\tilde{\chi}^2_{best}$ is the reduced chi squared for the best-fitting template, and $\tilde{\chi}^2_{worst}$ is that for the worst-fitting template. Source SEDs are not always well matched by any of the average spectra; the minimized $\tilde{\chi}^2$ ranges from 1.2 to 50, with a median value of 13. Although the templates were originally defined based on T_{bol}, the sources assigned to each category do not necessarily have bolometric temperatures that falls within the original T_{bol} bins.

There are a number of caveats to this analysis. Even for infinitely well-sampled SEDs, spectrum shape is not necessarily directly correlated with age or degree of embeddedness. For example, viewing geometry can have a strong effect on SED shape. In the three dimensional radiative transfer models of Whitney et al. (2003), Class I and Class II sources can have quite similar SEDs when viewed at the right inclination angle (e.g., when the observer's line-of-sight intersects the outflow opening angle of Class I sources). Even Class 0 sources can appear much warmer if we happen to be looking directly into the outflow cavity, although the probability of that occurring is small. In any case, the total mass of the envelope relative to the bolometric luminosity should be higher for more embedded sources, regardless of viewing angle.

6.8 Protostellar Evolution

We examine the evolution of cold protostars in more detail using the $L_{bol} - T_{bol}$ diagram, which is the protostellar equivalent of the H-R diagram (Myers et al., 1998), where T_{bol} is used as a measure of temperature rather than T_{eff}, which is not well-

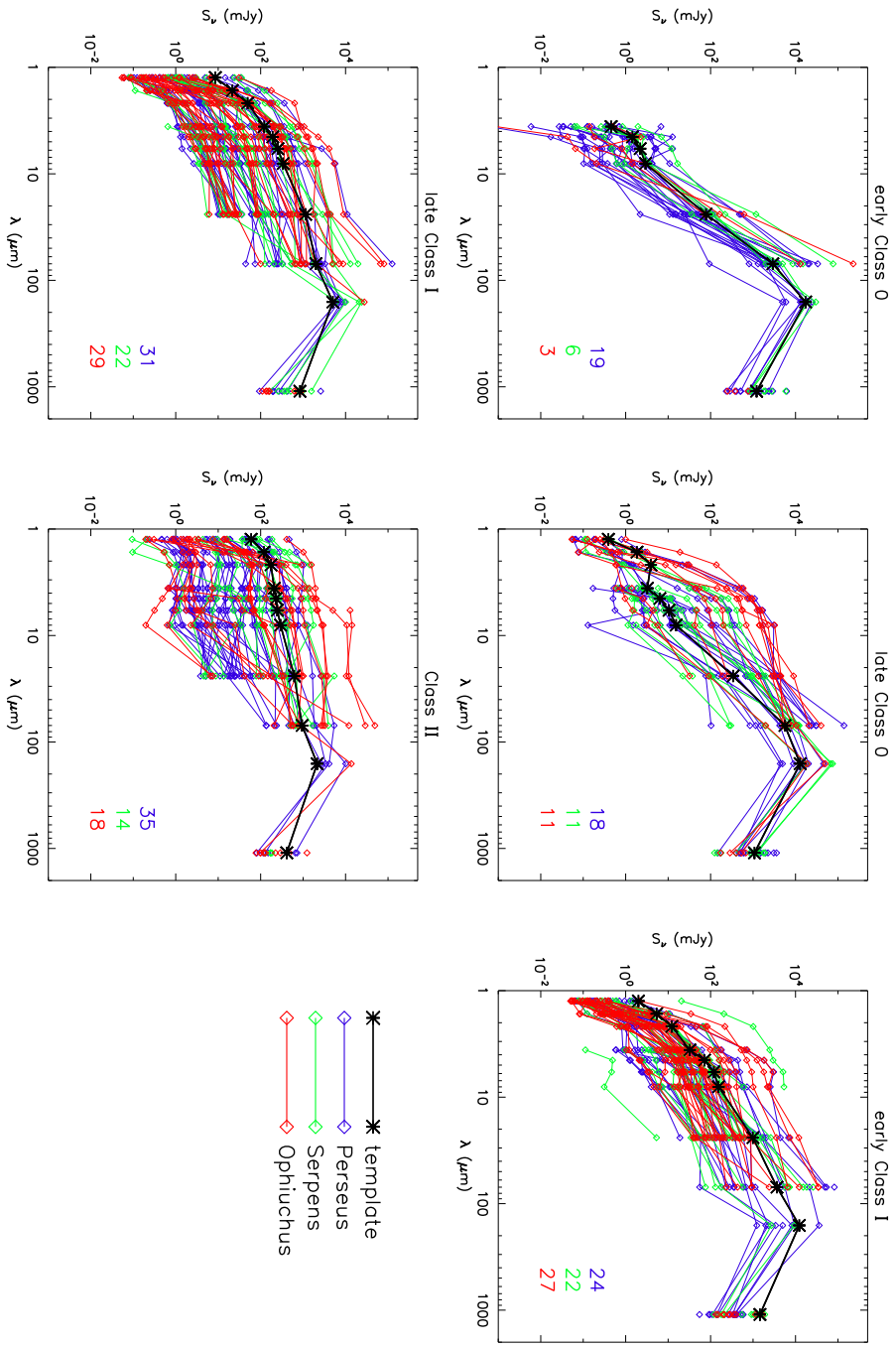

Figure 6.28 Results of fitting the SEDs of cold protostar candidates in Perseus, Serpens, and Ophiuchus to template spectra. Average spectra in T_{bol} bins of $T_{bol} < 50$ K, $50 < T_{bol} < 100$ K, $100 < T_{bol} < 300$ K, $300 < T_{bol} < 650$ K, and $T_{bol} > 650$ K, calculated from all sources in Perseus and Serpens, are used as templates (thick black lines). Spectra are color coded by cloud, and the number of sources in each category for each cloud are given in the lower right corners.

characterized for embedded sources. As discussed in Myers et al. (1998), newly-formed protostars should begin at low L_{bol} and T_{bol}, increasing in both L_{bol} and T_{bol} as accretion proceeds. If accretion abates or is otherwise halted, then L_{bol} will decrease for steadily increasing T_{bol}. Eventually, sources will move onto the main sequence, at $T_{bol} \gtrsim 3000$ K.

Figure 6.29 plots L_{bol} versus T_{bol} for the cold protostar samples in Perseus, Serpens, and Ophiuchus. Sources are color-coded according to whether they have reliable measured 160 μm fluxes (red squares), are saturated at 160 μm (blue circles), or are not detected at 160 μm (purple triangles). Given the discussion in §6.11 regarding the effect of missing 160 μm fluxes on the calculation of T_{bol}, blue circles would be expected to move up and to the right in this diagram for "cold" sources ($T_{bol} \lesssim 100$ K), and down and to the left for "warm" sources ($T_{bol} \gtrsim 100$ K), if 160 μm fluxes were available. The "saturated" category also include all sources for which we are unable to measure a 160 μm flux due to bad pixels or nearby saturated sources, but for which the inclusion of a 160 μm point would likely result in a decrease of the estimated T_{bol}.

Filled symbols are used for sources that are associated with a 1.1 mm core, while "+" symbols indicate sources with upper limits at 1.1 mm. While upper limits may be expected for sources with large T_{bol}, colder sources with no 1.1 mm detection must either be misclassified, e.g., they are actually faint red galaxies or more evolved objects, or very low mass sources whose 1.1 mm flux is below our detection limit. Our physical definition of Class I ($M_* \gtrsim M_{env}$) requires that any such objects have masses less than a few tenths of a solar mass, or have very little remaining envelope ($M_* \gg M_{env}$), to be undetected at 1.1 mm. Note that although we plot sources with 1.1 mm upper limits here, our final Class I sample includes only sources with 1.1 mm detections.

Protostellar evolutionary tracks, which predict source properties as a function of age and mass, can be easily compared to our data using the $L_{bol} - T_{bol}$ diagram. Model evolutionary tracks from Myers et al. (1998) (solid line) and Young & Evans (2005) (dotted lines) are shown in figure 6.29. From top to bottom, the Young & Evans (2005) models are for sources of mass 3.0, 1.0, and 0.3 $M_\odot$, assuming a constant

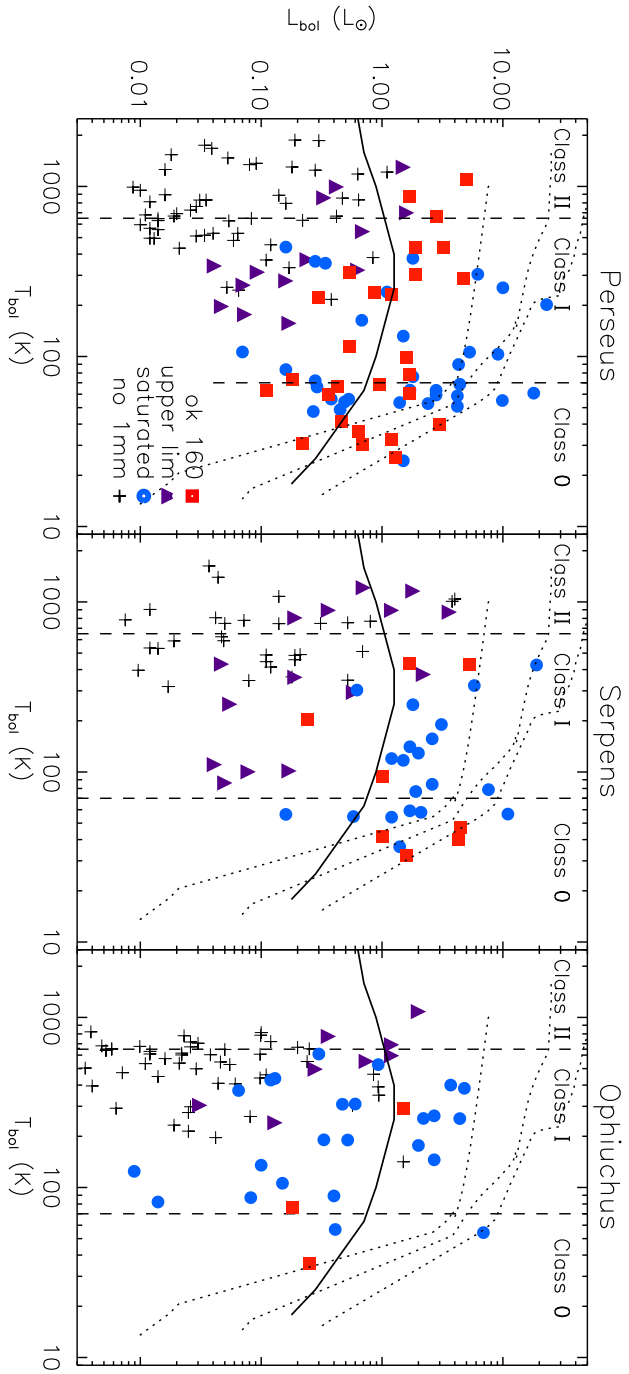

Figure 6.29 Bolometric luminosity plotted versus bolometric temperature ($L_{bol} - T_{bol}$ diagram) for the cold protostar samples in Perseus, Serpens, and Ophiuchus. Filled symbols indicate that a given protostar is associated with 1.1 mm emission, while "+" symbols indicate upper limits at 1.1 mm. The significance of colored symbols is explained in the text. Model evolutionary tracks from Young & Evans (2005) for sources with 3.0, 1.0, 0.3 $M_{\odot}$ (dotted lines, from top to bottom) and from Myers et al. (1998) for a source with final mass 0.3 $M_{\odot}$ (solid line) are shown for comparison. The number that lie below the evolutionary models indicate that neither a constant or steadily decreasing accretion rate match the observations. In fact, the large population of the low-luminosity Class I objects argues strongly for episodic accretion.

accretion rate or "Shu accretion": $dM/dt = c_s^3/G$, where c_s is the effective sound speed. These authors adopt the standard inside-out collapse model of Shu (1977), and assume that no mass is lost in the formation process. Finite masses are achieved by truncating the outer radius of the envelope. A one dimensional radiative transfer model (DUSTY) is used to calculate observational signatures (L_{bol}, T_{bol}, etc.) from the accretion model.

Unlike Young & Evans (2005), Myers et al. (1998) do not assume that that the entire mass of the original core ends up in the final star, but rather that a significant fraction of the core mass is lost in the star formation process. The Myers et al. (1998) model shown is for a source with initial core mass of 1.8 $M_\odot$ and final stellar mass of $0.3M_\odot$. The luminosity is lower than the Young & Evans (2005) tracks at later times because Myers et al. (1998) assume an accretion rate that is initially $dM/dt = c_s^3/G$, but falls off exponentially with time, designed to match the observed luminosity of pre-main sequence stars. Both evolutionary models assume an accreting central protostar, a circumstellar accretion disk, and an extended envelope, and a contribution to the luminosity from gravitational contraction of the protostar. Young & Evans (2005) also include nuclear (D) burning.

If we ignore for the moment the population of Class I sources in each cloud with L_{bol} values well below both models, the Myers et al. (1998) model, for which a large fraction of the core mass is ejected or dispersed, is more consistent with the observed protostellar sources. We conclude, therefore, that if the accretion rate is constant, star formation models in which 100% of the original core material is accreted onto the final star are unable to match the observed data. On the other hand, the ratio of the final stellar mass to initial core mass for the Myers et al. (1998) model shown ($f_{\rm eff} = 0.3/1.8 = 0.17$) is smaller than the lower limit $f_{\rm eff} \gtrsim 0.25$ derived in §6.5 comparing the CMD and IMF shapes, and also smaller than the value found by Alves et al. (2007) ($f_{\rm eff} = 0.3 \pm 0.1$).

This may be a moot point, however, as the fact that many points lie below all four model tracks indicates that neither a constant nor a steadily decreasing accretion rate are entirely consistent with the observed protostellar populations in these clouds. In

particular, the large population of Class I sources with low L_{bol} in each cloud, together with the lack of low-L_{bol} Class 0 sources, is difficult to understand in relation to most existing protostellar evolutionary models. A general feature of such models is that the bolometric luminosity peaks in the Class I stage, a result that is true for constant accretion rates (Young & Evans, 2005), decreasing rates (Myers et al., 1998), and gravo-turbulent models (Froebrich et al., 2006). Contrary to this prediction, we find that the mean luminosity of all Class I sources, is 1.92 $L_\odot$, compared to 2.4 $L_\odot$ for all Class 0 sources.

Given the above discussion and the large observed spread in L_{bol} of 2–3 orders of magnitude for Class I sources, we suggest that mass accretion during the Class I stage is episodic. Class I sources with low L_{bol} can be explained by periods of relative quiescence when the bolometric luminosity, which is driven primarily by accretion luminosity at this point, drops by at least a factor of 10. Conversely, Class I sources with high L_{bol} values, e.g., those that form the upper envelope of the distribution and appear to be consistent with the Young & Evans (2005) models, would correspond to periods where the accretion rate is close to the "Shu accretion" value. Episodic accretion is not an unreasonable assumption; evidence for variable mass accretion and ejection is plentiful, including that based on modeling FU Orionis eruptions (e.g., Hartmann & Kenyon, 1985), and bow shocks in Herbig-Haro outflows (e.g., Reipurth & Bally, 2001). Given the number of Class I sources with $L_{bol} < 0.1 L_\odot$ (11/39 in Perseus, 7/26 in Serpens, and 10/29 in Ophiuchus), we estimate that any given source spends approximately 25% of its Class I lifetime in a quiescent accretion state.

Although the observed distribution of L_{bol} for Class I sources is a strong argument for episodic accretion, that is not the only possibility. One alternative is that the low-L_{bol} Class I sources are simply very low mass objects, and we are somehow missing their low-mass Class 0 counterparts. We believe that this is unlikely, however. Based on our sensitivity limits at $70, 160$ μm and 1.1 mm, we should be able to detect Class 0 sources with L_{bol} at least as low as $0.03 L_\odot$. In figure 6.30 we show the average spectrum of low-luminosity Class I sources ($L_{bol} < 0.2 L_\odot$, $70 < T_{bol} < 650$ K) in

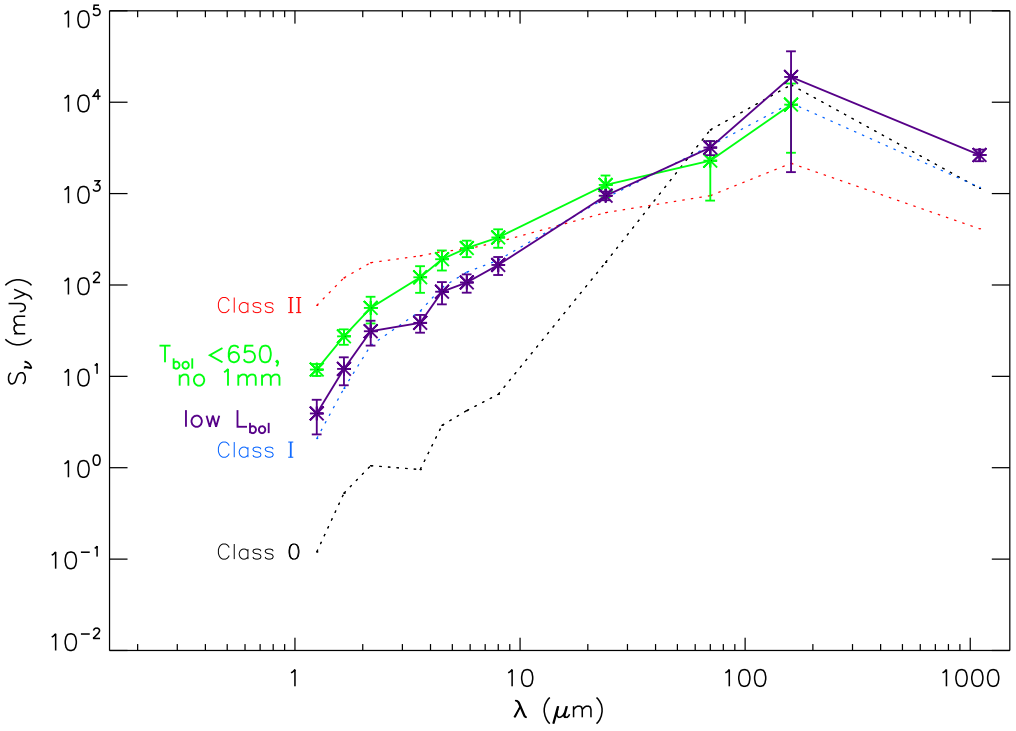

Figure 6.30 Average spectra of low-luminosity Class I sources (purple line), and sources that have $T_{bol} < 650$ K but no 1.1 mm emission ("non-envelope Class I"). The low-luminosity Class I sources appear to have relatively higher 160 μm and 1.1 mm fluxes compared to the shorter wavelength points, but are otherwise consistent with the average Class I spectrum (blue dotted line). The average non-envelope Class I spectrum is intermediate between the average Class I and Class II spectra, as expected if these represent an evolved stage in which there is little or no remaining envelope.

Perseus and Serpens that are detected at 1.1 mm (purple line). On average, these sources appear to have relatively higher 160 μm and 1.1 mm fluxes compared to the shorter wavelength points, but are otherwise consistent in shape with the average Class I spectrum (blue dotted line). Most of these sources also lack 160 μm fluxes which could cause an underestimate of L_{bol}.

The envelope mass M_{env} of protostellar sources in each cloud is plotted versus T_{bol} in figure 6.31. Symbols are the same as in figure 6.29, except that upper limits at 1.1 mm are now represented by arrows. Solid lines indicate the Young & Evans (2005) evolutionary tracks as before (top to bottom 3.0, 1.0, and 0.3 $M_\odot$). Sources

in all three clouds show a weak but consistent correlation of decreasing M_{env} with increasing T_{bol}, exactly the trend expected if the envelope is gradually depleted by accretion onto the protostar as sources evolve toward higher T_{bol}. This trend is not an effect of including the 1.1 mm flux, from which the envelope mass is derived, in the calculation of T_{bol}; the same trend is apparent even if T_{bol} is calculated by excluding the 1.1 mm flux point. Some warmer sources have high 1.1 mm upper limits because they lie in regions of extended or confused emission. Our determination that these sources are not actually associated with the 1.1 mm emission is based on visual examination of the images and SEDs.

In contrast to the $L_{bol} - T_{bol}$ diagram, the Young & Evans (2005) model tracks fit the $M_{env} - T_{bol}$ distribution quite well. Thus a constant accretion rate reproduces the decrease in envelope mass with increasing T_{bol}, although it does not fit the evolution of L_{bol}. The distribution of M_{env} versus T_{bol} can also be understood in relation to an episodic accretion scenario, however. The rate of mass transfer from the envelope to the accretion disk likely remains constant even in an episodic scenario, with the accretion rate from the disk to the protostar being the variable quantity (e.g., Kenyon & Hartmann, 1995). Therefore the envelope mass will steadily decrease with increasing T_{bol} even for variable accretion. Note that accretion stops when the envelope mass, as defined by the outer radius, has been exhausted. In the context of the Young & Evans (2005) models, the spread of M_{env} as function of T_{bol} suggests stellar masses in the range $M \sim 0.3 - 4$ $M_\odot$ in Perseus and Serpens, and $M \sim 0.1 - 1.5$ $M_\odot$ in Ophiuchus.

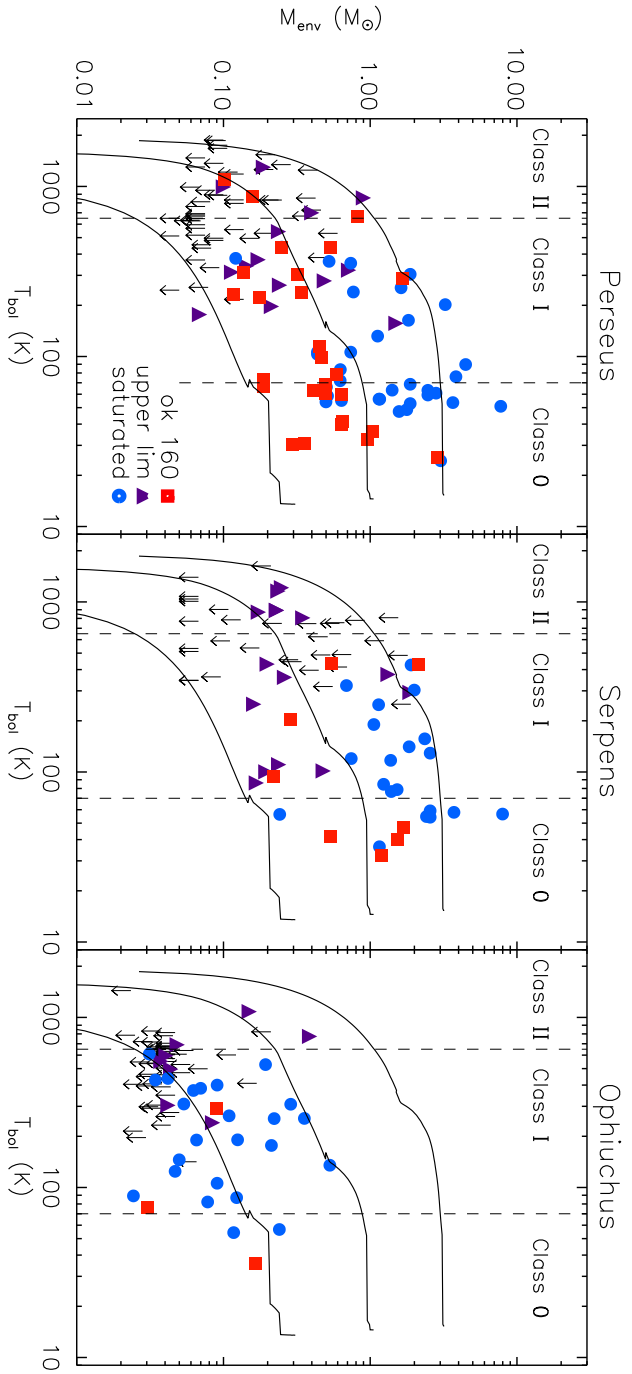

Figure 6.31 Envelope mass versus bolometric temperature for cold protostars in Perseus, Serpens, and Ophiuchus. Filled symbols indicate that a given protostar is associated with 1.1 mm emission, while sources with upper limits at 1.1 mm are plotted as arrows. Solid lines show the predictions of protostellar evolutionary models from Young & Evans (2005) for sources of mass (from top to bottom) 3.0, 1.0, 0.3 $M_{\odot}$. The Young & Evans (2005) models describe the evolution of mass with T_{bol} quite well, in contrast to what was seen for the luminosity (figure 6.29).

6.9 Lifetimes

If we assume that star formation in these clouds is a steady-state process (i.e., not occurring in bursts), and that the starless–Class 0–Class I classifications represents a true evolutionary sequence, then we can use the number of objects in consecutive evolutionary phases to estimate the relative lifetimes of those phases. As we ultimately calibrate our timescales based on the lifetime of the Class II phase ($\sim 10^6$ yr; Kenyon et al. 1990), star formation must have been steady in time for at least the last 1 Myr. In addition, we must assume that there are no significant dependence of the timescales on source mass. Despite a number of assumption that are required, this kind of analysis has the advantage of being quite straightforward to carry out, and it does not rely on an assumed accretion rate or star-formation model.

Table 6.6 list the total number of starless cores, Class 0, and Class I protostars in each cloud, as well as the ratios of the numbers of Class 0 to Class I sources, and starless cores to embedded protostars ($N_{emb} = N_{Class0} + N_{ClassI}$) for all three clouds. The average mean density of the starless core samples $\langle n \rangle_{SL}$, and corresponding free-fall timescale $t_{\rm ff}$, are also given for each cloud. The free-fall time is the timescale on which starless cores will collapse in the absence of internal support, and is calculated from the mean particle density (Spitzer, 1978):

$$t_{ff} = \sqrt{\frac{3\pi}{32G\rho}} = \sqrt{\frac{3\pi}{32G\langle n \rangle \mu_p m_H}}, \tag{6.6}$$

where m_H is the mass of hydrogen and $\mu_p = 2.33$ is the mean molecular weight per particle.

6.9.1 Timescale of the Class 0 Phase

There are approximately half as many Class 0 as Class I sources in Perseus and Serpens ($N_{Class0}/N_{ClassI} = 0.7$ and 0.4, respectively), suggesting that the Class 0 phase lasts roughly half as long as the Class I phase. For a total embedded timescale of 4×10^5 yr (Evans et al., in preparation), these ratios imply Class 0 timescales of

Table 6.6. Relative numbers of starless, Class 0, and Class I sources

Cloud	N_{SL}	$\langle n \rangle_{SL}$ (cm^{-3})	t_{ff} (yr)	N_{Class0}	N_{ClassI}	N_{Class0}/N_{ClassI}	N_{SL}/N_{emb}[1]
Perseus	67	1.3×10^5	9×10^4	29	39	0.7	1.0
Serpens	15	1.6×10^5	8×10^4	11	26	0.4	0.4
Ophiuchus	26	8.2×10^5	4×10^4	3	29	0.1	0.8

Note. — The free-fall timescale t_{ff} of starless cores is calculated from the mean density $\langle n \rangle_{SL}$ of the starless samples in each cloud using equation (6.6). The numbers of Class 0 and Class I sources are based on T_{bol} classifications: $T_{bol} < 70$ K (Class 0) and $70 < T_{bol} < 650$ K (Class I), with the additional requirement that Class I sources be detected at 1.1 mm.

[1]N_{emb} refers to the total number of embedded protostars, i.e., those in the Class 0 and Class I phases: $N_{emb} = N_{Class0} + N_{ClassI}$.

$t_{Class0} \sim 1.7 \times 10^5$ yr in Perseus, and 1.2×10^5 yr in Serpens. These lifetimes are significantly longer than a number of previous estimates of $t_{Class0} \sim 10^4$ yr, based both on the number of Class 0 sources in Ophiuchus (André & Montmerle, 1994), and on comparison to evolutionary models ($2 - 6 \times 10^4$ yr; Froebrich et al. 2006). A short Class 0 lifetime has been interpreted as evidence for a period of very rapid accretion early in the evolution of protostars (e.g., Visser, Richer, & Chandler, 2002). Our results in Perseus and Serpens argue against such a rapid accretion phase, however. Although accretion may decrease somewhat in Class I (or become episodic, see §6.8), it appears unlikely that the *average* accretion rate drops by more than a factor of two from Class 0 to Class I, based on the relative lifetimes of the two phases.

The derived Class 0 lifetimes for Perseus and Serpens are similar to the results of Visser et al. (2002) for a sample of Lynds dark clouds ($t_{Class0} \sim 2 \times 10^5$ yr), and to the recent findings of Hatchell et al. (2007) that the Class 0 lifetime in Perseus is similar to the Class I timescale. Our large, unbiased sample provides a distinct advantage over many other previous studies, which have necessarily relied on small samples or accumulated sources from a number of different surveys, wavelengths, and

detection methods. For example, the Visser et al. (2002) Class 0 sample consists of 7 sources, and the André & Montmerle (1994) timescale for Ophiuchus is based on 1 Class 0 object. Froebrich et al. (2006) note that their 50 Class 0/I sources come from a variety of sources including NIR imaging of outflows, IRAS data, submillimeter and millimeter mapping, and radio continuum surveys, causing their source sample to be subject to strong selection effects. The recent work by Hatchell et al. (2007) comparing SCUBA 850 μm maps and *Spitzer* c2d data of Perseus, with 34 Class 0 sources, is a notable exception. Within each cloud our surveys are very uniform, providing protostellar samples that are not biased by selection effects. For this reason, our estimated Class 0 lifetimes should be more robust than many previous measurements.

The results in Ophiuchus are strikingly different from Perseus and Serpens, with 10 times more Class I than Class 0 sources. In fact, our results for Ophiuchus are consistent with previously observed ratios of $N_{Class0}/N_{ClassI} \sim 1/10$ in that cloud (André & Montmerle, 1994), and with the resulting estimates of a very short Class 0 lifetime ($t_{Class0} \sim 10^4$ yr). More precisely, we find $t_{Class0} \sim 4 \times 10^4$ yr. There are two obvious, but conflicting, explanations for the much smaller N_{class0}/N_{ClassI} ratio in Ophiuchus. First, star formation may be highly temporally variable in Ophiuchus. Visser et al. (2002) suggest that a burst of star formation approximately 10^5 yr ago is responsible for the large ratio of Class I to Class 0 sources. Alternatively, the Class 0 phase may be much shorter in Ophiuchus than in the other two clouds due to higher accretion rates at early times. While a burst of star formation seems the more likely explanation, accretion rates, and thus lifetimes, could conceivably depend on cloud environment, particularly mean density.

Complicating both these scenarios is the fact that bolometric temperatures may be underestimated for sources without a 160 μm flux measurement, as discussed in §6.11. The lack of 160 μm fluxes is especially problematic in Ophiuchus, where the majority of sources are either saturated at 160 μm or in regions of saturated pixels, and may be partially responsible for the small number of observed Class 0 sources in that cloud. When we fit the SEDs of Ophiuchus sources to the average Class 0 and Class I spectra (§6.7.1), we find as many as 8 sources are classified as Class 0. If these

are true Class 0 objects, the ratio of Class 0 to Class I sources becomes similar to the other clouds (~ 0.4). Note that the spectra of 4 of these vary considerably from the average Class 0 spectrum, however (figure 6.26), and their deeply embedded nature is suspect.

Recall that we only include sources in our Class I sample if they are detected at 1.1 mm This criteria excludes 24 sources in Perseus with $70 < T_{bol} < 650$ K, 18 sources in Serpens, and 36 in Ophiuchus ("+" symbols in figure 6.29). The average spectrum of these "non-envelope Class I" sources is shown in figure 6.30 (green line, Perseus and Serpens only). The average spectrum appears to be intermediate between the "envelope Class I" (blue dotted line) and Class II (red dotted line) averages. Furthermore, the mean T_{bol} values of these "non-envelope Class I" sources (570 K in Perseus, 520 K in Serpens, and 500 K in Ophiuchus) confirm that they fall at the warm end of the Class I distribution. While it is possible that we are simply not detecting the envelopes of these sources (e.g., if $M_{env} \lesssim 0.1$ $M_\odot$ or they are very extended), it seems more likely that the transition from Class I (protostars that retain an envelope) to Class II (pre-main sequence stars with no envelope) occurs closer to $T_{bol} = 500$ K than $T_{bol} = 650$ K for these data.

When we include *all* sources with $T_{bol} < 650$ K in our Class I sample, dropping the requirement that they be detected at 1.1 mm, the ratio of Class 0 to Class I sources becomes 0.5 in Perseus, 0.3 in Serpens, and 0.05 in Ophiuchus. This represents only a 25–30% change in the Class 0 lifetime for each cloud, but does bring Serpens ($t_{Class0} \sim 0.6 - 1.2 \times 10^5$ yr), closer the "short Class 0" value.

6.9.2 Timescale of the Prestellar Phase

Assuming that all of the starless cores in our sample are in fact prestellar, and will eventually collapse to form stars or brown dwarfs (see §6.5), we can use the relative number of starless cores and embedded protostars to estimate the prestellar core lifetime. Knowing this prestellar timescale is essential for understanding the physical processes that govern the formation, support, and collapse of star-forming

cores. The ratio of the number of starless cores to the number of embedded protostars is $N_{SL}/N_{emb} = 1.0$ in Perseus, 0.4 in Serpens, and 0.8 in Ophiuchus, where $N_{emb} = N_{Class0} + N_{ClassI}$. For an embedded protostar phase that lasts $t_{emb} = 4 \times 10^5$ yr (Evans et al., in preparation), the observed ratios imply prestellar core lifetimes of 4×10^5 yr in Perseus, 2×10^5 yr in Serpens, and 3×10^5 yr in Ophiuchus.

We also found approximately equal numbers of protostellar and starless cores in all three clouds (table 6.1), further confirmation that the timescale for starless cores is similar to that of the embedded protostellar phase. Thus, the dense starless cores we are sensitive to lasts $2 - 4 \times 10^5$ yr in all three clouds. Approximately equal timescales for the prestellar and embedded protostellar phases were also found recently by Jørgensen et al. (2007) in Perseus using SCUBA maps and *Spitzer* c2d data. Furthermore, our values are only a factor of two shorter than the timescale derived by (Visser et al., 2002) for a sample of Lynds dark clouds.

The prestellar lifetime can be compared to the free-fall time for starless cores, calculated from the mean densities of the starless core samples in each cloud: $t_{ff} \sim 9 \times 10^4$ yr in Perseus and 8×10^4 yr in Serpens, based on mean densities of 1.3×10^5 cm^{-3} and 1.6×10^5 cm^{-3}, respectively. Thus prestellar cores last for only a few free-fall times in both Perseus and Serpens. Such a short core lifetime is inconsistent with the classical picture of magnetic support, in which the evolution of highly sub-critical cores is moderated by ambipolar diffusion (Shu et al., 1987). Specifically, in the magnetic paradigm prestellar cores should have lifetimes similar to the ambipolar diffusion timescale, or $t_{AD} \sim 7 \times 10^6$ yr for typical ionization levels in low-mass star forming regions (e.g., Evans, 1999), which is more than an order of magnitude longer than our results. The calculated free-fall time is much shorter in Ophiuchus, however, due to higher mean densities, and a lifetime of $\sim 8 t_{ff}$ may be more consistent with ambipolar diffusion. Note that higher core densities were found to be a result of the higher linear resolution in Ophiuchus (§5.4), so it is possible that mean densities in the other clouds could be underestimated.

It is also important to emphasize here that our Bolocam surveys are sensitive to cores with relatively high mean density ($n \gtrsim 2 - 3 \times 10^4$ cm^{-3}). It is quite

possible, therefore, that we are sampling only the densest end stage in a longer core evolutionary picture, in which case a magnetic field dominated scenario might still be applicable at early times (e.g., Tassis & Mouschovias 2004). Ciolek & Basu (2001) also note that t_{AD} can be as short as a few free-fall times for marginally sub-critical cores.

6.10 Conclusions

Utilizing large-scale 1.1 mm surveys (Enoch et al., 2006; Young et al., 2006; Enoch et al., 2007) together with *Spitzer* IRAC and MIPS maps from the c2d Legacy program (Evans et al., 2003), we have constructed an unbiased census of prestellar cores and deeply embedded protostars in the Perseus, Serpens, and Ophiuchus molecular clouds. We first assembled a sample of candidate cold protostars in each cloud, and used them to distinguish starless cores from cores that have an internal luminosity source (protostellar cores).

Cloud environment appears to have a significant effect on the physical properties of starless cores, and how such properties are altered by the formation of a central protostar. Starless cores in Perseus are larger and have lower mean densities than protostellar cores, by factors of 1.3 and 3.7, respectively. Thus there is a relatively simple scenario by which protostellar cores might have evolved from starless cores in that cloud, becoming smaller and denser at a fixed mass. In Serpens, however, it is not clear how the relatively massive protostellar cores ($\langle M \rangle = 2.1$ M$_\odot$) could have evolved from the current population of compact, low mass starless cores ($\langle M \rangle = 0.9$ M$_\odot$), unless cores merge at later times. By contrast to both Serpens and Perseus, we see essentially no difference in Ophiuchus between cores that have formed stars and those that have not.

We also investigate the spatial clustering of cores, and relationship to the local cloud column density, as traced by visual extinction. Starless cores are observed to have a lower degree of spatial clustering in all three clouds, based on the amplitude of the two-point correlation function. For Perseus and Serpens this result is supported by

the peak surface density of cores, which is higher for protostellar cores by a factor of 1.5 to 2 In all three clouds both starless and protostellar cores are only found at relatively high cloud column densities: 75% of cores are associated with $A_V \gtrsim 7 - 8.5$ mag in Perseus, $A_V \gtrsim 9.5 - 16$ mag in Serpens, and $A_V \gtrsim 19.5 - 23$ mag in Ophiuchus. An extinction threshold for forming dense cores at $A_V = 4 - 8$ mag has been suggested for magnetically supported clouds (McKee, 1989). Our results are consistent with this prediction, but only in Ophiuchus is a true threshold observed; in that cloud only two cores are found at $A_V < 17$ mag.

Assuming that all of our starless cores will eventually form stars, we construct the combined prestellar core mass distribution (CMD) with the 108 starless cores from all three clouds. The combined starless core mass distribution has a slope of $\alpha = -2.5 \pm 0.2$, consistent with recent measurements of the stellar initial mass function ($\alpha = -2.4$ to -2.8). Our result lends support to the idea that stellar masses are directly linked to the core formation process. The relationship of the prestellar CMD to the combined protostellar CMD, however, is more complex than anticipated if protostellar cores were originally drawn from the prestellar CMD. Although the protostellar CMD has a wider distribution to smaller masses as expected if core mass is lost to accretion, the high-mass tail of the protostellar CMD is difficult to understand unless any future star formation in these clouds will result in stars of lower mass than the current generation of protostars.

After examining the starless and protostellar core populations, we focus on the properties of the cold protostar samples. Bolometric luminosities, temperatures, and envelope masses are calculated for the candidate Class 0 and Class I sources in each cloud (tables 6.2–6.4). Our sample includes a total of 43 Class 0 sources and 94 Class I sources, with approximate detection limits of $M_{env} > 0.2$ $M_\odot$ and $M_{env} > 0.1$ $M_\odot$ for Class 0 and Class I sources, respectively. We compare different protostellar classification methods, concluding that the bolometric temperature is a better measure of evolutionary state than the near- to mid-infrared spectral index, α_{IR}, for deeply embedded sources.

Observed source properties are compared to protostellar evolutionary models using

the bolometric temperature-luminosity ($L_{bol} - T_{bol}$) diagram, the protostellar equivalent of the H-R diagram (Myers et al., 1998). Neither models with a constant mass accretion rate (Young & Evans, 2005), nor those with an exponentially decreasing rate (Myers et al., 1998) fit the observed sources. In particular, there is a large population of low luminosity Class I sources that cannot be explained by the general prediction that L_{bol} should peak during the Class I phase. We interpret this result as evidence for episodic accretion during the Class I stage; based on the number of sources with $L_{bol} < 0.1 L_{\odot}$, protostars should spend approximately 25% of their Class I lifetime in a quiescent accretion state.

Finally, the relative number of starless, Class 0, and Class I sources are used to estimate timescales for the dense prestellar core and Class 0 phases. There are approximately half as many Class 0 as Class I sources in Perseus and Serpens, implying a Class 0 timescale of $1 - 2 \times 10^5$ yr. In Ophiuchus the fraction of Class 0 sources is much smaller ($N_{Class0}/N_{ClassI} \sim 0.1$). Part of this difference may be due to the lack of reliable 160 μm flux measurements in Ophiuchus, but it seems likely that the Class 0 phase is either much shorter in that cloud or that a burst of star formation is responsible for the large population of Class I objects. In all three clouds the lifetime of dense prestellar cores is approximately equal to the timescale of the embedded protostellar phase, or $2 - 5 \times 10^5$ yr. Such a short prestellar core lifetime, only a few free-fall timescales in Perseus and Serpens, is inconsistent with a scenario in which core support and evolution is dominated by magnetic fields, in which case the lifetime should be similar to the ambipolar diffusion timescale, $t_{AD} \sim 10^7$ yr. These observations might still be consistent with ambipolar diffusion if we are only observing the densest stages of a longer-scale core evolution.

Acknowledgments

Support for this work, part of the Spitzer Legacy Science Program, was provided by NASA through contracts 1224608 and 1230782 issued by the Jet Propulsion Laboratory, California Institute of Technology, under NASA contract 1407. Additional

support was obtained from NASA Origins Grant NNG04GG24G to the University of Texas at Austin. Support for the development of Bolocam was provided by NSF grants AST-9980846 and AST-0206158.

6.11 Appendix: Calculating the bolometric luminosity and temperature

We use two different methods to do the integrations over frequency in equations 6.3–6.4. The first (linear) method uses power law fit between flux points. For example, the fit between measured flux density points at λ_j and λ_{j+1} is given by $S(\lambda) = 10^b \lambda^m$, with

$$m = \frac{\log(S(\lambda_{j+1})/S(\lambda_j))}{\log(\lambda_{j+1}/\lambda_j)}, \text{ and } b = \log S(\lambda_j) - m \log \lambda_j. \tag{6.7}$$

The SED is extrapolated from the longest wavelength flux using $S_\nu \propto \nu^2$. The second (midpoint) method utilizes a simple midpoint interpolation. In both methods flux upper limits are treated as zero and removed from the fit (i.e., we interpolate over them). Uncertainties in flux density measurements are included in the midpoint calculation, and used to estimate formal fitting errors for T_{bol} and L_{bol}.

Figure 6.32 compares the results of using the linear and midpoint methods to calculate L_{bol} and T_{bol} for the cold protostar sample in Perseus. Except for the coldest sources, the midpoint T_{bol} is lower than the linear T_{bol}, by about 10%. Conversely, L_{bol} calculated by the midpoint method is nearly always higher than the linear L_{bol}. It is not unexpected that the linear estimate of L_{bol} would be too low, as a linear fit to a blackbody function will always be an underestimate to the true flux. The expected behavior for T_{bol} is not so clear, however.

To further test this behavior, we plot in figure 6.33 the fractional errors due solely to finite sampling, for L_{bol} and T_{bol} calculated from input blackbody spectra. Blackbody sources with input T_{bol} from 5–5000 K are sampled at the observed wavelengths (λ =1.25, 1.65, 2.17, 3.6, 4.5, 5.8, 8, 24, 70, 160, 1100 μm), and the bolometric temperature and luminosity calculated by the linear (left) and midpoint (right) methods. As anticipated, the linear L_{bol} is an underestimate of the true value, by more than 20% for input $T_{bol} \lesssim 300$ K. The linear T_{bol} is often underestimated as well, but by less than 10%. In contrast, the midpoint L_{bol} is higher than the true values for input $T_{bol} \lesssim 200$ K, by up to 20%. Although the amplitude of the fractional errors on T_{bol}

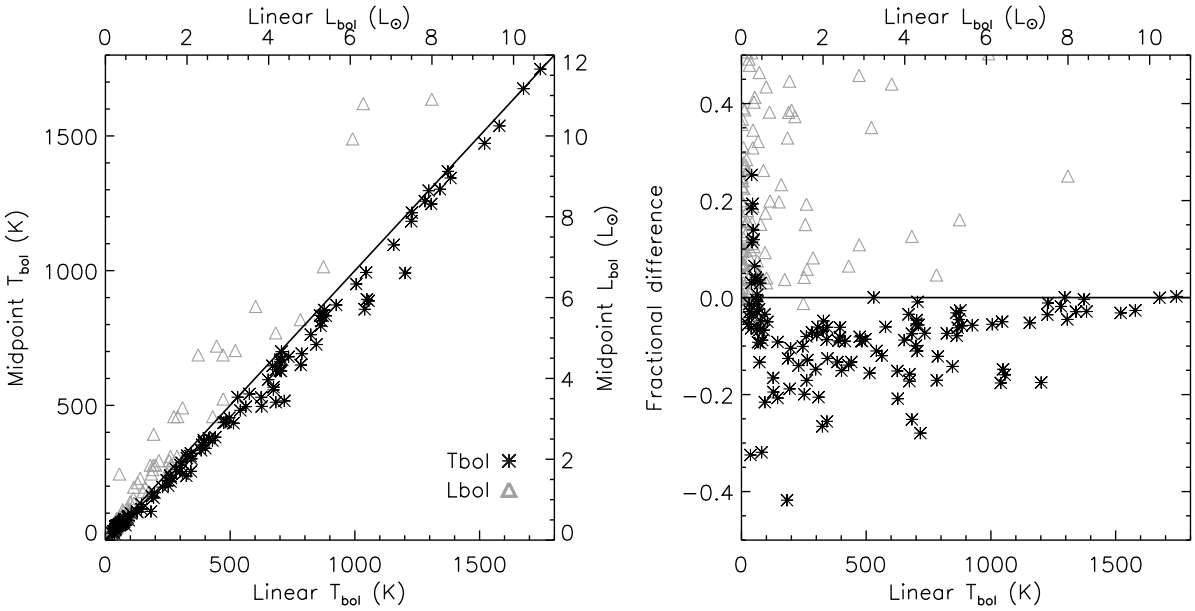

Figure 6.32 Comparison of the linear and midpoint methods for calculating L_{bol} and T_{bol}, for sources in Perseus. *Left*: Linear and midpoint T_{bol} (black asterisks) and L_{bol} (triangles) values are plotted for all cold protostar candidates in Perseus. *Right*: Fractional difference between the linear and midpoint methods, plotted as (midpoint-linear)/linear. L_{bol} calculated by the midpoint method is nearly always higher than the linear L_{bol}, and it is not unexpected that the linear value should be an underestimate. Except for the coldest sources, the midpoint T_{bol} is lower than the linear T_{bol} by 10–20%.

are larger for the midpoint method, they are centered on zero, and thus the midpoint method provides a more *accurate*, if not more *precise*, measurement of L_{bol} and T_{bol}. Based on figures 6.32–6.33, we use the midpoint method throughout this chapter, although it must be noted that the blackbody spectra tested here are not necessarily representative of the more complicated observed SEDs.

In general, measured 160 μm fluxes are uncertain by up to a factor of 2, due to unquantified saturation effects and calibration uncertainties, and in many cases we are unable to measure a 160 μm flux at all. In addition, the "point-source" 160 μm fluxes of extended sources will likely be underestimated, because they are measured with a PSF fit rather than aperture photometry. Missing or severely underestimated fluxes at 160 μm can significantly affect both L_{bol} and T_{bol} for cold sources that peak

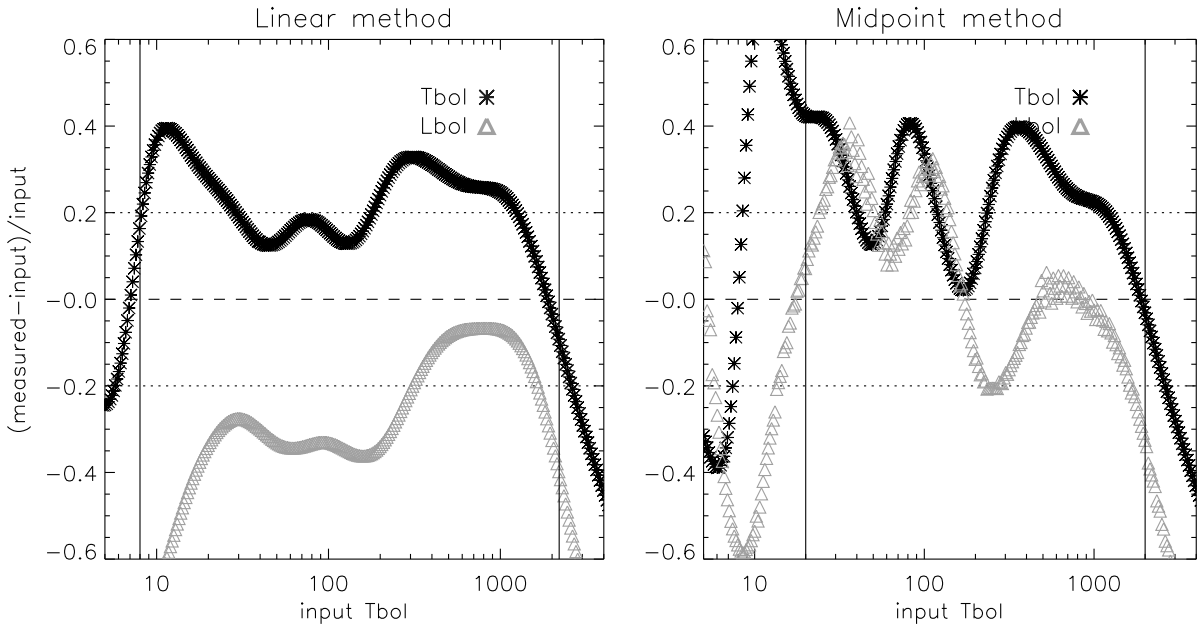

Figure 6.33 Characterization of sampling errors for T_{bol} and L_{bol} calculated using the linear (left) and midpoint (right) methods. The fractional difference between the input (T_{bol},L_{bol}) of blackbody spectra and the measured values when SEDs are sampled at the observed wavelengths is plotted as a function of input T_{bol}. The linear L_{bol} is underestimated, as expected. Although the absolute amplitude of the T_{bol} errors are smaller for the linear method, the midpoint method tends to be more accurate. Source SEDs, which are not pure blackbodies, may behave differently.

near 100 μm. As we are primarily interested in the coldest sources, we attempt here to quantify the effects of missing or underestimated 160 μm flux. One way of approaching this problem is to examine sources for which we have additional information near the peak of the SED, e.g., from IRAS or SHARC 350 μm observations.

We first look at two example sources, one cold ($T_{bol} \sim 33$ K), and one warmer ($T_{bol} \sim 163$ K). The colder source (IRAS 03282+3039) is isolated, so we can use the IRAS fluxes without worrying about confusion due to the large IRAS beam. We calculate the "true" L_{bol} and T_{bol} by including the IRAS 60 and 100 μm fluxes, a SHARC II 350 μm flux (Wu et al., in preparation), and a MIPS 160 μm flux measured in a large aperture, which is almost two times higher than the PSF-fit flux. Using the underestimated point source 160 μm flux, and no longer including IRAS or SHARC II data, causes an *underestimate* of L_{bol} by 35% and an *overestimate* of T_{bol} by 15%

compared to the "true" values. Omitting the 160 μm point altogether, as would be appropriate for saturated sources, results in an underestimate of L_{bol} by 7% and an overestimate of T_{bol} by 9%.

Thus we conclude that while the 160 μm point is important for characterization of the SED of cold objects, our integration method can interpolate over a missing 160 μm flux to estimate L_{bol} and T_{bol} to with 20% for cold sources. Severly underestimated 160 μm flux densities will cause larger errors of up to 50%. Using a similar procedure for the warmer source (T_{bol} = 163 K), we find that omitting the 160 μm flux results in errors in the opposite sense compared to the colder source: an *overestimate* of L_{bol} by 28% and an *underestimate* of T_{bol} by 18%.

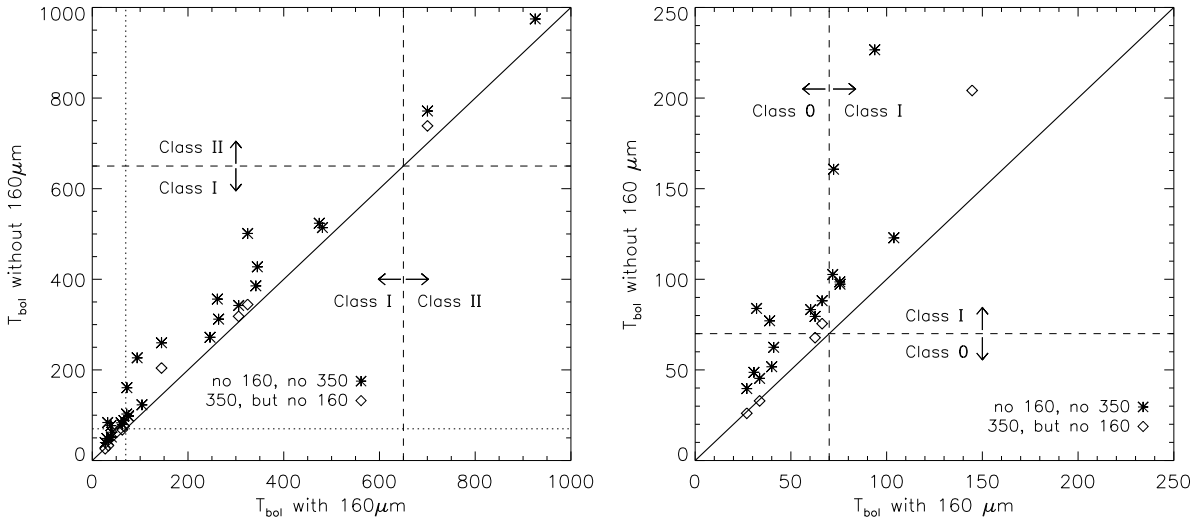

Figure 6.34 Characterization of the systematic errors introduced for T_{bol} when a 160 μm flux density is not available. *Left*: For all sources in Perseus with a reliable 160 μm flux, we calculate T_{bol} with and without the 160 μm point (asterisks). T_{bol} is always overestimated when the 160 μm flux is missing, but it does not change the classification of Class I sources for these data. *Right*: Similar, but with the scale adjusted to highlight lower T_{bol} sources. Not having a 160 μm point does change the classification of approximately half of the Class 0 ($T_{bol} < 70$ K) sources. Errors are substantially reduced when a flux at 350 μm is available (diamonds).

For a more general result, we compare T_{bol} calculated with the 160 μm flux included in the SED to the value found by omitting the 160 μm point, for all sources in Perseus

with a measured 160 μm flux (figure 6.34, left panel). For this plot, we have adopted Class 0/Class I/Class II divisions from Chen et al. (1995). Source classifications are discussed in §6.7. Although T_{bol} calculated without the 160 μm flux is always overestimated compared to T_{bol} calculated with the 160 μm flux, it is never a large enough effect to shift the source classification of objects with $T_{bol} \gtrsim 100$ K (e.g., from Class I to Class II). This is not the case for Class 0 sources, however, as can be seen in the right panel of figure 6.34, where the scale has been adjusted to highlight the lowest T_{bol} values. Five sources that have $T_{bol} < 70$ K (Class 0) when including the 160 μm flux are shifted to $T_{bol} > 70$ K (Class I) when a 160 μm flux is not available. If a published 350 μm flux is available (diamonds), the errors in T_{bol} resulting from excluding the 160 μm flux are almost completely eliminated. Therefore we include 350 μm fluxes in the calculation of T_{bol} when available (nine sources in Perseus).

Based on figures 6.32–6.34 and the above examples, we estimate overall uncertainties for measured L_{bol} and T_{bol} values of $20-50\%$, depending on whether or not a 160 μm flux is available. If we are unable to measure a 160 μm flux, T_{bol} will almost certainly be an overestimate for very cold sources, which may affect our classification of protostellar candidates.

Bibliography

Adams, F. C., & Fatuzzo, M. 1996, ApJ, 464, 256

Adams, F. C., Lada, C. J., & Shu, F. H. 1987, ApJ, 312, 788

Alves, J., Lada, C. J., & Lada, E. A. 2001, Nature, 409, 159

Alves, J., Lombardi, M., & Lada, C. J. 2007, A&A, 462L, 17

André, P. 1994, *The Cold Universe*, editors Montmerle, T., Lada, C. J., Mirabel, I. F., & Tran Thanh Van, J. Gif-sur-Yvette, Editions Frontieres, p. 179

André, P., & Montmerle, T. 1994, ApJ, 420, 837

André, P., Ward-Thompson, D., & Barsony, M. 1993, ApJ, 406, 122

Aspin, C., Sandell, G., & Russell, A. P. G. 1994, A&AS 106 165

Beckwith, S. V. W. & Sargent, A. I. 1996, Nature, 383, 139

Beckwith, S. V. W., Sargent, A. I., Chini, R. S., & Güsten, R. 1990, 99, 924

Bonnell, I. A., Bate, M. R., Clarke, C. J., & Pringle, J. E. 2001, 323, 785

Bonnor, W. B. 1956, MNRAS, 116, 351

Chabrier, G. 2005 in The Stellar Initial Mass Function Fifty Years Later, editors E. Corbelli, F. Palla, and H. Zinnecker, p. 41

Chen, H., Myers, P. C., Ladd, E. F., & Wood, D. O. S. 1995, ApJ, 445, 377

Ciolek, G. E., & Basu, S. 2001, ApJ, 547, 272

Cohen, M. & Kuhli, L. V. 1979, ApJS, 41, 743

Crutcher, R. M. 1999, ApJ, 520, 706

Di Francesco, J., Evans, N. J., II, Caselli, P., Myers, P. C., Shirley, Y., Aikawa, Y., & Tafalla, M. 2007, in Protostars and Planets V, editors B. Reipurth, D. Jewitt, and K. Keil, p. 17

Ebert, R. 1955, Zeitschrift Astrophysics, 37, 217

Enoch, M. L., Young, K. E., Glenn, J., Evans, N. J., II, Golwala, S., Sargent, A. I., Harvey, P., et al. 2006, ApJ, 638, 293

Enoch, M. L., Glenn, J., Evans, N. J., II, Sargent, A. I., Young, K. E., & Huard, T. L., ApJ, in press

Evans, N. J., II 1999, ARA&A, 37, 311

Evans, N. J., II, Allen, L. E., Blake, G. A., Boogert, A. C. A., Bourke, T., Harvey, P. M., Kessler, J. E., et al. 2003, PASP, 115, 965

Evans, N. J., II, Rawlings, J. M. C., Shirley, Y. L., & Mundy, L. G. 2001, ApJ, 557, 193

Evans, N. J., II, et al. 2007, Final Delivery of Data from the c2d Legacy Project: IRAC and MIPS

Froebrich, D., Schmeja, S., Smith, M. D., & Klessen, R. S. 2006, MNRAS, 368, 435

Greene, T. P., Wilking, B. A., André, P., Young, E. T., & Lada, C. J. 1994, ApJ, 434, 614

Gregersen, E. M. & Evans, N. J., II 2000, ApJ, 538, 260

Habets, G. M. H. J., & Heintze, J. R. W. 1981, A&A, 46, 193

Hartmann, L., & Kenyon, S. J. 1985, ApJ, 299, 462

Harvey, P. M., Chapman, N., Lai, S.-P.. Evans, N. J., II, Allen, L. E., Jørgensen, J. K., Mundy, L. G., et al. 2006, ApJ, 644, 307

Harvey, P. M., Merin, B., Huard, T. L., Rebull, L. M., Chapman, N. Evans, N. J., II, & Myers, P. C. 2007a, ApJ, in press (preprint: arXiv:0704.0009 [astro-ph])

Harvey, P. M., Rebull, L. M., Brooke, T., Spiesman, W. J., Chapman, N., Huard, T. L., Evans, N. J., II, et al. 2007b, ApJ, in press (preprint: arXiv:0704.0253 [astro-ph])

Hatchell, J., Fuller, G. A., Richer, J. S., Harries, T. J., & Ladd, E. F. 2007, A&A, accepted (preprint:astro-ph/0612601)

Herbig, G. H. & Kameswara, R. N. 1972, ApJ, 174, 401

Jeans, J. H. 1928, *Astronomy and Cosmogony*, p. 340. Cambridge, U.K.: Cambridge University Press

Johnstone, D., Wilson, C. D., Moriarty-Schieven, G., Joncas, G., Smith, G., Gregersen, E., & Fich, M. 2000, ApJ, 545, 327

Jørgensen, J. K., Harvey, P. M., Evans, N. J., II, Huard, T. L., Allen, L. E., Porras, A., Blake, G. A., et al. 2006, ApJ, 645, 1246

Jørgensen, J. K., Johnstone, D., Kirk, H., & Myers, P. C. 2007, ApJ, 656, 293

Kenyon, S. J., & Hartmann, L. W. 1995, ApJS, 101, 117

Kenyon, S. J., Hartmann, L. W., Strom, K. M., & Strom, S. E. 1990, AJ, 99, 869

Kirk, H., Johnstone, D., & DiFrancesco, J. 2006, ApJ, 646, 1009

Kroupa, P. 2002, Science, 295, 82

Lada, C. J. 1987, in IAU Symp. 115, Star Forming Regions, editors M. Peimbert & J. Jugaku (Dordrecht: Reidel), p. 1

Lada, C. J., & Lada, E. A. 2003, ARA&A, 41, 57

Looney, L. W., Mundy, L. G., & Welch, W. J. 2000, ApJ, 529, 477

Luhman, K. L., Stauffer, J. R., Muench, A. A., Reike, G. H., Lada, E. A., Bouvier, J., & Lada, C. J. 2003, ApJ, 593, 1115

McCaughrean, M. J., Rayner, J. T., & Zinnecker, H. 1994, ApJ, 436, L189

McKee, C. F. 1989, ApJ, 345, 782

McKee, C. F., & Zweibel, E. G. 1992, ApJ, 399, 551

Motte, F., André, P., & Neri, R. 1998, A&A, 336, 150

Muench, A. A., Lada, E. A., Lada, C. J., & Alves, J. 2002, ApJ, 573, 366

Myers, P. C., Adams, F. C., Chen, H., Schaff, E. 1998, ApJ, 492, 703

Myers, P. C., & Ladd, E. F. 1993, ApJ, 413, 47

Natta, A., Testi, L., Calvet, N., Henning, Th., Waters, R., & Wilner, D. 2007, in Protostars and Planets V, editors B. Reipurth, D. Jewitt, and K. Keil, p. 767

Onishi, T., Kawamura, A., Tachihara, K., & Fukui, Y. 2002, ApJ, 575, 950

Ossenkopf, V., & Henning, Th. 1994, A&A, 291, 943

Pringle, J. E. 1989, MNRAS, 239, 361

Rebull, L. M., et al. 2007, ApJS, in press (preprint: astro-ph/0701711)

Reid, I. N., Gizis, J. E., & Hawley, S. L. 2002, AJ, 124, 2721

Reipurth, B., & Bally, J. 2001, ARA&A, 39, 403

Salpeter, E. E. 1955, ApJ, 121, 161

Scalo, J. M. 1986, Fundam. Cosmic Phys., 11, 1

Scalo, J. M. 2005, in The Stellar Initial Mass Function Fifty Years Later, Kluwer Academic Publishers, editors E. Corbelli, F. Palla, and H. Zinnecker, p. 23

Schröder, K.-P.,& Pagel, B. E. J. 2003, MNRAS, 343, 1231

Shirley, Y. L., Evans, N. J., II, & Rawlings, J. M. C. 2002, ApJ, 575, 337

Shirley, Y. L., Evans, N. J., II, Rawlings, J. M. C., & Gregersen, E. M. 2000, ApJS, 131, 249

Shu, F. H. 1977, ApJ, 214, 488

Shu, F. H., Adams, F. C., & Lizano, S. 1987, ARA&A, 25, 23

Spitzer, L. Jr. 1978, *Physical Processes in the Interstellar Medium*, New York: Wiley, p. 282

Tassis, K. & Mouschovias, T. Ch. 2004, ApJ, 616, 283

Testi, L., & Sargent, A. I. 1998, ApJ, 508, L91

Vieira, S. L. A., Corradi, W. J. B., Alencar, S. H. P., Mendes, L. T. S., Torres, C. A. O., Quast, G. R., Guimarães, M. M., & da Silva, L. 2003, AJ, 126, 2971

Visser, A. E., Richer, J. S., & Chandler, C. J. 2002, AJ, 124, 2756

Ward-Thompson, D., Scott, P. F., Hills, R. E., & Andre, P. 1994, MNRAS, 268, 276

Whitney, B. A., Wood, K., Bjorkman, J. E., & Cohen, M. 2003, ApJ, 598, 1079

Young, C. H. & Evans, N. J., II 2005

Young, C. H., Shirley, Y. L., Evans, N. J., II, & Rawlings, J. M. C. 2003, ApJS, 145, 111

Young, K. E., Enoch, M. L., Evans, N. J., II, Glenn, J., Sargent, A., Huard, T. L., Aguirre, J., et al. 2006, ApJ, 644, 326